Controlling superconductivity using tailored THz pulses

Dissertation

zur Erlangung des Doktorgrades an der Fakultät für Mathematik, Informatik und Naturwissenschaften

Fachbereich Physik

der Universität Hamburg

Vorgelegt vor

Biaolong Liu

aus Hebei, China

Hamburg

2019

Gutachter der Dissertation:	Prof. Dr. Andrea Cavalleri
	Prof. Dr. Franz X Kärtner
Zusammensetzung der Prüfungskommission:	
	Prof. Dr. Andrea Cavalleri
	Prof. Dr. Franz X Kärtner
	Prof. Dr. Markus Drescher
	Prof. Dr. Alexander Lichtenstein
	Prof. Dr. Michael A. Rübhausen
Vorsitzender des Prüfungskommission:	Prof. Dr. Michael A. Rübhausen
Datum der Disputation:	27.04.2020
Vorsitzender des Promotionsausschusses:	Prof. Dr. Wolfgang Hansen
Leiter des Fachbereich Physik:	Prof. Dr. Michael Pottho
Dekan der Fakultät MIN:	Prof. Dr. Heinrich Graener

Hiermit erkläre ich an Eides statt, dass ich die vorliegende Dissertationss- chrift selbst verfasst und keine anderen als die angegebenen Quellen und Hilfsmittel benutzt habe. Diese Arbeit lag noch keiner anderen Person oder Prüfungsbehörde im Rahmen einer Prüfung vor.

I hereby declare, on oath, that I have written the present dissertation on my own and have not used other than the mentioned resources and aids. This work has never been presented to other persons or evaluation panels in the context of an examination.

Hamburg, den Biaolong Liu

Abstract

Many transition metal oxides show strong electronic correlations that produce functionally relevant properties like metal-insulator transitions, colossal-magnetoresistance, ferroelectricity, and unconventional superconductivity. The development of intense femtosecond laser sources has made possible to control these functionalities and explore unknown out-of-equilibrium phase states of such complex materials by light.

In particular, selective excitation of infrared-active phonon modes by intense THz pulses has been demonstrated as a powerful tool to manipulate electronic and magnetic phases. So far, this approach has been restricted to the excitation of phonons with frequencies above 15 THz, limited by the lack of intense sources at lower frequencies. Notably, these distorted perovskite compounds exhibit further lower energy vibrational modes, which fall into the so-called "Terahertz gap" frequency regime. These low energy excitations also hold promise to manipulate novel phases and physical processes, maybe with even better efficiency.

Within this thesis, I developed a novel table-top source of narrowband intense THz pulses tunable across the frequency gap. Chirped-pulse difference frequency generation in nonlinear organic crystals was employed to overcome the limitations of earlier approaches.

This source was then applied to investigate light-induced superconductivity in high-temperature cuprates, that is the existence of an optically excited short-lived superconducting-like state far above the thermodynamic transition temperature. In $YBa_2Cu_3O_{6+x}$, this phenomenon has so far been associated with the nonlinear excitation of certain lattice modes and the creation of new crystal structures. I measured the photo-susceptibility of the light-induced state in $YBa_2Cu_3O_{6.5}$ throughout the far-, near-, and mid-infrared optical spectrum and found signatures of nonequilibrium superconductivity only for far-infrared excitations that are resonant with vibrational modes that drive *c*-axis apical oxygen atomic positions. In addition, a second resonance is observed at the charge transfer band edge at near-infrared frequencies.

These observations highlight the importance of light coupling to the electronic structure of the cuprates, either mediated by a phonon or by charge transfer. Beyond, these experiments demonstrate the capability of the newly developed source in nonlinear optical spectroscopy, hence open up new possibilities for the vibrational control of condensed matter.

Zusammenfassung

Viele Oxide der Übergangsmetalle zeigen starke Elektronenkorrelationen, die sich in funktionell relevanten Eigenschaften wie einem Metall-Isolator Übergang, dem kolossalen magnetoresistiven Effekt, der Ferroelektrizität oder der unkonventionellen Supraleitung zeigen. Die Entwicklung von Quellen intensiver ultrakurzer Laserpulse ermöglichte jüngst die Kontrolle dieser Funktionalitäten sowie die Erforschung bisher unbekannter Phasenzustände dieser komplexen Materialien außerhalb des Gleichgewichts durch Anregung mit Licht.

Speziell die selektive Anregung infrarot-aktiver Phononen mit intensiven THz-Pulsen wurde als mächtiges Werkzeug zur Manipulation elektronischer und magnetischer Phasen benutzt. Bisher war dieser Ansatz aber auf die Anregung von Phononen mit Frequenzen oberhalb von 15 THz beschränkt, limitiert durch den Mangel an intensiven Lichtquellen bei niedrigeren Frequenzen. Insbesondere die so verzerrten Perowskit-Verbindungen erhalten weitere niederenergetische Vibrationsmoden in der sogenannten „Terahertz-Lücke“, die vermutlich ebenso die Manipulation neuartiger Phasenzustände und physikalischer Prozesse ermöglichen, womöglich mit größerer Effizienz.

In dieser Arbeit habe ich eine neuartige kompakte Quelle schmalbandiger THz-Strahlung entwickelt die innerhalb der „Terahertz-Lücke“ frequenz-durchstimmbar ist. Um die Beschränkungen früherer Ansätze zu überwinden wurde die Differenzfrequenzmischung zeitlich gestreckter Pulse in nichtlinearen organischen Kristallen verwendet.

Diese Quelle wurde dann benutzt um die lichtinduzierte Supraleitung, d.h. die Existenz eines optisch angeregten kurzlebigen supraleitungsähnlichen Zustands, in Kupraten bei Temperaturen weit über der thermodynamischen Sprungtemperatur zu untersuchen. In $YBa_2Cu_3O_{6+x}$ wird dieses Phänomen bisher mit der nichtlinearen Anregung bestimmter Gitterschwingungen und der Erzeugung neuer Kristallstrukturen in Verbindung gebracht.

Ich habe die Photo-Suszeptibilität des lichtinduzierten Zustands in $YBa_2Cu_3O_{6+x}$ über das gesamte fern, mittel- und nah-infrarote optische Spektrum gemessen. Hinweise auf die Nichtgleichgewichtssupraleitung fand ich nur bei resonanter Anregungen von Vibrationsmoden im Fernen Infrarot, welche die apikalen Sauerstoff-Atome entlang der c-Achse bewegen. Eine zweite Resonanz am Rand des Ladungstransfer-Bandes bei nahinfraroten Frequenzen wurde gefunden.

Diese Beobachtungen unterstreichen die Wichtigkeit der Lichtwechselwirkung mit der elektronischen Struktur der Kuprate, die entweder durch ein Phonon vermittelt oder durch einen Ladungstransfer hervorgerufen wird. Zusätzlich zeigen diese Experimente die

Leistungsfähigkeit der neu entwickelten Quelle in der nichtlinearen Spektroskopie auf und eröffnen neue Möglichkeiten der Kontrolle von Festkörpern durch die Anregung von Gitterschwingungen.

Contents

List of Publications

The present thesis is based on my work as a doctoral student at the Max Planck Institute for the Structure and Dynamics of Matter, Hamburg, within the Quantum Condensed Matter Division and at the University of Hamburg.

The results presented in this manuscript are based on the following papers:

1. **B. Liu**, M. Först, M. Fechner, D. Nicoletti, J. Porras, B. Keimer, A. Cavalleri, Pump frequency resonances for light-induced incipient superconductivity in $YBa_2Cu_3O_{6.5}$. *Phys. Rev. X,* **10**, 011053 (2020)

2. **B. Liu**, H. Bromberger, A. Cartella, T. Gebert, M. Först, A. Cavalleri, Generation of narrowband, high-intensity, carrier-envelop phase stable pulses tunable between 4 and 18 THz. *Opt. Lett.,* **42**, 1, 129 (2017).

Other publications beyond the ones related to the results discussed in the thesis:

3. R. Mankowsky, **B. Liu**, S. Rajasekaran, H. Liu, D. Mou, X. J. Zhou, R. Merlin, M. Först and A. Cavalleri, Dynamical stability limit for charge density wave in $K_{0.3}MoO_3$. *Phys. Rev. Lett.,* **118**, 116402 (2017).

4. A.S. Disa, M. Fechner, T.F. Nova, **B. Liu**, M. Först, D. Prabhakaran, P.G. Radaelli and A. Cavalleri, Polarizing an antiferromagnet by optical engineering of the crystal field. *arXiv:2001.00540 accepted at Nature Physics.*

Introduction

The ability to control electronic and magnetic phases of strongly correlated materials has been drawing enormous interest in condensed matter physics. One class of such correlated systems are transition metal oxides, for example, manganites, nickelates or cuprates, which exhibit many technologically interesting properties like metal-insulator transitions, colossal magnetoresistance, ferroelectricity, and superconductivity. Temperature and doping concentration are routinely tuned to control these properties and result in complex phase diagrams. Beyond, external magnetic fields and pressure have been shown to manipulate the electronic and magnetic phases statically. For example, the critical temperature of high-T_C cuprate superconductors can be increased by the application of pressure.

Over recent decades, control of the macroscopic phases by short light pulses has become one of the grand goals in ultrafast condensed matter physics. Figure 0.1 depicts the schematic drawing of the electromagnetic spectrum of light in a wide frequency range, together with fundamental excitations in complex solids that can be driven in the different spectral regions. Electronic excitations dominate the near-infrared (NIR) and visible frequency range, while the excitation of the lattice vibrational modes, i.e. phonons, and the collective modes of broken symmetry states take place at mid-infrared (MIR) and terahertz (THz) frequencies.

Ultrafast pulses in the visible/NIR have been widely used to steer the phases in strongly correlated materials on the sub-picosecond time scale [1]. However, incoherent dynamics takes place via heat dissipation immediately afterward, due to the significant amount of entropy introduced in the system.

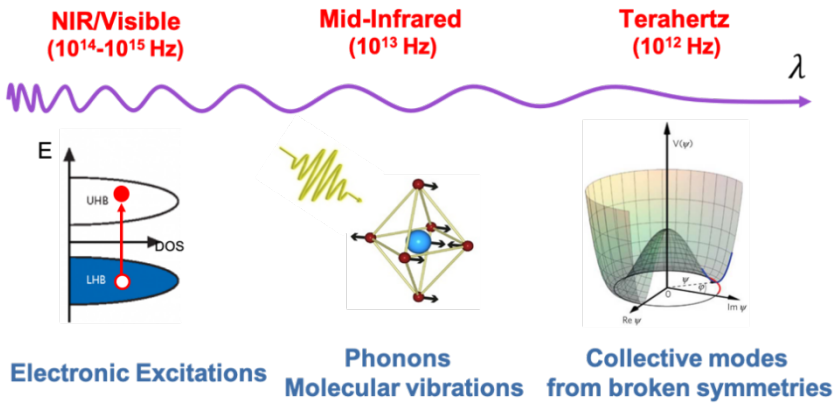

Figure 0.1. The electromagnetic spectrum of the light wave and the corresponding fundamental excitation in solids in different energy scales.

The resonant excitation of the vibrational modes using intense pulses in the MIR (5-20 μm, 15-50 THz) regime has recently been witnessed as the milestone of ultrafast phase control in quantum materials [1]-[7]. Selective optical excitation of phonons is particularly interesting in systems, in which the electronic and magnetic properties are known to depend critically on the crystallographic structure. The insulator-metal transition in antiferromagnetic insulating manganites [1], the cross-interface control of charge and magnetic order in nickelate hetero-structures [2][8], the polarization reversal in ferroelectrics [9] and the control of the superconducting properties in high-T_c cuprates [6][10][11] highlight the success of this novel approach.

Resonant phonon excitation has also been exploited to manipulate the superconducting order parameter in high-T_C cuprate superconductors. Optical fingerprints of the transient light-induced superconducting-like state have been evidenced using time-resolved THz spectroscopy combined with resonant driving of the apical-oxygen phonons in the pseudogap phase. Strikingly, a few picoseconds long-lived superconducting state was induced in underdoped bilayer $YBCO_{6+x}$ compounds far above the thermal transition temperature and even above room temperature. The light-induced coherent phase superimposed on the equilibrium phase diagram is reported in Figure 0.2(a).

One mechanism proposed for light-induced superconductivity goes back to anharmonicities of the crystal lattice, cast in the term ‘nonlinear phononics’. That is, the infrared-active apical oxygen phonon mode of B_{1u} symmetry, resonantly excited to large-amplitude, couples nonlinearly to other lattice vibrations, in this case an A_g symmetry Raman-active mode, to transiently distort the crystal structure. The atomic displacements along the Raman mode coordinates, which were identified in a time-resolved x-ray diffraction experiment and then proposed to play an important role in the formation of the light-induced

superconducting state, are sketched in Figure 0.2(b). The change of distances of CuO_2 layers along the crystallographic *c*-direction presumably modifies the spatial overlap of certain copper d-orbitals to favor the superconducting-like state.

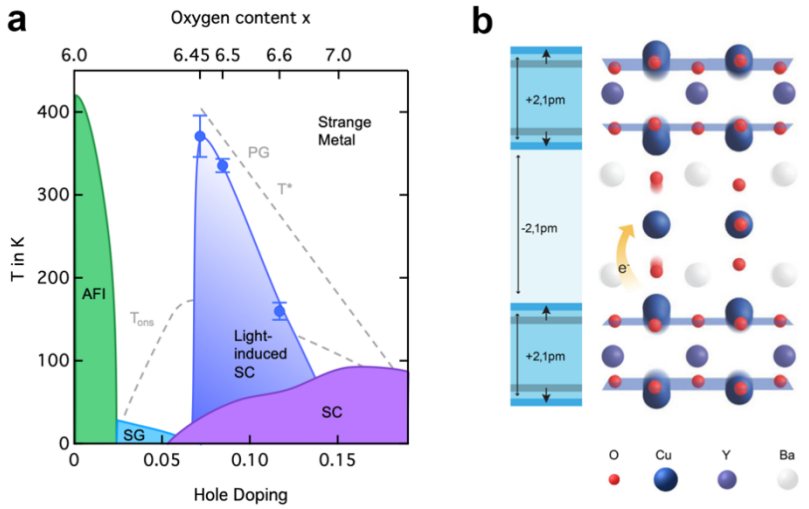

Figure 0.2. (a) Schematic phase diagram of $YBa_2Cu_3O_{6+x}$ as a function of temperature and hole concentration. On top of the generic equilibrium phases, a light-induced superconducting phase within the pseudogap phase emerges after the resonant excitation of IR-active phonons along the crystal c-axis. **(b)** Sketch of transient structure change and enhancement of Josephson tunneling. Adapted from [12][13].

This mechanism could be critically assessed if one was able to selectively drive different vibrational modes and inspect the transient changes in the electronic properties. The goal of the present thesis is to gain new insight into the phenomena of light-induced superconductivity in the bilayers cuprates $YBCO_{6+x}$ by tackling this open question.

So far, however, the spectral range at which these phonons were resonantly driven was restricted to frequencies above ~15 THz, even though the cuprates and other transition metal oxides exhibit further vibrational modes at lower frequencies. For instance, as sketched in Figure 0.3, several vibrational modes can be identified in the optical conductivity (red) of $YBCO_{6+x}$, which are associated with different collective atomic motions (insets). The reason for this shortcoming lies in the lack of powerful table-top light sources in the *terahertz gap* between 3 and 15 THz. It is the absorption and dispersion of THz radiation in the *Reststrahlen* band of the nonlinear optical crystals, like GaSe, which have typically been used to generate intense ~100 MV/cm peak electric field pulses via difference-frequency generation, which restricts the accessible frequency range.

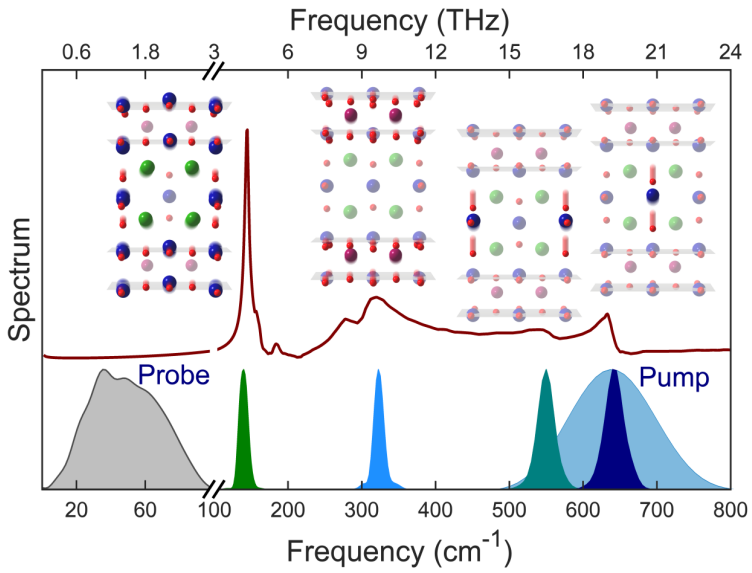

Figure 0.3. Top: Various optical vibration modes along the *c*-axis of $YBa_2Cu_3O_{6.5}$. Middle: optical conductivity in the same direction. Bottom: Fourier spectrum of different generated THz pulses together with the broadband THz probe.

The availability of high-quality organic crystals with significant nonlinear susceptibility and low absorption in the THz range has opened up new possibilities in the vibrational phase control.

In this thesis, frequency-mixing in large aperture organic crystal DSTMS has been demonstrated as a novel approach for the generation of frequency-tunable, narrowband pulses across the THz-gap, which could then be applied to selectively excite different vibration modes in complex solids.

With the aid of this home-built optical device, a first phonon mode-selective investigation of the light-induced superconductivity was performed in $YBCO_{6+x}$ (see Figure 0.3). By systematically tuning the pump frequency throughout the entire optical spectrum, the frequency-dependent photo-susceptibility for this light-induced coherent state was measured. The ultrafast responses of the light-induced state following the resonant excitation of various infrared-active modes will be interpreted together with the corresponding transient atomic displacements determined by *ab-initio* calculations based on nonlinear phononics theory. The deviation from the theoretical prediction and the observation of a second resonance peak in the photo-susceptibility in the near-IR frequency range suggests that the anharmonic phonon coupling is not the only possible mechanism underlying optically-driven superconductivity in cuprate superconductors.

Thesis structure

This thesis is structured as follows:

Chapter 1 summarizes the recent achievements of vibrational phase control in strongly correlated electron materials with intense THz pulses. The basic concept of nonlinear phononics, which can explain many of the experimental observations, will be introduced.

With the goal of accessing low energy vibrational modes, a novel optical parametric device, filling the vacancy of the "THz-gap", was developed. The principles and experimental techniques of narrowband THz pulse generation will be discussed in Chapter 2.

Chapter 3 then introduces the physics of unconventional high-T_c superconductors, with a focus on the equilibrium crystal structures and superconducting properties.

Experiments on the vibrational control of superconductivity in the high-T_c cuprate superconductor $YBa_2Cu_3O_{6+x}$ via mode-selective excitation using narrowband THz pulses will be presented in Chapter 4.

Finally, the conclusion and possible future investigation will be summarized at the end of this thesis.

Chapter 1

1. Vibrational phase control of strongly correlated electron materials

A characteristic of correlated materials is the strong interplay between charges, orbitals, spins, and crystal lattice. Small perturbations of this interaction hence produce enormous susceptibilities. Traditionally, such responses have been studied utilizing static control knobs such as temperature, pressure, and carrier doping. In recent years, also the dynamical perturbations, in combination with pump-probe experiments, became a useful and insightful tool to study these materials.

A unique approach in this respect is phononics, the selective excitation of infrared active phonon modes in materials. Many electronic and magnetic properties depend or become determined by the arrangement of the atoms in the crystal lattice. The displacement of the fundamental lattice modes, phonons, hence allows to switch or create entirely new electronic phases.

Intense terahertz pulses are powerful tools in controlling the functionalities in complex solids and molecular systems. Due to the low photon energy, strong-field THz pulses (below 3 THz) have been exploited to induce the energy transfer of the optical phonons [14], parametric amplify the Josephson plasma wave [15], and unfold the hidden ferroelectric phase [3]. On the other hand, by driving lattice vibration modes to large-amplitude with intense pulses above 15 THz, ultrafast control of insulator-metal transition [1][5], ferroelectric

switching [9], high harmonic generation of optical phonons [16] and light control of superconductivity [6][10][11] have been witnessed over the past decade.

Nonlinear phononics theory has been proven to be an elegant tool in understanding the phase changes through anharmonic coupling induced by large-amplitude displacement of the driven infrared-active phonons. Various coupling mechanisms have been investigated to theoretically predict the vibrational phase control in transition metal oxides, such as light-induced metallicity, ferroelectricity and superconductivity.

In this chapter, recent experiments of such a vibrational phase control in strongly correlated materials using intense THz pulses are summarized. The underlying theoretical models are introduced, which are based on the anharmonic coupling between phonon modes and other degrees of freedom. Finally, exemplary time-resolved x-ray diffraction measurements are discussed, which implement the theoretical models and provide information for the connection between the phase transition and the structural deformation in the nonequilibrium state.

1.1 Controlling the crystal lattice with THz pulses

In this section, I will introduce the concept of nonlinear phononics. In the following, the first experimental demonstration and recent progress on nonlinear phononic coupling will also be discussed. The theory on nonlinear phononics has been systematically discussed in Ref. [17], which acts as the theoretical basis of this section.

The behavior of the vibrational modes of the crystal lattice can be described by the simple Lorentzian model, which regards the dynamics of the phonon modes as harmonic oscillators [18].

However, when the harmonic oscillator is driven to large-amplitude, higher order terms come into play for large-amplitudes as the crystal lattice is anharmonic. Considering the resonant excitation of an optical phonon, the crystal Hamiltonian can be described as following

$$H = H_L + H_{NL} \tag{1.1}$$

where H_L and H_{NL} denote the linear and nonlinear response of the total Hamiltonian [17]. Since the wavelength of the driving IR phonon mode is much longer than the lattice constant,

the wavevector of the phonon mode $\boldsymbol{k}$ in the momentum space is approximately zero. The Hamiltonian of the linear response at $\boldsymbol{k} = \mathbf{0}$ is then given by

$$H_L = \frac{1}{2}(P_{IR}^2 + \omega_{IR}^2 Q_{IR}^2) + \sum_{\boldsymbol{j}} \frac{1}{2}(P_j^2 + \omega_j^2 Q_j^2) \tag{1.2}$$

where P_{IR}, ω_{IR}, Q_{IR}, P_{IR}, ω_j, Q_j, P_{IR} denote the momentum, eigenfrequency and normal coordinate of the driven IR-active mode and the coupled mode. For the driven vibrational mode, the applied THz light field resonating with the oscillator acts as a driving force $f(t) = e^{-\frac{t^2}{2\sigma^2}} sin(\omega_{IR} t)$. The dynamics can be described by the equation of motion of a harmonic oscillator derived from the Lagrange equation as

$$\ddot{Q}_{IR} + 2\gamma_{IR}\dot{Q}_{IR} + \omega_{IR}^2 Q_{IR} = Z^* f(t) \tag{1.3}$$

where ω_{IR}, γ_{IR} and Z^* denote the frequency, damping factor and Born effective charge of the oscillator, respectively. The decay time of the oscillation is set by the damping factor as $1/\gamma_{IR}$, and in most of the cases the phonon modes are under-damped.

When the IR-active mode is driven to large amplitude, the higher-order anharmonic terms of the driven phonon should be taken into consideration. In the meantime, the driven IR-active mode will also couple to other lattice vibrations, which shift the energy potential of the system. The nonlinear response contains the high-harmonic terms of the driven IR-active mode and the nonlinear coupling terms to other modes. The nonlinear Hamiltonian can be expressed as

$$H_{NL} = \sum_{m>2} a_m Q_{IR}^m + \sum_j (a_{12} Q_{IR} Q_j^2 + a_{21} Q_{IR}^2 Q_j + a_{22} Q_{IR}^2 Q_j^2 + a_{13} Q_{IR} Q_j^3 + a_{31} Q_{IR}^3 Q_j \ldots) \tag{1.4}$$

The first summation describes the high-harmonic terms of the driven phonon, while the second summation gives the nonlinear coupling terms of the cubic and quartic couplings. The model considering the higher-order anharmonicity of the driven IR-active mode has successfully explained the experimental observations of the high-harmonic signals in vibrationally excited $LiNbO_3$ [16]. Further, the anharmonic coupling between the IR-active mode to an A_g Raman mode which inducing a transient structural deformation has proven to be the microscopic mechanism in various of nonequilibrium measurements of strongly correlated materials using THz fields [1]-[6].

1.1.1 Cubic coupling

To begin with, we restrict the situation to centrosymmetric crystals, for instance, manganites $La_{1-x}Sr_xMnO_3$, $Pr_xCa_{1-x}MnO_3$, and cuprates $YBCO_{6+x}$, in which the IR-active modes are of odd paring symmetry. In these compounds, the first cubic coupling term $a_{12}Q_{IR}Q_j^2$ is always zero, while the second term will take nonzero value only if Q_j has a A_{1g} symmetry, which represents the full symmetry [20]. In this case, the coupling mode must be a Raman-active mode. The cubic coupling term in the Hamiltonian results in a shifted energy potential of the system shown in Figure 1.1(a). The dynamics of both the driven IR-active mode and the anharmonically coupled Raman mode is given by the coupled equations:

$$\ddot{Q}_{IR} + 2\gamma_{IR}\dot{Q}_{IR} + \omega_{IR}^2 Q_{IR} = Z^* f(t) + 2a_{21}Q_{IR}Q_R \tag{1.5}$$

$$\ddot{Q}_R + 2\gamma_R\dot{Q}_R + \omega_R^2 Q_R = 2a_{21}Q_{IR}^2 \tag{1.6}$$

here Q_R, γ_R, ω_R denote the normal coordinate, damping factor and eigenfrequency of the Raman mode, respectively. According to (1.6), the driving force for the Raman mode is proportional to Q_{IR}^2, oscillating at two times of ω_{IR}. This term leads to a shift of the energy potential of the Raman mode (see Figure 1.1(a)). Figure 1.1(b) simulates the driving force and the normal coordinate of the driven Raman-active mode.

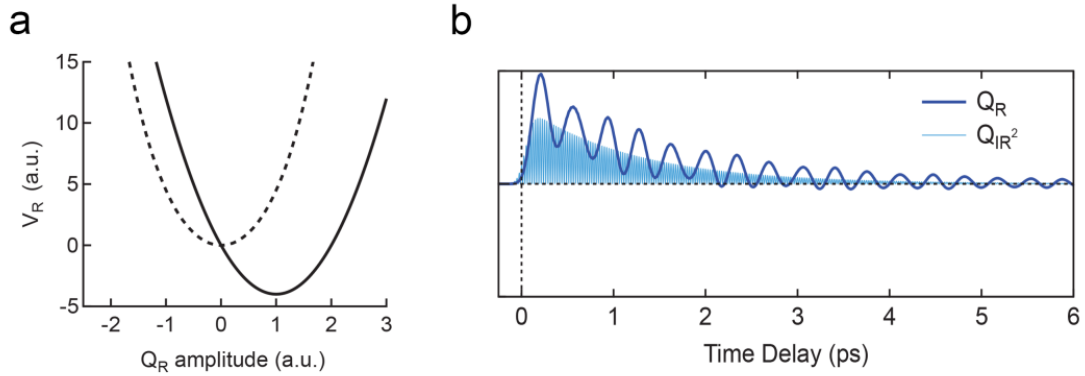

Figure 1.1. (a) Equilibrium energy potential (dashed curve) and the shifted potential through the cubic nonlinear coupling (solid curve) for the Raman mode. **(b)** Dynamics of the driving force (light blue) and the normal coordinate (dark blue) for the anharmonically coupled Raman mode [17].

1.1.2 Quartic coupling

Most of the nonlinear processes, which have been discovered over the past decade, are dominated by the cubic coupling to certain Raman-active modes. However, when the lattice vibration is excited by an even higher electric field, the higher-order nonlinear coupling

becomes prominent. The nonlinear Hamiltonian through quartic coupling to a Raman-active mode can be described as

$$H_{NL} = a_{22} Q_{IR}^2 Q_j^2 \tag{1.7}$$

Notably, the coupled mode Q_j is not constrained to optical modes, which means any generation of mode pairs with opposite wavevectors can participate [17].

The energy potential of the coupled mode is captured as Figure 1.2(a). Compared with the cubic coupling, the potential is not shifted but softened (or stiffened). For the case of softening, beyond a certain threshold, the potential becomes unstable and can lead to a symmetry-breaking transition [20].

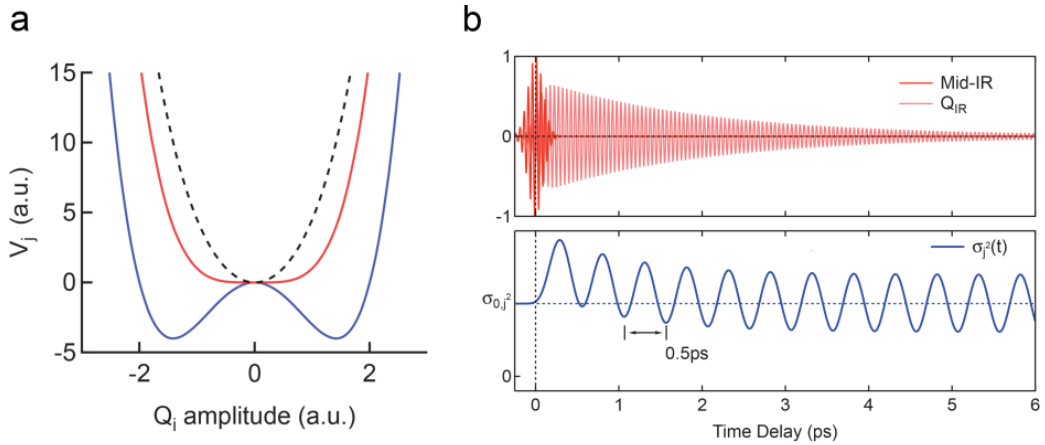

Figure 1.2. (a) The energy potential of the coupled mode through quartic coupling. It is deformed to be softened (red) or stiffened into an unstable double well potential. **(b)** Instead of displacing the crystal lattice, the variance of the coupled mode $\sigma_j^2 =< Q_j^2 >$ is oscillating at twice the frequency of the coupled mode [17].

The equation of motion describing the dynamics of the coupled mode is rewritten as [17]:

$$\ddot{Q}_j + 2\gamma_j \dot{Q}_j + \omega_j^2 Q_j = 2a_{22} Q_{IR}^2 Q_j \tag{1.8}$$

Normalization in the frequency of the coupled mode $\omega_j^* = \sqrt{\omega_j^2 - 2a_{22}Q_{IR}^2}$ takes place through such coupling. If the amplitude of the IR mode is above the threshold, the frequency of mode Q_j becomes imaginary, which destabilizes the system.

The quartic coupling has been applied to simulate the dynamics of cuprate superconductors La_2CuO_4, in which a cubic coupling is forbidden. Instability can be induced beyond the threshold, resulting in a distortion intro a crystal structure of lower symmetry [21].

1.1.3 First experimental demonstration

Nonlinear phononics was first experimentally demonstrated by M. Först et. al. in an optical measurement on ferromagnetic insulating manganite $La_{0.7}Sr_{0.3}MnO_3$ [18]. In this experiment, large-amplitude resonant excitation of an E_u Mn-O stretching mode was triggered by sub-ps THz pulses at 20 THz (~ 605 cm^{-1}). The time-dependent optical reflectivity measurement following the excitation is depicted in Figure 1.3(a). By subtracting the differential signal between the orthogonal polarization in the probe beam, a clear oscillation at 1.2 THz was observed (left inset), which can be associated with an E_g Raman mode involving the rotation of oxygen octahedron around the Mn cations [18] (right inset). In Figure 1.3(b), the amplitude of the oscillation is plotted as a function of pump wavelength. The wavelength-dependent amplitude overlaps the linear absorption coefficient nicely, manifesting the light-induced effect to be a phonon-mediated process.

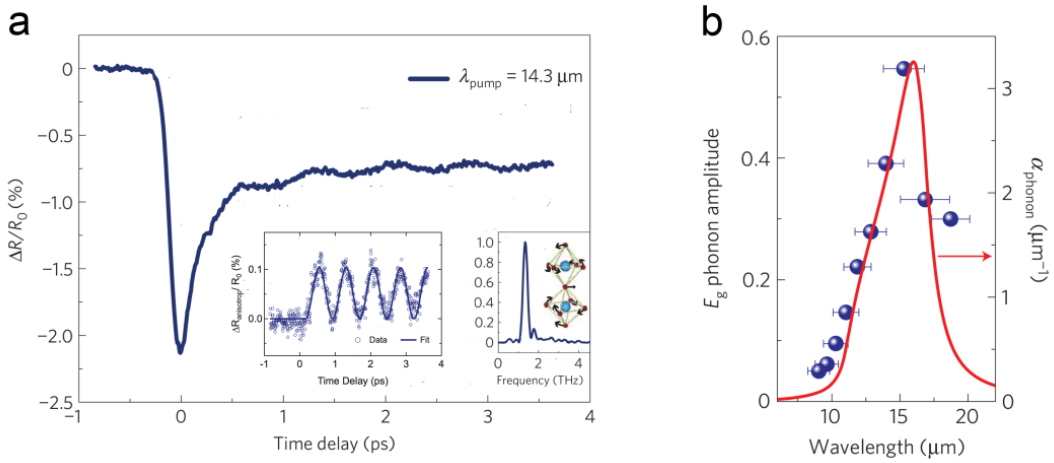

Figure 1.3. (a) Time-resolved reflectivity changes following resonant excitation of the E_u symmetry Mn-O stretching vibration at 14.3 µm in $La_{0.7}Sr_{0.3}MnO_3$. Insets: left is the Raman phonon-induced anisotropic contributions to the transient reflectivity; right is the corresponding Fourier spectrum and the atomic motion of the Raman mode. **(b)** Amplitude of the Raman oscillation (blue circles) and linear absorption coefficient (red line) of $La_{0.7}Sr_{0.3}MnO_3$ as a function of pump wavelength. Adapted from [18].

A complementary experiment was later performed with time-resolved x-ray probe to identify the structural change predicted by nonlinear phononics. The atomic motions of the driven IR phonon mode and the rotational E_g Raman mode are illustrated in Figure 1.4(a). Notably, anti-phase rotations of the two MnO_6 octahedra are theoretically predicted by nonlinear phononics theory to follow the THz excitation. The intensity modulation of the (201) and (012) lattice Bragg peaks was measured with high-brightness x-ray in LCLS. Opposite relative intensity changes of the two peaks are depicted in Figure 1.4(b), where the solid lines are the solution to the coupled equations of motion. The sign and ratio of the two structure

factor changes in the experiment could be nicely predicted by considering the cubic coupling term [25].

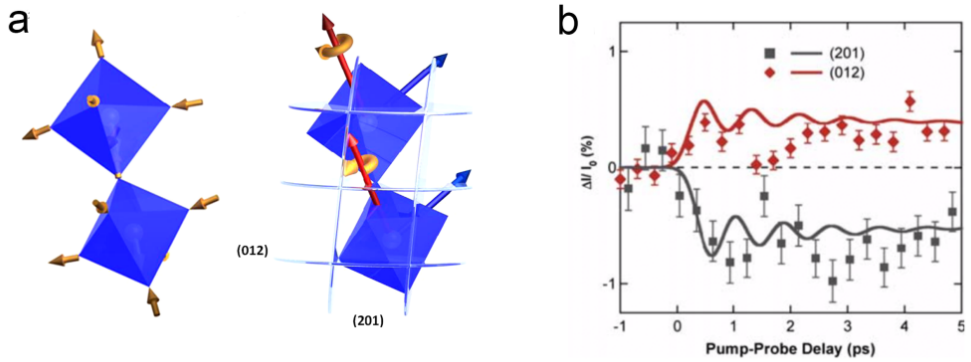

Figure 1.4. (a) Left: atomic motions of the E_u symmetry Mn-O stretching mode in $La_{0.7}Sr_{0.3}MnO_3$. Right: sketch of the nonlinearly driven Raman-active mode, the rotation of the O-octahedra is around an axis (red) perpendicular the [111] crystal axis. **(b)** Relative X-ray intensity changes of the (201) and (012) Bragg peaks induced by MIR excitation. Figures are taken from [25].

1.2 Controlling electronic properties in perovskites

The first experimental demonstration of the vibrational phase control using strong field THz pulses was realized in the insulator to metal transition in manganite $Pr_{0.3}Ca_{0.7}MnO_3$. It is an example of the ultrafast phase control in complex solids, which triggered follow-up research. A second example is the vibrational phase control in $NiNdO_3/LaAlO_3$ hetero-structure. Ultrafast THz spectroscopy was exploited along with NIR reflectivity measurements in the light-induced phase transition. Notably, the time-resolved x-ray diffraction measurements, which provides insight for the transient structure changes as well as the phase dynamics, manifests itself to be the indispensable experimental method in the nonequilibrium study of quantum materials.

1.2.1 Ultrafast insulator-metal transition in manganite

In doped manganites like $La_{0.7}Sr_{0.3}MnO_3$ or $Pr_{0.7}Ca_{0.3}MnO_3$, the materials behave as either ferromagnet or antiferromagnet. The electronic and magnetic properties strongly depend on the Mn-O-Mn bond angles in such materials. In $Pr_{0.7}Ca_{0.3}MnO_3$, covalent-bond is formed between a half-filled orbital (Mn^{3+}) and an empty orbital (Mn^{4+}). If the Mn^{3+}-O^{2-}-Mn^{4+} bond is 180 degrees, electron hopping is enhanced and the system behaves as a ferromagnet. However,

in a strongly distorted perovskites, an antiferromagnetic (AFM) insulating phase emerges due to the bond bending [20]. This subtle structure change can be induced either by applying external pressure or photo-doping the system. In the experiment performed by M. Rini et al., the Mn-O stretching mode at 17-μm was resonantly excited by THz pulses. Figure 1.5(a) depicts the frequency-dependent reflectivity change in the excited state, which follows the equilibrium low-temperature optical conductivity within the pump frequency range. Strikingly, Figure 1.5(b) reports an approximately five-order-of-magnitude increase of the electrical conductivity, evidenced by measuring the current transport with a fast oscilloscope [1].

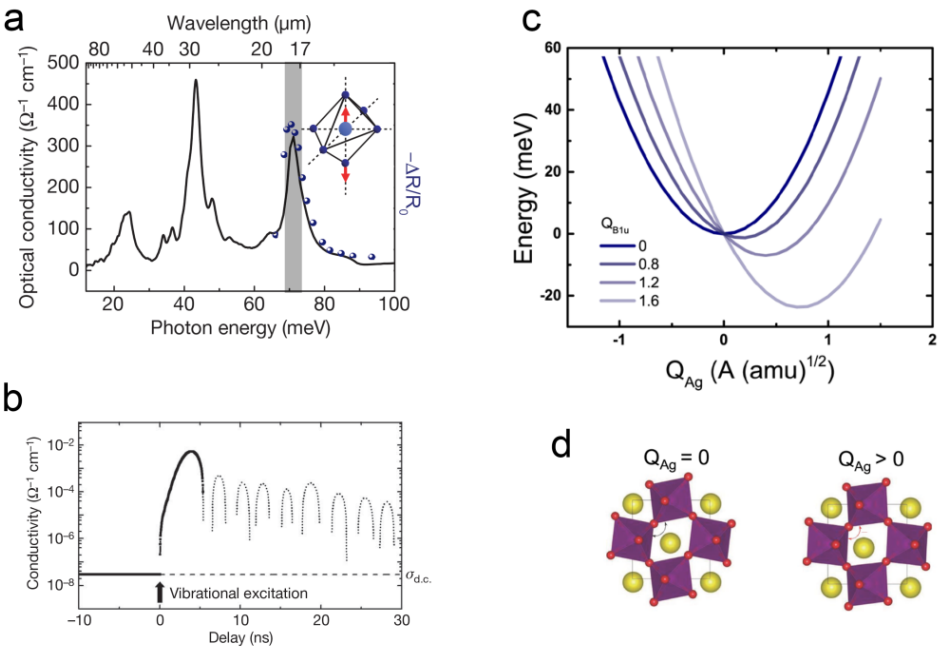

Figure 1.5. (a) Low-temperature optical conductivity spectrum of $Pr_{0.7}Ca_{0.3}MnO_3$. The inset shows the atomic displacements of the Mn-O stretching mode within the MnO_6 octahedra corresponds to the 71 meV (16.5 μm) peak in the conductivity spectrum. The blue dots are the relative change of the optical reflectivity measured after the vibrational excitation **(b)** Time-dependent conductivity after resonant excitation of the Mn-O stretching mode with 4-ns time resolution. **(c)** The Energy potential of the Raman mode for different static displacements of the IR mode. **(d)** Atomic position of the orthorhombically distorted perovskite at equilibrium (left) and with a positive amplitude of Raman mode. Adapted from [1][20].

The nonlinear phononics model was employed to exam the connection between the structure deformation and the emergence of the metallic phase. In Figure 1.5(c), the energy potential of a coupled A_g Raman mode is displayed for different static displacements of the IR mode in parent compound $PrMnO_3$, calculated by Subedi et al. based on density function theory [21]. Through cubic nonlinear coupling, the energy potential of the Raman mode shifts with a new minimum position. In Figure 1.5(d), the atomic motions associated with positive

amplitude results in lowering the symmetry and uncurling the Mn-O-Mn bonds. As aforementioned, such lattice distortion potentially suppresses the AFM orders. Further theoretical calculation of the electronic density of states is suggestive for the speculation of the light-induced metallicity. In the calculation. the gap at the Fermi energy for the equilibrium crystal structure is tended to close after the vibrational excitation of the B_{1u} mode [13].

To understand the microscopic process of the phase evolution, a time-resolved x-ray diffraction measurement on a qualitatively similar manganite $La_{0.5}Sr_{1.5}MnO_4$ was performed. Figure 1.6(a) reports the dynamics of melting the AFM and charge/orbital orders after the resonant excitation of the Mn-O stretching mode. The data was obtained by measuring the intensity changes associated with certain super-lattice reflections. Considering the nonlinear coupling, an A_g symmetry Jahn-Teller mode, which is distorted in the equilibrium state, relaxes due to the excitation of the B_{1u} mode. Consequently, the ordering of orbitals and spins is destabilized, which is evidenced by the diffraction measurement.

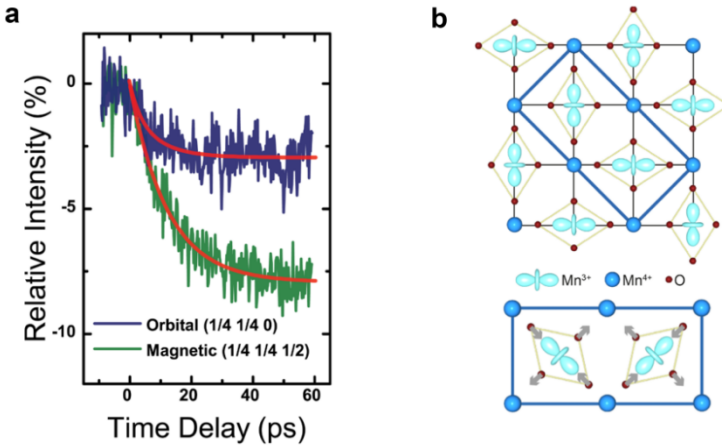

Figure 1.6. (a) Melting of antiferromagnetic and charge/orbital order in manganite $La_{0.5}Sr_{1.5}MnO_4$ after MIR excitation. **(b)** Top: in-plane charge/orbital order in the equilibrium state. Bottom: displacement of the oxygen atoms associated with the Jahn-Teller mode. Adapted from [20].

1.2.2 Vibrational control of ferroelectricity

It is evident that vibrational excitation of IR-active phonons can be exploited to induce metallicity in perovskites [1][2]. In this section, such phase control technique is extended to manipulate the ferroelectric properties in complex solids. As aforementioned, light-induced ferroic properties have been theoretically predicted by vibrational exciting the system. Via an

anharmonically coupled Raman-active mode, the tensors for ferroelectric polarization and magnetization could be directly coupled to, modifying the ferroic phases [22].

Previously, the vibrational excitation of high-frequency optical phonon was proven to unfold the hidden ferroelectric phase in paraelectric materials [3]. On the other hand, the ferroelectric polarization in the ferroelectrics, typically controlled with static or pulsed electric fields, could also be manipulated via vibrational excitation of high-frequency phonon in $LiNbO_3$, demonstrated by R. Mankovsky et al. [9].

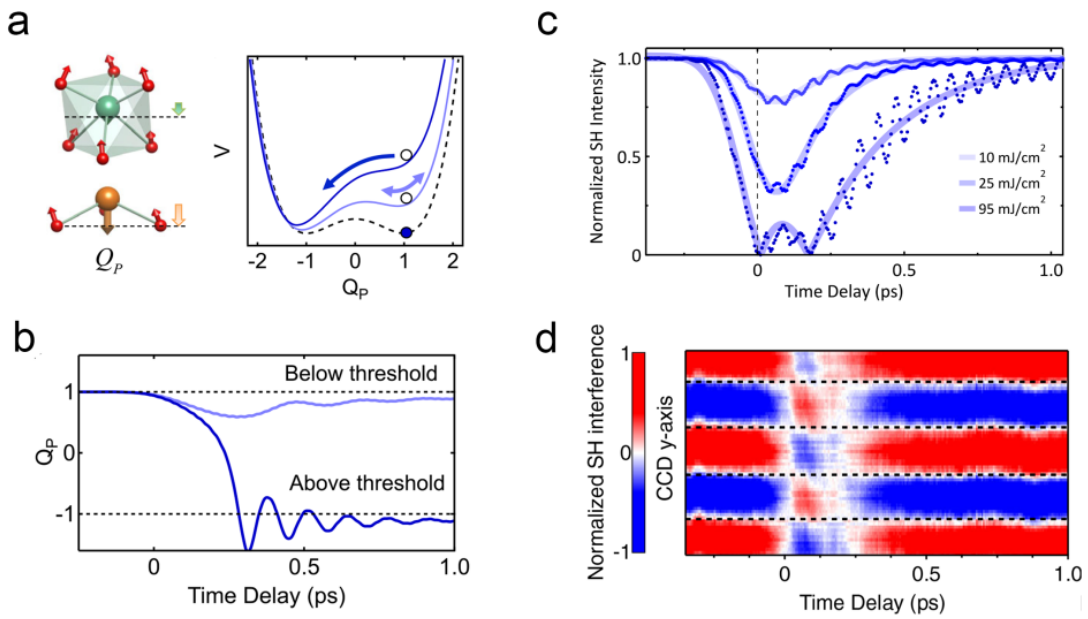

Figure 1.7. (a) Left: the atomic motion of the ferroelectric mode Q_P and double-well potential V(Q_P, Q_{IR}) along the mode direction. **(b)** The solution to the coupled equation of motion below and above a certain threshold. **(c)** Time-resolved second-harmonic intensity normalized to the value before excitation. (d) The time-resolved measurement of the interference fringes (integrated along x direction on CCD) shows a transient π phase shift after the THz excitation. Reproduced from [9].

The atomic motions of the ferroelectric mode in $LiNbO_3$ are sketched in Figure 1.7(a). The equilibrium energy potential of the ferroelectric mode has a double-well feature along the coordinate Q_P, and the value of Q_P will take one of the minima. Considering the cubic nonlinear coupling between the driven IR-active mode and the ferroelectric mode, the total lattice potential is given by

$$V(Q_P, Q_{IR}) = -\frac{1}{4}\omega_p^2 Q_p^2 + \frac{1}{4}c_P Q_p^4 + \frac{1}{2}\omega_{IR}^2 Q_{IR}^2 - aQ_{IR}^2 Q_P \tag{1.9}$$

For finite displacements Q_{IR}, this minimum is first displaced and then destabilized as Q_{IR} exceeds a threshold, as depicted in the right panel of Figure 1.7(a). Notably, even though the authors only take the Q_{IR}^2 term into account for the energy potential of the driven phonon

mode, the contributions from the higher-order terms (i.e. Q_{IR}^3) should however be considered as well when the coordinate of the IR phonon is driven to large-amplitude (see Ref. [16] by A.v. Hoegen et al. for more details).

The corresponding dynamics of the two modes will be governed by the rewritten equations of motion as

$$\ddot{Q}_{IR} + \gamma_{IR}\dot{Q}_{IR} + \omega_{IR}^2 Q_{IR} = 2aQ_P Q_{IR} + Z^* f(t), \tag{1.10}$$

$$\ddot{Q}_P + \gamma_P \dot{Q}_P - \tfrac{1}{2}\omega_p^2 Q_P + c_P Q_P^3 = aQ_{IR}^2. \tag{1.11}$$

Figure 1.7(b) reports the solution to the equations. The ferroelectric mode Q_P is driven to lower values and the polarization reverses permanently above a certain threshold.

Experimentally, time-resolved, phase-sensitive, second harmonic (SH) generation measurement following the 19-THz excitation was also performed. In Figure 1.7(c), the time-resolved SH intensity of the probe pulses at selected pump fluence F is reported. Further, when the pump fluence F < 50 mJ/cm^2, a reduction in SH intensity to a finite value within approximately 200 fs. In contrast, when pump with F ~ 95 mJ/cm^2, the SH intensity vanishes completely twice in the vicinity of an intermediate value before relaxing to the equilibrium.

In addition, the time-dependent interference of the SH field was measured by impinging the pump-induced SH pulse with a reference SH pulse generated in a non-excited crystal on a CCD camera. After excitation, the SH intensity first reduced with a constant phase. At zero-time delay, the phase of the second-harmonic field flipped by 180°, as revealed by a sudden sign change of the interference fringes. Within this time interval, the polarization was transiently reversed. The vibrational control of the polarization reversal on sub-picosecond timescale can be potentially used to manipulate the complex functionalities in materials. In another perspective, since the reversal of the ferroelectric polarization can be induced in both directions, it is promising to build nonvolatile ultrafast memory units [9].

1.2.3 Light-induced superconductivity in high-T_C cuprates

In this section, the vibrational phase control technique using intense THz pulses is exploited to promote the equilibrium superconducting phase and understand the interplay with competing orders. Time-resolved THz spectroscopy has been exploited to capture the phase information in ultrafast timescales. Besides, the dynamics of underlining stripe orders and

transient structure modulation were revealed by the time-resolved x-ray diffraction measurement.

Melting the competing order in the stripe phase of single-layer cuprates

Superconductivity was found in layered perovskite $La_{2-x}M_xCuO_4$, where M = Ba, Sr, Ca in 1986 [107]. Experimental results over the past decades show that in the CuO_2 planes there exists modulation of charge and spin density, which is often referred to as the stripe orders. The stripe orders not only compete with the static superconducting condensations, but also frustrate the interlayer coherent transport in a fashion of 90° rotation of the orientation between periodic stacking of CuO_2 layers (Figure 1.8(a)) [4][5]. For example, the schematic phase diagram and crystal structure (inset) of $La_{1.8-x}Eu_{0.2}Sr_xCuO_4$ are displayed in Figure 1.8(b). The stripe phase becomes static at a distinctive doping x=1/8 and completely quenches the superconducting state. So far, the coexistence and competition between superconductivity, stripe order and structural distortion are still puzzling in high-T_c cuprates [12].

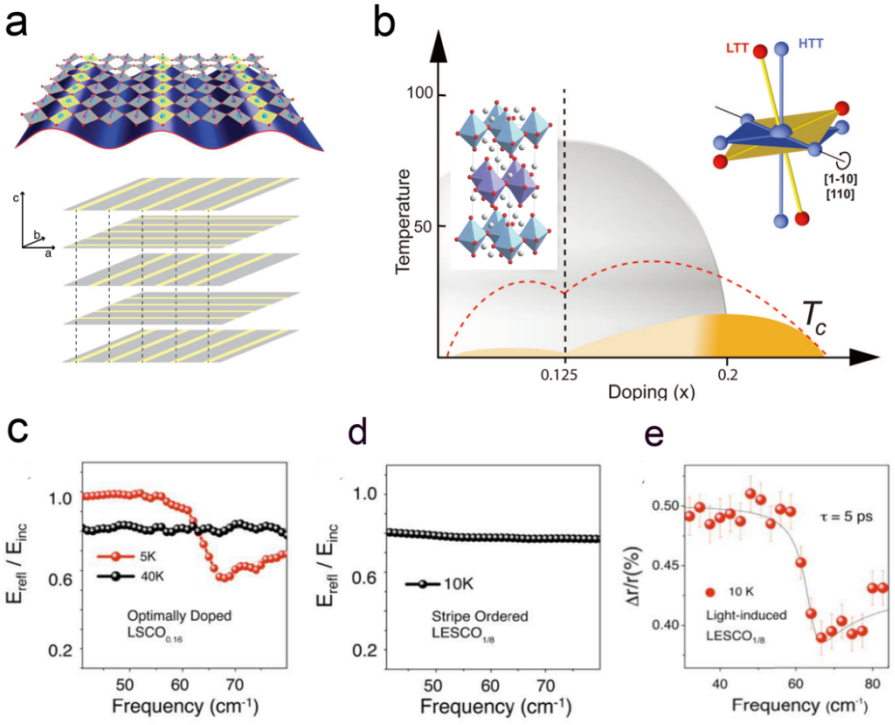

Figure 1.8. (a) Schematic drawing of the charge, spin, lattice arrangement within a CuO_2 plane. The periodic stacking of such CuO_2 planes is illustrated in the lower panel with a 90° rotation between adjacent layers. From Ref. [5]. **(b)** Schematic phase diagram and crystal structure (inset) for $La_{1.8-x}Eu_{0.2}Sr_xCuO_4$. **(c)** Equilibrium c-axis reflectivity of $La_{1.84}Sr_{0.16}CuO_4$ below and above T_c (T_c ~35 K). Josephson plasma resonance (red) appears in the superconducting phase. **(d)** Reflectivity of non-superconducting $La_{1.675}Eu_{0.2}Sr_{0.125}CuO_4$ at 10 K. **(e)** Light-induced in reflectivity edge in $La_{1.675}Eu_{0.2}Sr_{0.125}CuO_4$ by THz excitation at 10 K. Reproduced from [4].

In the experiment performed by D. Fausti *et al.* the vibrational excitation of optical phonons was first applied to induce a superconducting-like state in a non-superconducting compound $La_{1.675}Eu_{0.2}Sr_{0.125}CuO_4$. In high-$T_c$ superconducting cuprates, a prominent feature of the superconducting state is the Josephson plasma resonance showing in the THz frequency reflectivity perpendicular to the CuO_2 planes. As a related example, Figure 1.8(a) depicts the reflectivity of $La_{1.84}Sr_{0.16}CuO_4$ in the THz frequency range below and above the thermal superconducting transition temperature ($T_C \sim 35$ K). Compared with the reflectivity in the normal state (black), a clear reflectivity edge at 60 cm^{-1} appears below T_c (red) as the signature of interlayer Josephson tunneling of the Cooper-pairs.

In contrast, in the investigated sample $La_{1.675}Eu_{0.2}Sr_{0.125}CuO_4$, the insulating phase persists even below 10 K, showing no feature of Josephson plasmon shown in Figure 1.8(d). Remarkably, short after the resonant excitation the Cu-O stretching phonon mode in the CuO_2 planes at 20 THz, a clear plasma edge in the reflectivity shown up indicating the emergence of a nonequilibrium superconducting-like transport, which is reported in Figure 1.8(d). The light-induced plasma edge was measured to be at the same frequency as $La_{1.84}Sr_{0.16}CuO_4$ at equilibrium.

Another reporter of light-induced superconductivity was the transient optical conductivity. At equilibrium, the imaginary part of the optical conductivity σ_2 exhibiting a 1/ω behavior in the low-frequency THz regime, which acts as a reporter of the superfluid density and the capability to expel the interior magnetic field of a superconductor. In the light-induced state, the transient σ_2 also showed a 1/ω divergence in the low-frequency THz range, which evidence the emergency of a transient superconducting correlation above the equilibrium critical temperature.

To investigate the microscopic mechanism of the light-induced superconductivity in layered cuprates, a study of the transient structural change after the resonant excitation of the optical phonon was conducted. In resonant x-ray diffraction measurement, the dynamics of the stripe phase at (0.24 0 0.5) and the LTT distortion at (001) during the same vibrational excitation were monitored in quantitatively related $La_{1.875}Ba_{0.125}CuO_4$ through near the oxygen K-edge [5]. The dynamics of the peak intensity of the stripe phase are reported at the top of Figure 1.9(a). Nearly 70% decrease of that peak indicates the melting of the stripe order within 1 ps, which is consistent with the time scale of the onset of the light-induced superconductivity in $La_{1.675}Eu_{0.2}Sr_{0.125}CuO_4$. However, the modulation of the LTT phase (bottom) is much weaker and slower. A DFT calculation of the possible lattice distortion in the parent $LaCuO_4$ compound induced by the driven IR-active mode is plotted in Figure 1.9(c-d).

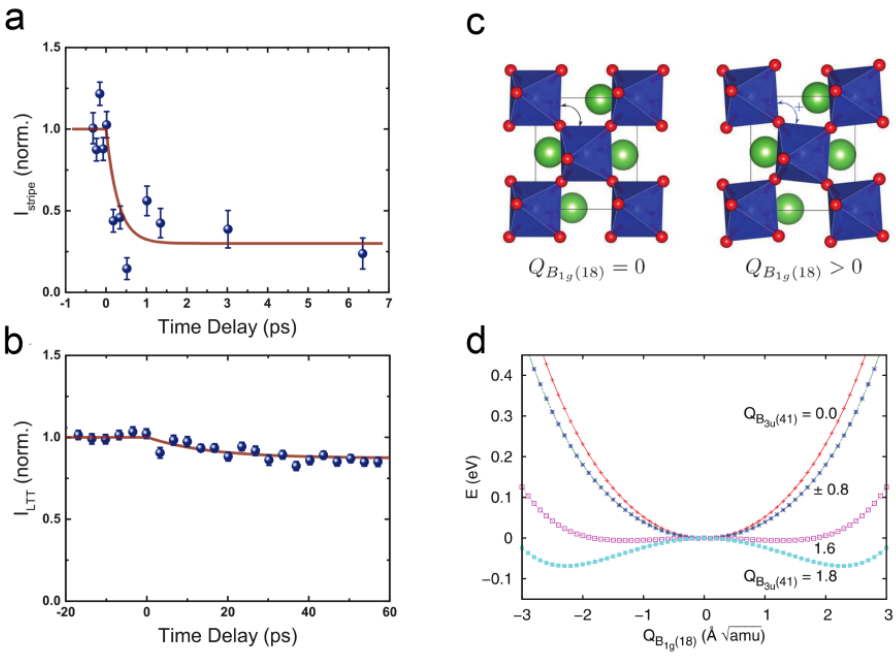

Figure 1.9. (a) Light-induced dynamic of the charge stripe order diffraction peak in $LBCO_{1/8}$. **(b)** Corresponding changes in the intensity of the diffraction peak associated with the LTT distortion in the same crystal under the same excitation conditions. Red lines: exponential fits with corresponding time constants. **(c)** Sketch of the atomic displacements of B_{1g} Raman mode in La_2CuO_4. **(d)** Differential energy potential of the coupled Raman mode through quartic coupling. Taken from[5] [21].

As aforementioned, the cubic coupling is forbidden by symmetry in $LaCuO_4$ [21], but a distortion into a lower crystal symmetry could be induced through the quartic nonlinear coupling $Q_{IR}^2 Q_R^2$. This coupling term could be sizable and distortion in the crystal structure could be induced if the amplitude of the IR-active mode is driven above a critical threshold. Possibly, the pump fluence at 2 mJ/cm^2 used in this experiment was below this threshold, which could only result in a tiny modulation of the crystal structure by other processes. Note that the LTT distortion plays a minor role in this process, excitation at near-infrared and optical wavelengths has also been observed to induce enhancement of superconductivity in striped compounds of the $La_{2-x}Ba_xCuO_4$ family [161]. Overall, these observations suggest that the vibrational excitation of the Cu-O stretching mode induce a nonequilibrium superconducting-like state in the stripe phase by melting the competing orders.

Enhancing the Josephson tunneling in bilayer cuprate

Light-induced superconductivity has also been observed in high-T_c bilayer $YBa_2Cu_3O_{6+x}$ compounds in their equilibrium pseudogap states following the vibrational excitation of the optical phonons. Figure 1.10(a) displays the crystal structure of $YBa_2Cu_3O_{6.5}$ with conducting

CuO_2 layers separated by the insulating Yttrium layers. Similar to the single-layer cuprates, Josephson plasma resonance appears in the THz reflectivity spectrum when the system becomes superconducting below T_c ~52 K. Along the crystal c axis, nonequivalent CuO_2 bilayers are intrinsically stacked, leading to the appearance of two Josephson plasma edges in the reflectivity accompanied with peaks at the plasma frequencies in the energy loss function in the superconducting state (Figure 1.10(b)).

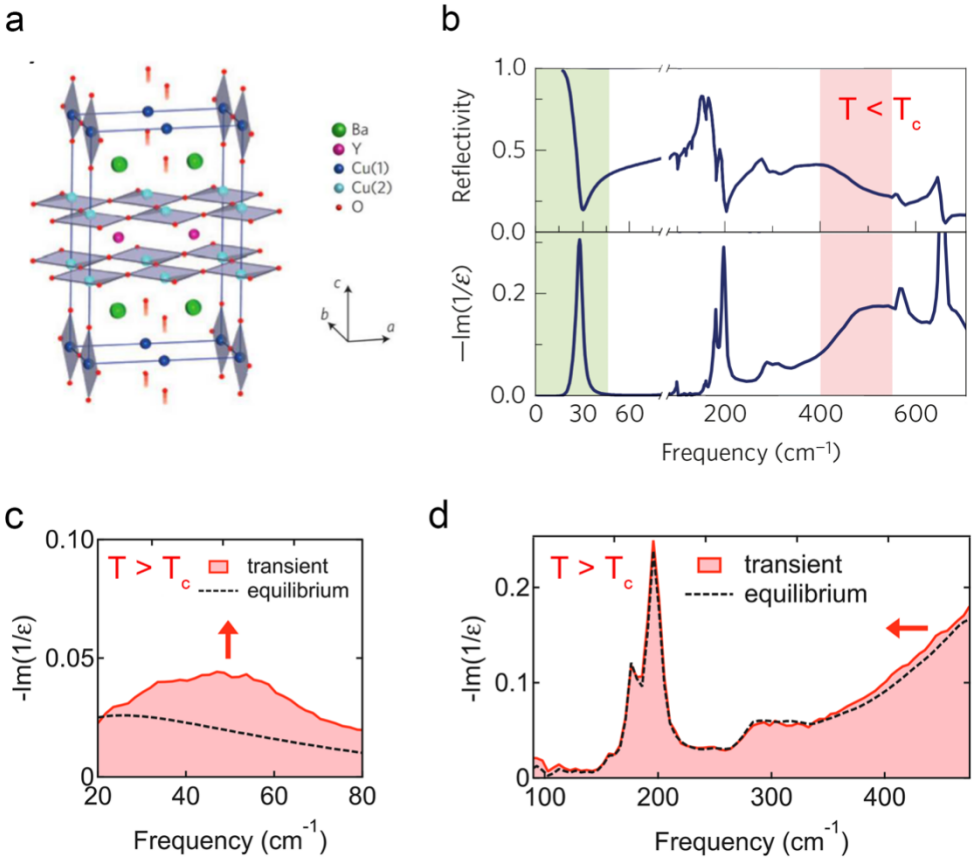

Figure 1.10. (a) Crystal structure of bilayer $YBCO_{6.5}$. **(b)** The reflectivity of $YBCO_{6.5}$ along the crystal *c* axis. Two longitudinal plasmons are highlighted with shadows. **(c)** Loss-function at 100 K with (red shadowed) and without (dashed) the vibration excitation of the apical-oxygen mode, indicating the enhancement of the inter-bilayer coupling. **(d)** Same quantity as (c), but in a higher frequency range. A reduction of intra-bilayer coupling is evidenced. Reproduced from [6].

Again, ultrafast THz spectroscopy has proven to be an effective probing method in recognizing the superconducting coherence in the transient light-induced state. A series of measurements have been performed on $YBa_2Cu_3O_{6+x}$ by monitoring the transient optical properties following the resonant excitation of the apical-oxygen stretching phonon mode along the crystal *c* axis. For example, Kaiser et al. demonstrated the enhancement of the Josephson tunneling in the superconducting state below T_c after the excitation of the apical-oxygen stretching mode with broadband THz pulses polarized along *c* axis [11]. Further, in

the normal state, a light-induced plasma edge at 1.5 THz appeared, indicating the emergence of the superconducting response after the THz excitation. Such vibrational control of the superconductivity has been observed in various of compounds with different doping levels. Another THz measurement by probing the broadband mid-infrared to THz frequency range was performed by Hu et al., in which the dynamics of both the longitudinal Josephson plasmons can be characterized [6]. As shown in Figure 1.10(b), the two Josephson plasma resonance locate at 30 cm^{-1} and 450 cm^{-1} in the reflectivity below T_c as highlighted. There are also clear features in the energy loss function ($-Im(1/\varepsilon)$), which can be the reporter of the coupling strength of the inter- and intra-bilayer Josephson junctions.

Figure 1.10(c-d) summarizes the experimental observations in terms of the change in energy loss functions. About 1 ps after the THz excitations, a peak appears at 50 cm^{-1} in the energy loss function at 100 K, indicating the emergence of a transient Josephson plasmon. In the meantime, a red-shift in the loss function of the higher frequency plasmon revealed a transfer of coherent spectral weight of superconducting carriers from the intra-bilayer to the inter-bilayer Josephson coupling (see Figure 1.10(d)).

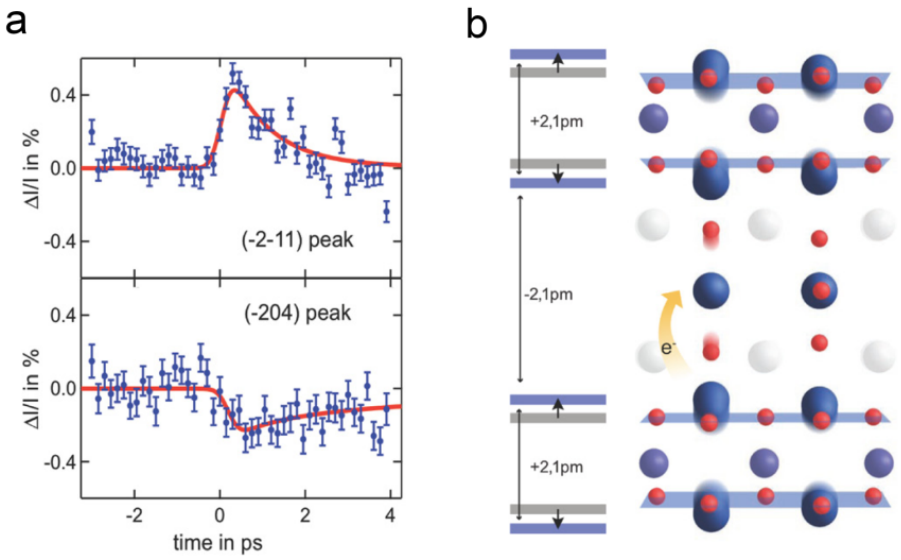

Figure 1.11. (a) Relative changes in the diffracted intensity of (-2-11) and (-204) Bragg peaks in $YBCO_{6.5}$ following the MIR resonant excitation. **(b)** Sketch of the reconstructed transient crystal structure at the peak signal. The redistributed layer distance of the Josephson layers is evidenced. Adapted from [13].

Notably, the emergence of the light-induced superconducting-like state is observed in the pseudogap phase, in which the precursor of the superconducting phase exists. The optical measurement in the THz range indicated an enhancement of the inter-bilayer Josephson tunneling at the expense of the intra-bilayer coupling, which could be interpreted if there is a

microscopic redistribution of the intra-bilayer and inter-bilayer distance following the THz excitation. To verify the speculation, a femtosecond hard x-ray diffraction experiment was carried out by R. Mankovsky et al. to investigate the connection between the lattice structural change and the light-induced superconducting-like state in $YBCO_{6.5}$ [10]. Overall four diffraction peaks were measured at 100 K using 50 fs x-ray pulses [13]. Typically, an increase and decrease of the (2-11) and the (-204) peaks were recognized following the resonant excitation of the out-of-plane Cu-O B_{1u} mode. Interestingly, the recovering time of both peaks is consistent with the lifetime of the transient superconducting-like state obtained from the terahertz experiments, which indicates a direct link between the light-induced coherent state and the transient lattice deformation.

A plausible explanation based on the coupling between the driven B_{1u} mode and another A_g Raman mode was proposed by the authors. Sizable displacement of the crystal lattice was predicted along the coordinates of the coupled Raman mode induced by vibrational excitation. The red curves in Figure 1.11(a) are the fits with the amplitude of the B_{1u} phonon as the fitting parameter. According to the sign and size in intensity change, the lattice distortion can be concluded. In Figure 1.11(b), ~2.1 pm decrease of the inter-bilayer distance and increase of the intra-bilayer distance were evidenced, while the distance of the apical-oxygen ions and copper atoms is reduced. The lattice dynamics can be interpreted in a picture describing the modulation of Josephson coupling of the intra- and the inter-bilayers. The decrease in inter-bilayer distance is supposed to enhance the tunneling between bilayers, corresponding to the emergence of the JPR in the low-frequency THz range. Furthermore, the increase in intra-bilayer distance can be associated with the observation by Hu et al. that the inter-bilayer tunneling is enhanced at the expense of coherent intra-bilayer coupling [6].

Summary

Intense mid-infrared light fields can be used to drive complex solids into transient crystal structures and hidden phases, which are not achievable at equilibrium. Experimental observations including vibrationally-induced metallicity, ferroelectricity, and superconductivity in transition metal oxides highlight the success and significance of this novel approach. Time-resolved x-ray crystallography has been exploited to gain insight into the nonequilibrium crystal structures, which potentially linked to light-induced phenomena. Theoretically, the anharmonic coupling between different vibrational modes is the key to understanding the connection between the structural changes and the light-induced phase.

Notably, strong-field THz light fields have shown the edge in controlling the phase of complex solids by exciting optical phonons higher than 15 THz. However, perovskite materials such as cuprate $YBa_2Cu_3O_{6.5}$ and manganite $P_{0.7}Ca_{0.3}MnO_4$ exhibit further lower-frequency vibration modes in the so-called "THz-gap" between 5 and 15 THz (Figure 1.12), which could be used to control phases and induce new physical processes. Due to the strong absorption in nonlinear crystals, it is difficult to drive these modes to a large-amplitude with the THz fields generated from the table-top laser source. The realization of vibrational phase control via resonant excitation of the low energy vibrational modes becomes the goal of this thesis.

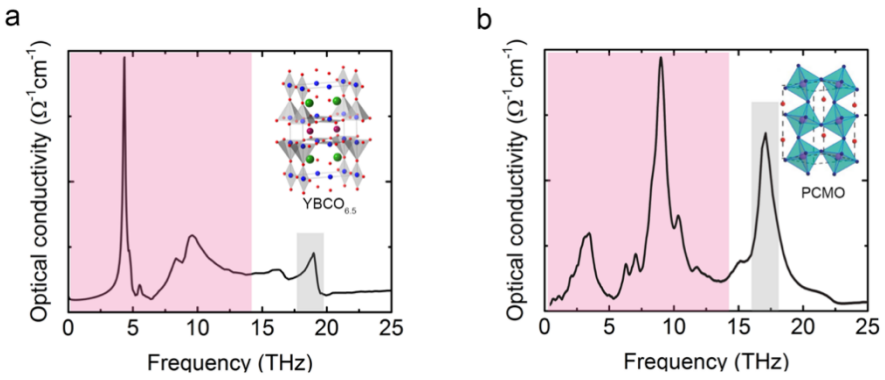

Figure 1.12. Optical conductivity along c direction in (a) $YBa_2Cu_3O_{6.5}$ and (b) $Pr_{0.7}Ca_{0.3}MnO_3$. The phonons investigated previously are highlighted in grey. Low energy phonons in the THz-gap range are highlighted in red. Insets, crystal structures for $YBa_2Cu_3O_{6.5}$ and $Pr_{0.7}Ca_{0.3}MnO_3$ [1].

Chapter 2

2. Generation of intense narrowband CEP-stable THz pulses

In this chapter, I will first review the basic principles of intense THz generation. Then, I will give the details on the narrowband THz generation based on chirped-pulse frequency mixing in large-piece nonlinear organic crystals. This principle was used to achieve vibrational phase control of the high-T_c cuprate superconductor presented in Chapter 4.

2.1 Basic principles of intense THz pulse generation

Due to the development of high-power ultrafast laser techniques, scientists are able to investigate the dynamics of materials on femtosecond and even attosecond time scales [36]. Ultrafast THz spectroscopy is a powerful state-of-art technique to study both the linear and nonlinear response of complex materials [37]. Intense THz light sources are effective in driving the materials into nonlinear regimes because of their strong electric field. For different applications, desired THz light fields can be achieved either by Free-electron lasers or frequency-mixing in nonlinear optical crystals.

2.1.1 Free-electron lasers

Free-electron lasers (FELs) are large facilities, which can produce tunable, brilliant, and coherent high-power radiation with the wavelengths spanning from the far-infrared to hard x-rays. Figure 2.1(a) sketches the FEL-based THz source (ELBE) in Dresden-Rossendorf, which contains three main components: accelerator, undulator and optical resonator [40]. The high-energy electron bunches from the accelerator are steered into the undulator by a magnet. The wiggling electrons are confined in an optical resonator to enhance the interaction of photons and electrons. This FEL can be operated in the range of 18-250 microns wavelength with pulse energy between 0.01 to 2 uJ and pulse duration from 1 to 25 ps [40].

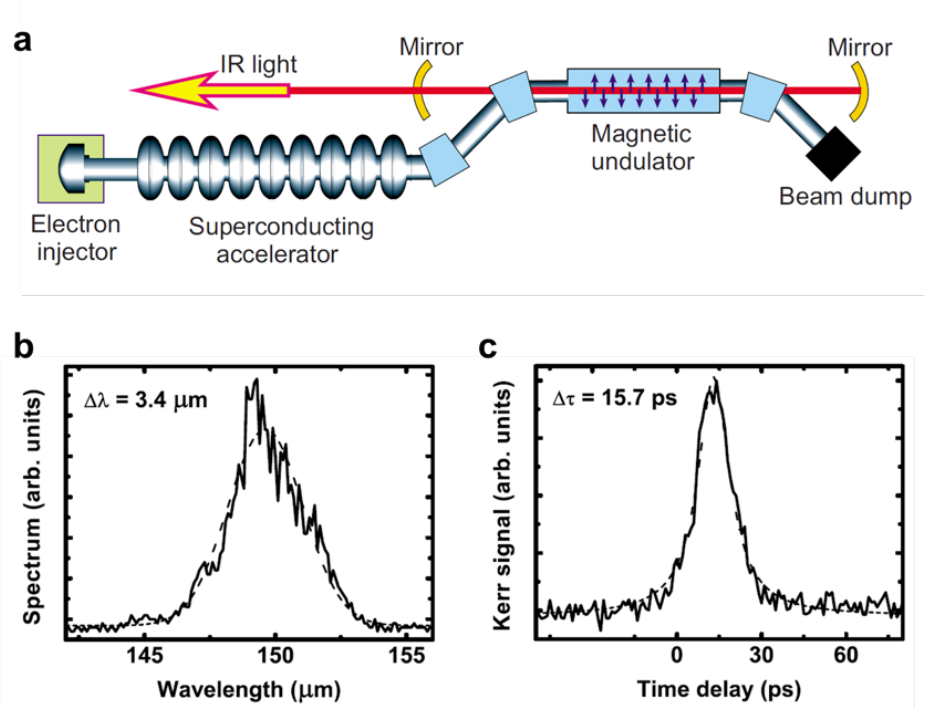

Figure 2.1. (a) Schematic view of the free-electron laser in the FZD. **(b)** Measured spectrum of the FEL at 150-μm wavelength. **(c)** The Electro-optic sampling of the free electron laser pulses in a ZnTe crystal. The FWHM of the Kerr signal reveals a pulse duration of ~ 16 ps. Taken from Ref. [40].

However, FELs cannot provide few-cycle THz transients with a controllable carrier envelope phase [43]. Besides, the tuning of the operation frequency in FELs is quite difficult. So far, it is impossible for most of the scientists to have unlimited access to the FELs THz sources.

2.1.2 Frequency mixing in nonlinear optical crystals

Unlike the FELs, the laser-based THz sources are more compact and able to generate CEP stable pulses. Field strength of up to 100 MV/cm can be achieved by exploiting difference frequency generation (DFG) or optical rectification (OR) processes in nonlinear crystals. Basic principle of these two nonlinear processes will be discussed below.

The polarization induced P_i in general nonlinear materials can be described as a function of the applied electric field E

$$P_i = \varepsilon_0 \chi_{ij}^{(1)} E_j + \varepsilon_0 \chi_{ijk}^{(2)} E_j E_k + \varepsilon_0 \chi_{ijkl}^{(3)} E_j E_k E_l + \ldots \tag{2.1}$$

where $\chi^{(1)}$ denotes the linear susceptibility, while $\chi^{(2)}$ and $\chi^{(3)}$ correspond to the nonlinear susceptibilities of the second and the third order, respectively. The susceptibility tensor coefficients are dependent on the frequency of the involved interacting electric fields E. Then the induced polarization can be separated into two contributions

$$P_i = P_L + P_{NL} \tag{2.2}$$

where P_L and P_{NL} represent the linear and nonlinear response, respectively. If we only take the second-order nonlinear term into consideration and omit the spatial and temporal dispersion, P_{NL} can be written as

$$P_{NL} = \varepsilon_0 \chi_{ijk}^{(2)} E_j E_k = 2\varepsilon_0 d_{eff} E(\omega_1) E(\omega_2) \tag{2.3}$$

where $E(\omega_1)$ and $E(\omega_2)$ denote the interacting electric field with frequency at ω_1 and ω_2. Figure 2.2 illustrates the two principle second-order nonlinear processes, which are sum-frequency generation and difference-frequency generation.

Difference-frequency generation (DFG)

I will focus on the DFG process, in which the difference frequency of the interacting electric field $E(\omega_1)$ and $E(\omega_2)$ lies in the THz range. For efficient generation at ω_3 (or ω_{THz}) the phase matching condition $\Delta k \approx 0$ should be well satisfied

$$\Delta k = k_{THz} - (k_1 - k_2) \tag{2.4}$$

where k_{THz} stands for the wavevector of the THz beam; k_i (i = 1,2) are the wave vectors of the interacting optical fields. The phase-matching condition can be quantified by the coherence

length l_c, which defines the maximum interacting length in the nonlinear crystal. In the simplest collinear geometry, the coherence length is given by

$$lc = \frac{\pi}{|\Delta k|} = \frac{1}{2}\left(\frac{n_{THz}}{\lambda_{THz}} - \frac{n_1}{\lambda_1} + \frac{n_2}{\lambda_2}\right)^{-1} \tag{2.5}$$

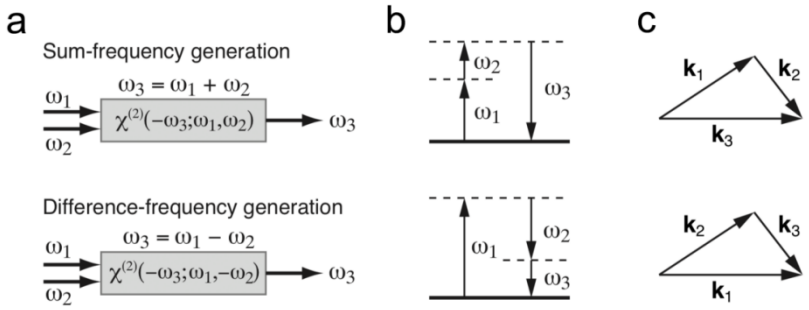

Figure 2.2. (a) Schematic illustration of two principle second-order nonlinear processes: sum-frequency generation and difference frequency generation. (**b**) Corresponding photon energy conservation. (**c**) Corresponding wavevectors satisfying the phase-matching condition. Adapted from [49].

In addition, (2.5) can be simplified in the case THz generation, in which the refractive index dispersion is relatively small. With $n_2 = n_1 + (\partial n/\partial\lambda)(\lambda_2 - \lambda_1)$, (2.5) can be rewritten by

$$lc = \frac{\lambda_{THz}}{2(n_{THz} - n_g)} \tag{2.6}$$

where $n_g = n_1 - (\partial n/\partial\lambda)\lambda_1$ denotes the group index of the optical wave. In the best phase-matching condition and ignoring the pump-light absorption, the conversion efficiency is given by [50]

$$\eta_{THz} = \frac{\omega_{THz}^2 d_{THz}^2 L^2 I_0}{2\varepsilon_0 c^3 n_0^2 n_{THz}} exp\left(-\frac{\alpha_{THz} L}{2}\right)\left(\frac{sinh\,(\alpha_{THz} L/4)}{\alpha_{THz} L/4}\right)^2 \tag{2.7}$$

$d_{THz} = \frac{1}{4} n_0^4 r$ accounts for the NLO coefficient for THz generation which scales with the electro-optic coefficient r. L, I_0, α_{THz} and n_0 denote the length of the crystal, the pump intensity absorption, coefficient at the THz and optical frequencies, respectively. The figure of merit (FOM) for THz-wave generation FM THz can be defined as

$$FM_{THz} = \frac{d_{THz}^2}{n_0^2 n_{THz}} = \frac{n_0^6 r^2}{16 n_{THz}} \tag{2.8}$$

Difference frequency generation in semiconductor emitters

Most of the vibration modes in solids are exhibited in the MIR frequency range. Novel OPA-based laser sources have been used to generate widely tunable multi-cycle MIR-THz pulses via DFG in semiconductors, such as GaSe and $AgGaS_2$. Transmission in GaSe crystal is almost flat in a broad frequency range above 15 THz, below which good phase matching couldn't be reached due to strong phonon absorption in the materials. Efficient MIR generation up to 70 THz can be phase-matched by tuning the angle of GaSe. The energy band gap of GaSe is typically ~ 2.1 eV (~ 590 nm), so that pump wavelength longer than 1180 nm is required in the DFG process in order to avoid two-photon absorption. On the other hand, $AgGaS_2$ crystal has a higher bandgap at 2.75 eV (~ 450 nm), in which the two-photon absorption will only be pronounced when the pump is shorter than 900 nm. Laser pulses at 1 μm wavelength delivered from Yb: YAG amplifier system, can be used to directly pump $AgGaS_2$ and better energy conversion efficiency can be achieved.

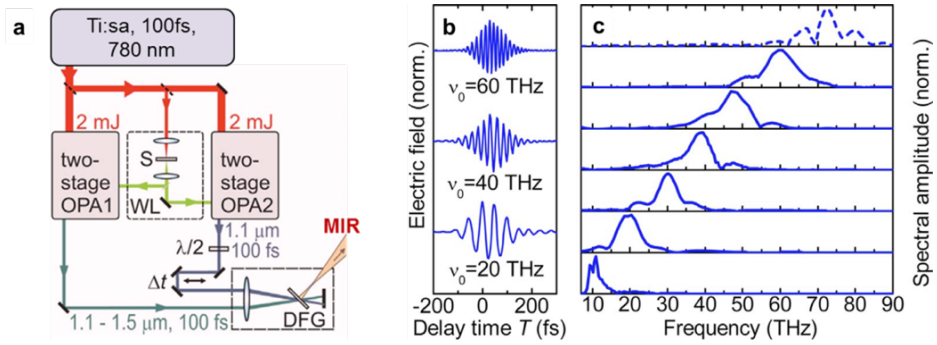

Figure 2.3. (a) Intense MIR setup based on frequency mixing in GaSe crystal. S, sapphire window; WL, white-light seed for OPA1 and OPA2; DFG, non-collinear difference frequency mixing of both OPA outputs. **(b)** Real-time transients and **(c)** normalized amplitude spectra for widely tuned center frequencies, generated by DFG of the signal waves of both OPAs. Emitter: GaSe (length: 140 μm, all solid curves) or $AgGaS_2$ (length: 800 μm, broken curve). Adapted from Ref. [43].

For broadband tunability, the most straightforward way is to tune the energy difference of the signal and idler beam of the OPA and mix them in nonlinear crystals. Pulse energy up to hundreds of μJ can be achieved based on Ti:sapphire or Yb: YAG amplifiers. However, in this parametric process, the signal and idler are not mutually phase-locked, so the carrier envelope phase of the generated pulses is not controllable. Difference frequency mixing between the signal waves of two optical parametric amplifiers (OPAs) seed by the same white light continuum can generate CEP-stable THz pulses with field strength up to 100 MV/cm [43]. In Figure 2.3, by fixing the pump wavelength at 1.1 μm and varying the signal

wavelength between 1.1 μm and 1.5 μm, waveforms with carrier frequencies spanning from 10 to 72 THz has been generated. Peak fields up to 108 MV/cm and pulse energies as high as 19 μJ has been achieved with type-II DFG in this material.

Optical rectification (OR)

The optical rectification process is a special situation for the DFG process with the two interacting electric fields oscillating close to a degenerated frequency. Instead of using two pump beams, THz radiation is generated via optical rectification by pumping the nonlinear crystal with a single broadband pump pulse. A near transform-limited ultrashort laser pulse in the sub-picosecond range intrinsically occupies a broadband spectrum, within which different frequencies components can mix with each other in a nonlinear material and produce a broadband THz pulse.

In the perfect phase-matching condition with the plane-wave approximation, the conversion efficiency of the generated THz wave is simplified as

$$\eta_{THz} = \frac{\omega_{THz}^2 d_{THz}^2 L^2 I_0}{2\varepsilon_0 c^3 n_0^2 n_{THz}} = \frac{1}{2\varepsilon_0 c^3} FM_{THz} \omega_{THz}^2 I_0 L^2 \tag{2.9}$$

Table 2.1 Relevant properties of widely used materials for THz generation via optical rectification. The parameters showing here are refractive index n_o and group index n_g at the pump optical wavelength λ; refractive index n_{THz} in the THz range; the electro-optic coefficient r; the NLO coefficient d_{THz} and the figure of merit FM_{THz} for THz-wave generation FM_{THz} [49].

Material	n_o	n_g	n_{THz}	r (pm/V)	d_{THz} (pm/V)	FM_{THz} $(pm/V)^2$	λ (nm)
DAST	2.13	2.26	~ 2.3	47	240	5600	1500
DSTMS	2.08	2.19	~ 2.2	50	230	5800	1500
OH1	2.16	2.33	~ 2.3	52	280	7500	1300
ZnTe	2.85	3.2	~ 3.2	4	66	170	800
GaP	3.12	3.36	~ 3.35	1	24	17	1000
$LiNbO_3$	2.16	2.22	~ 5.0	30	160	1100	1000

Relevant properties of widely used materials for THz generation via optical rectification are listed in Table 2.1. ZnTe and GaP have much lower electro-optic coefficients compared to the best inorganic electro-optic crystals such as $LiNbO_3$. Assisted by the pulse-front-tilting technique, the phase-matching condition is dramatically improved and up to hundreds of μJ

THz pulses can be achieved [52]. Compared with inorganic materials, molecular organic materials are attractive due to large nonlinear susceptibilities, ultrafast response times and almost unlimited design possibilities [63]. Efficient THz generation in organic crystals DAST, DSTMS, OH1 can be phase-matched using pulses between 1300 and 1560 nm. Laser sources such as optical parametric amplifiers [71], Cr: Forsterite laser amplifiers [75][80][81] or even cheap telecommunication fiber lasers [82] are good candidates for the pump source.

Optical rectification using the tilted pulse front technique in $LiNbO_3$

Lithium Niobate ($LiNbO_3$) has larger THz nonlinear susceptibility ($|d_{33}|$= 27 pm/V) [59], which becomes a good option in strong-field THz generation. It has a much larger bandgap, which allows high power excitation in the optical rectification process without sizable two-photon absorption. However, the THz waves, which take the form of phonon-polariton waves in $LiNbO_3$, have a large phase-velocity mismatch, which makes the collinear velocity matching impossible. Recently, the tilted pulse-front technique was introduced to overcome the phase-matching problem by diffracting the NIR pulses off a grating. The generated THz radiation by the tilted pulse front method will propagate perpendicularly to this front with a velocity v_{THz}

$$v_{THz} = v_{NIR}^{gr} * \cos\gamma. \tag{2.10}$$

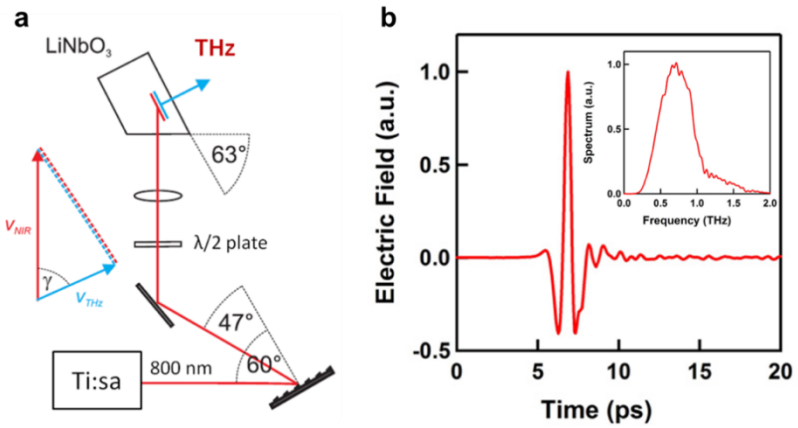

Figure 2.4. (a) The pulse front of near-infrared pulses at 800 nm generated from a Ti:sapphire laser amplifier is tilted by an angle of γ to fulfill the phase matching condition. The pulse front tilting is achieved by diffracting the beam off a grating at an incident angle of 60 degrees. **(b)** Characterization of the generated THz pulse via electro-optical sampling. Inset, the corresponding Fourier transform of the measured electric field.

The velocity matching condition can be fulfilled by choosing the angle γ. Figure 2.4(a) sketches the THz generation setup pumped by front-tilted 800 nm pulses generated by a Ti:sapphire laser. After the diffraction from the grating, the polarization of the 800 nm beam

is rotated 90 degrees. A lens is placed to image the laser spot on the $LiNbO_3$ crystal. The generated THz pulse is propagating perpendicular to the crystal surface. The electro-optical sampling of the generated THz pulse and the corresponding Fourier spectrum are presented in Figure 2.4(b). The conversion efficiency persists with relatively high pump power and can be further improved by cooling the crystal to reduce the THz absorption [55][56]. In the meanwhile. the bandwidth could be narrowed down via chirped-pulse DFG in $LiNbO_3$ single crystal [60], or periodically poled $LiNbO_3$ (PPLN) [52][60]-[62].

Optical rectification in large organic crystals

Large organic crystals with significant nonlinear susceptibility and low absorption in the THz range open up new possibilities in THz generation. THz waves generated via optical rectification in organic crystals has been first demonstrated in DAST crystals in 1992 and investigated by many other researchers [63]. More novel organic crystals have been manufactured and commercialized, such as DSTMS [69], OH1 [71], HMQ-TMS [75], BNA [78]. The properties of widely used materials for THz generation are listed in Table 2.1, in which the organic crystals show clear edges over the conventional nonlinear crystals.

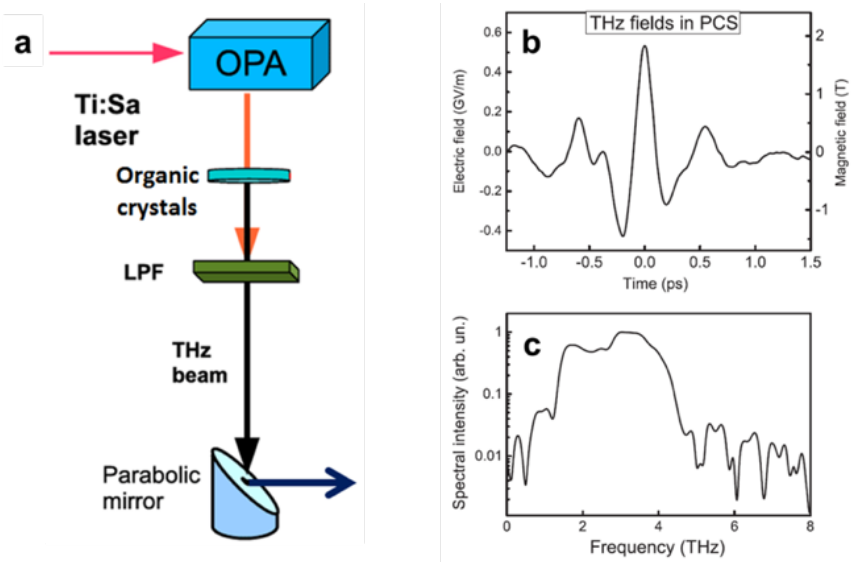

Figure 2.5. (a) Tabletop terahertz source based on the partitioned DSTMS. The crystal is pumped by an optical parametric amplifier (OPA). The THz beam is separated from the residual pump by a low-pass filter (LPF). THz electric field **(b)** and corresponding spectrum **(c)** obtained by optical rectification in a patterned DSTMS crystal structure. Adapted from Ref. [69].

Good phase-matching condition in organic crystals requires NIR beams beyond 1 μm, which can be obtained from optical parametric amplifier [71], Cr: Forsterite laser amplifier[75], or fiber laser at telecommunication wavelengths [82]. In Figure 2.5, single-

cycle THz fields up to GV/m between 1 and 5 THz can be achieved in large piece partitioned DSTMS crystal powered by NIR pulses generated from laser-driven optical parametric amplifier [69]. However, due to the vibration modes in the nonlinear organic material, the strong absorption peaks for certain THz frequencies will make the perfect phase-matching condition unreachable. One possibility to reduce the absorption is cooling down the organic material with the cryogenic system [83]. But the usage of coolant and cryostat makes the setup more complicated, while the organic crystals are not stable at low temperature due to the chemical composition,

The variety of the optical properties in the THz range in different organic crystals can be used to fill the THz-gaps. In Figure 2.6, the coherence lengths of THz generation in the DFG process with different pump frequencies are depicted for DAST, DSTMS and OH1 crystals. In a broad range up to 11 THz, DAST shows good phase-matching around 1400 - 1500 nm, except for 1.1 THz. As a derivative material from DAST, DSTMS shows similar coherence length and the phase-matching condition is quite improved around 1 THz due to heavier anions [84]. On the other hand, OH1 has the highest figure of merit for THz generation below 3 THz with an optical pump longer than 1 μm.

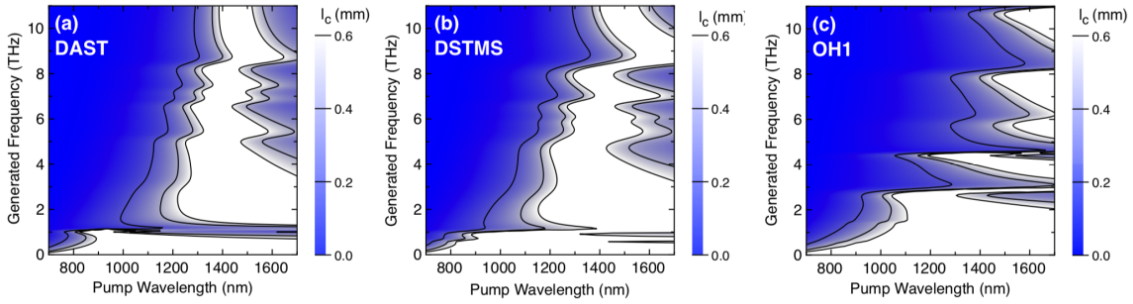

Figure 2.6. Coherence length for THz generation in (a) DAST; (b) DSTMS; (c) OH1 as a function of the pump optical wavelength and the generated THz frequency. Adapted from Ref. [49].

Different approaches based on difference frequency generation have been attempted to reach the higher THz frequencies. Narrowband nanojoule THz pulses widely tunable between 1 and 20 THz were produced by difference-frequency mixing the signal and idler beams from a nanosecond OPO [85]. THz pulses above 10 THz via DFG between the signal and idler of sub-picosecond OPAs were generated in DAST [86]. Unfortunately, these THz fields are not strong enough for the vibration phase control in complex materials.

Compared with the FEL-based THz source, intense MIR-THz pulses can be generated via frequency mixing in the laser-based setup using nonlinear crystals. Figure 2.7 summarizes the table-top approaches in generating intense MIR-THz pulses. Notably, due to the strong

absorption in the nonlinear crystals, in the spectral range between 5 and 15 THz, which is referred to as "THz-gap", an efficient table-top source is still not available.

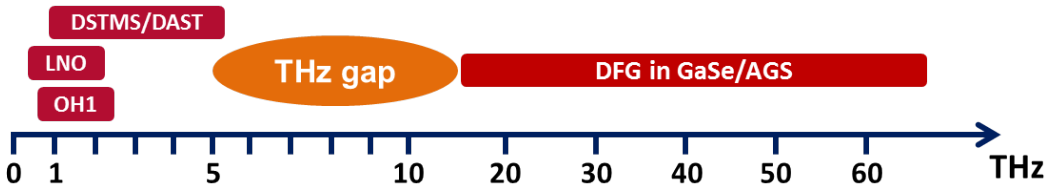

Figure 2.7. General table-top techniques of intense THz pulses generation. Below 5 THz, Optical rectification are widely used in ferroelectric material (e.g. $LiNbO_3$) and large piece of organic crystals (OH1, DSTMS, DAST). Above 15 THz, frequency mixing using near-infrared pulses can be exploited in semiconductor emitters like GaSe, $AgGaS_2$. Efficient light source in the "THz gap" is still on demand.

2.2 Demonstration of difference frequency generation in organic crystals

Aiming at vibrational phase control of complex materials, a new approach to produce intense narrowband MIR-THz exploiting DFG in organic crystal DSTMS using chirped near-infrared pulses from two mutually phase-locked OPAs was investigated. This was used to generate a narrowband tunable THz source across the THz-gap.

2.2.1 Bandwidth control in difference frequency generation

Notably, general techniques can deliver MIR-THz pulses with relative bandwidths between 10% - 30%. However, the typical linewidth of the vibrational modes ($\frac{\Delta\upsilon}{\upsilon_0}$) in complex materials is in the order of only a few percent. It is crucial to reduce the bandwidth to drive the target modes independently and effectively. One can either reduce the bandwidth of the interacting NIR pulses or filter the generated THz with bandpass filters. However, the pulses generated with these approaches are usually not sufficiently strong enough to effectively excite the vibrational modes. Besides, the spectrum bandwidth of the MIR-THz pulses will not easy to be tuned in both cases, which makes it difficult to selectively excite different phonons. The generation of ultrashort (< 1 ps) frequency (1- 30 THz) and bandwidth (< 5 %)

tunable MIR-THz pulses with high electric field (> 1 MV/cm) is on-demand in our experiment.

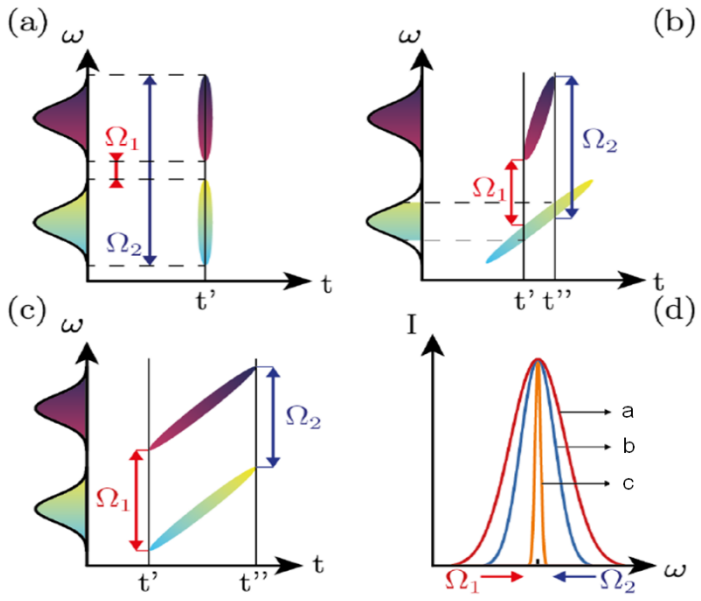

Figure 2.8. Principle of the narrowband MIR pulse generation. (a-c) Time-frequency Wigner distributions of the interacting NIR pulses for various chirp configurations; the THz components are generated at the difference frequency between NIR spectral frequencies at the same time delay. Ω_1 and Ω_2 are the lowest and highest MIR frequencies, respectively. **(d)** Corresponding MIR spectra. For configuration (a-c). Adapted from Ref. [97].

Another approach to generating ultrashort narrowband pulses is chirped pulse DFG in nonlinear crystals. Narrowband pulses can be efficiently generated via nonlinear interaction between chirped broadband pulses. This approach has been demonstrated in the generation of narrowband visible pulses via the sum frequency generation of NIR pulses with opposite chirp [93] and narrowband THz pulses by difference frequency generation between NIR pulses with opposite chirp [94][96].

The principle is elucidated in Figure 2.8. Two interacting NIR pulses as a functon of time and frequency are sketched in (a-c). The generated THz spectrum bandwidth will be determined by Ω_1 and Ω_2, which are the lowest and highest MIR frequencies, respectively. In the case of broadband generation, two NIR beams are consisted with near transform-limited pulses, all frequency components of the two beams will interact at the same time delay with the maximum frequency bandwidth. If two pulses are linearly chirped, the THz bandwidth will be narrowed because the interacting frequency components are reduced. If the same amount of dispersion is introduced to the two pulses, the narrowest spectrum can be achieved

in (c). Schematic drawings of THz generation processes for broadband and narrowband excitation pulses via are shown in Figure 2.9.

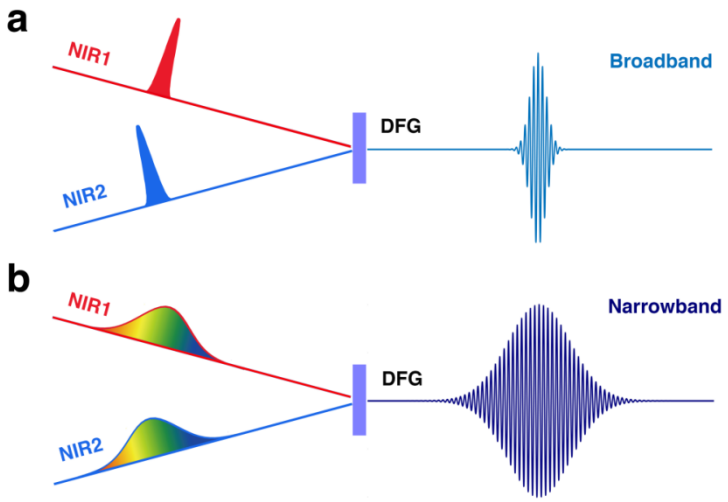

Figure 2.9. Schematics of the generation processes for (a) broadband and (b) narrowband THz pulses.

Our approach to intense narrowband MIR-THz is DFG in the organic crystal using chirped pulses. By stretching the near-IR pulses, we get rid of the THz light generated by the individual NIR beam via optical rectification, which significantly improves the efficiency. The optical parametric amplifiers, NIR stretchers and the DFG process in nonlinear organic crystal DSTMS will be discussed in the follows.

2.2.2 Technical approaches used for narrowband THz source

Organic crystal DSTMS

Organic crystals based on the charged chromophores and strong Coulomb interaction have several advantages over non-ionic crystals. They have large molecular nonlinearity and a higher tendency to override the dipole-dipole interactions, which could form non-centrosymmetric macroscopic packing [49]. The most widely investigated crystal is DAST, which has large second-order nonlinear optical susceptibilities $\chi_{111}^{(2)}$= (420±110) pm/V at 1.9 μm. However, it is still challenging to reduce the growing time of high optical quality DAST with large dimensions, which usually takes several months.

As a derivative compound of DAST, DSTMS ($C_{25}H_{30}N_2O_3S$) has the monoclinic space group Cc and shows rather higher solubility in methanol. Larger pieces of DSTMS crystals can be grown with a spontaneous nucleation method or the seeded solution growth method in several weeks. Figure 2.10(a-c) depict large piece DSTMS, molecular structures with the dominant sample morphology.

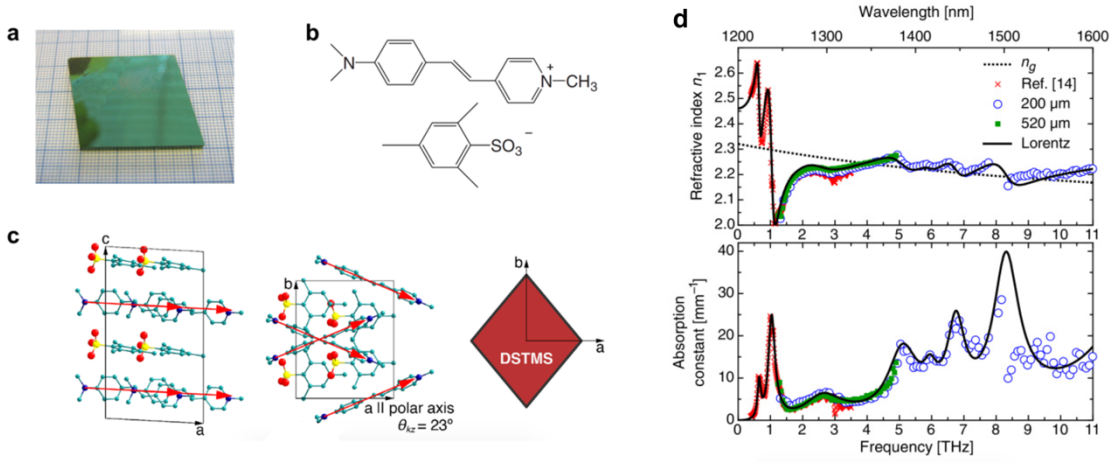

Figure 2.10. **(a)** DSTMS bulk crystal, the large surface is the (001) face. **(b)** Molecular structures [90] and **(c)** the dominant sample morphology of DSTMS [49]. (**d)** Terahertz refractive index and absorption of DSTMS crystals for polarization parallel to the polar a-axis. Adapted from [92].

DSTMS is another good choice in generating higher frequency THz, due to its good group velocity matching for broadband THz range at 1350 - 1560 nm pump wavelength (Figure 2.10(d)). However, the melting point of the material is only 258 degrees and the damage threshold is ~ 100 GW/cm^2, which is much lower than inorganic nonlinear crystals. So far, the only approach to high pulse energy THz generation is to enlarge the crystal size and the lower the pump intensity. On the other hand, stretched near-infrared with much lower peak intensity can also be used to pump the organic crystals for THz generation, which will be discussed later.

Optical parametric amplifier system

DSTMS crystal has good group velocity matching with 1350 - 1560 nm pump pulses, which can be effectively generated from the optical parametric amplifier (OPA) pumped by Ti:sapphire system. The OPA system behaves as a high-efficiency frequency converter, from 800 nm to 1.3 ~ 1.55 µm for the phase-matching. Two parallel OPAs work as frequency

converters are seeded by the same white-light continuum producing signal beams with a relatively-locked carrier-envelope phase.

In Figure 2.11(a), the optical parametric amplification process can be comprehended in the picture of energy and momentum conservation of different photons. A pump photon excites a virtual energy level which is stimulated by a signal photon. This results in the emission of an identical second signal photon and an idler photon [98][99].

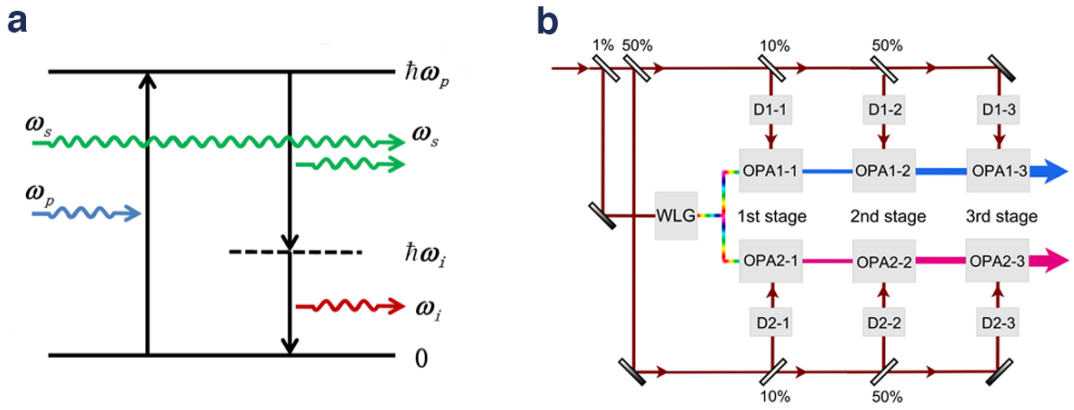

Figure 2.11. (a) Photon picture of optical parametric amplification: stimulated emission of signal photons from a virtual level excited by the pump photons. **(b)** Schematic of the two OPAs used in the narrowband MIR-THz source. WLG: white light generation. DL: delay stage. Nearly 1% energy of the 6-mJ pulses is used for generating white light pulses in a sapphire plate. The generated white light is split and seed the two parallel 3-stage OPAs. Around 3 mJ 800 nm pulses are used for pumping each of the OPAs and approximately 0.9 mJ signal pulses can be generated in the spectra range of 1.3 ~ 1.55 μm.

For high conversion efficiency, two parallel 3-stage OPA seed by the same super-continuum are designed in our lab. In Figure 2.11(b), about 6 mJ pulses at 800 nm with horizontal polarization are steered into the OPA system. Nearly 1% of the energy is used for generating stable white-light continuum in a 5-mm sapphire plate. The polarization of the super-continuum is 90 degrees rotated. Type II phase-matching is exploited for all the OPA stages to take advantage of the high nonlinear susceptibility of the BBO crystals. All the BBO crystals are cut with $\theta = 29.2°, \varphi = 0°$. The amplification in the first OPA stage is performed in 2-mm type-II BBO crystals, with slightly focusing s-polarized seed pulses and p-polarized pump pulses. The amplified signal beam from the seed is separated from the generated idler beam and residual pump beam using metallic irises. The output pulse energy varies from 15 μJ to 30 μJ from 1550 nm to 1350 nm.

Collinear phase-matching is achieved with collimated pump and signal beams sent to the second and third OPA stages. The parametric amplification process takes place in 3 mm (2^{nd} stage) and 2.5 mm (3^{rd} stage) BBO crystals, which are equally pumped by the remained

fundamental beams. Both the OPAs deliver pulses with a maximum energy of 850 - 900 μJ tunable between 1550 nm and 1350 nm, corresponding to a photon-conversion efficiency around 50%, with better performance than the commercial designs.

Near-IR pulse stretching technique

The phenomenon of delaying or advancing some wavelengths relative to others is referred to as chirp or group delay dispersion (GDD). Electro-magnetic wave at an angular frequency ω can be written in plane-wave solution:

$$\tilde{E}(\omega) = |\tilde{E}(\omega)| exp\ (i\Phi(\omega)) \tag{2.11}$$

where $|\tilde{E}(\omega)|$ represents the amplitude and $\Phi(\omega)$ the spectrum phase. (2.11) can also be described as a function of wavevector $k(\omega) = \frac{\omega}{c/n(\omega)}$

$$\Phi(\omega) = k(\omega)z = \frac{\omega z}{c/n(\omega)} \tag{2.12}$$

Particularly, for an ultrashort pulse propagating in a dispersive medium, this frequency-dependent phase can be expanded as

$$\Phi(\omega) = \Phi(\omega_0) + \frac{\partial\Phi(\omega)}{\partial\omega}|_{\omega_0}(\omega - \omega_0) + \frac{1}{2}\frac{\partial^2\Phi(\omega))}{\partial\omega^2}|_{\omega_0}(\omega - \omega_0)^2 + \cdots \tag{2.13}$$

The velocity of a certain monochromatic wave is defined as group velocity, which gives $v_g = [\partial\Phi(\omega)/\partial\omega]|_{\omega_0}$. The delay of the group velocity is defined as group delay (*GD*):

$$GD(\omega_0) = \frac{\partial\Phi(\omega)}{\partial\omega}|_{\omega_0} = z\frac{\partial k}{\partial\omega}|_{\omega_0} \tag{2.14}$$

Then the group delay dispersion (*GDD*) can be defined as the second-order expansion coefficient

$$GDD(\omega_0) = \frac{\partial^2\Phi(\omega)}{\partial\omega^2}|_{\omega_0} = z\frac{\partial^2 k}{\partial\omega^2}|_{\omega_0} \tag{2.15}$$

Higher-order dispersion, i.e. the third-order dispersion (TOD), will not be discussed in this chapter.

For a Gaussian pulse oscillating at ω_0 with pulse duration of τ_{in}, the pulse shape will still be Gaussian after a linearly dispersive component with pulse duration τ_{out}, which is given by

$$\tau_{out} \sim \tau_{in}\sqrt{1+(\frac{GDD(\omega_0)}{\tau_{in}})^2} \tag{2.16}$$

Narrowband pulses THz were generated using linearly chirped pulses with different approaches. Linear chirp can be introduced to the NIR beams propagating in highly dispersive materials such as ZnSe, CdTe and Si [97][100]. However, there are disadvantages, for example, the introduced chirp is fixed for certain wavelength by the length of the dispersive materials. Further, the intensity of the propagating beam has to be lowered to avoid even higher order dispersion and self-phase modulation (SPM). On the other hand, chirp mirror pairs can be used to introduce linear negative chirp, however, high-quality chirp mirrors beyond 1 μm are usually not available.

Stretchers and compressors composed of gratings or prism pairs can continuously introduce linear dispersion. Prism pairs with transparent dispersive materials like SF-10 can be used for a broadband spectrum range. However, compact geometry is not achievable. Metallic gratings are widely used to compress and stretch pulses, especially in the commercial femtosecond laser system. However, the diffraction efficiency in the range between 1.3 μm and 1.55 μm is unfortunately quite low.

Interestingly, the transmission gratings designed for telecommunication wavelengths with low loss and high damage threshold can be used in our approach. A stretcher consisted of four pieces of transmission gratings is depicted in Figure 2.12. This geometry is compact and it is additionally easy to switch from broadband to narrowband generation. The total amount of negative dispersion is described as

$$GDD(\omega_0) = -\frac{4m^2\pi^2c\Lambda^2}{\omega_0^3}[1-(-m\frac{2\pi c}{\omega_0}-\ sin\,(\theta))^2]^{-3/2}L_g \tag{2.17}$$

where ω_0, m, Λ, θ, and L_g denote the central frequency of the wave packet, the diffraction order, the grating period, the incident angle on the first grating, and the separation between each grating pairs, respectively.

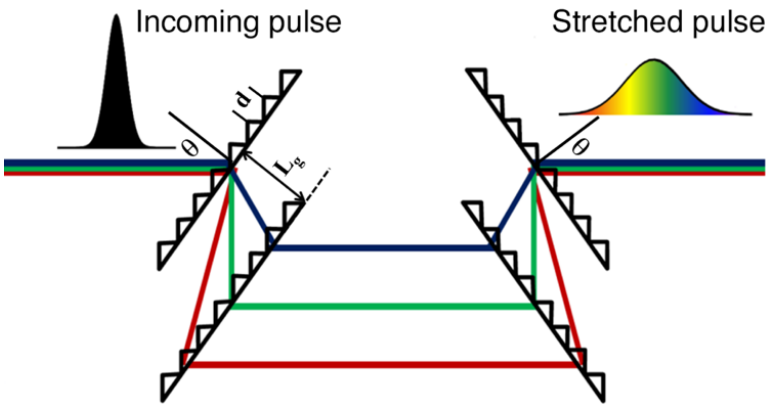

Figure 2.12. Schematic representation of the stretcher used in the experiment. The stretcher is made by two transmission grating pairs. The total amount of negative dispersion introduced by the stretcher is proportional to the distance L_g between the gratings constituting a pair.

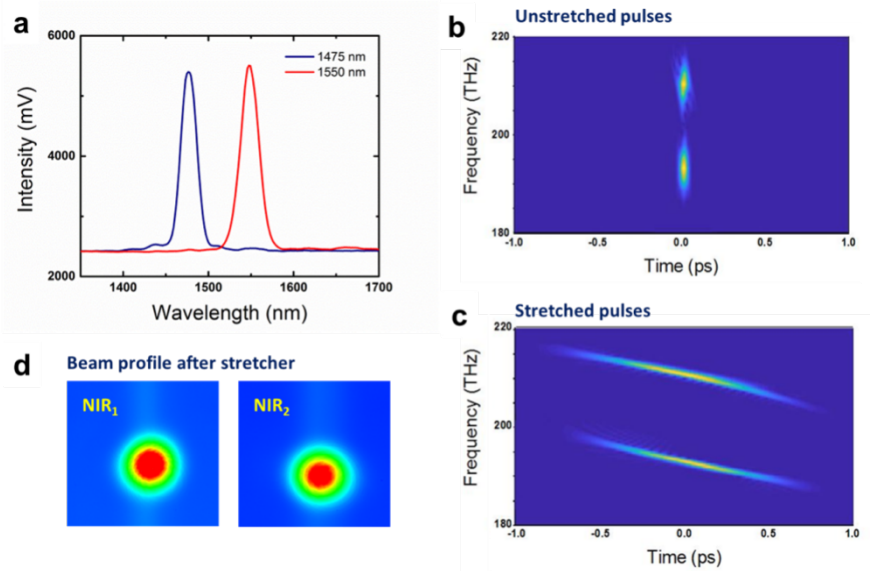

Figure 2.13. (a) Spectra intensity of the two NIR beams with central wavelength at 1475 and 1550 nm and ~ 30 nm bandwidth as the pump and signal in the DFG process. **(b-c)** Wigner map as a function of frequency and time for the two NIR beams before **(b)** and after **(c)** the transmission grating stretcher. **(c)** depicts the two stretched pulses with roughly the same GDD (the slope of the frequency-time trace). **(d)** Beam profile after the stretcher measured with CCD camera for NIR light.

The duration of the stretched NIR pulses is in the range of picoseconds, which is much longer than the incoming pulses ($\tau_{out} \gg \tau_{in}$). Expression (2.16) can be simplified by

$$\tau_{out} \approx GDD/\tau_{in} \tag{2.18}$$

The duration of the output pulses τ_{out} will be linearly proportional to the separation distance L_g. In the experiment, high-efficiency transmission gratings (almost 95% diffraction

efficiency between 1.4 μm and 1.55 μm) with 966.2 lines/mm and incident angle θ of 48.3° have been used.

In our setup, two identical pulse stretchers were used to introduce equivalent amounts of negative linear dispersion to the signal beams from the OPAs at 1475 nm and 1550 nm wavelengths. Figure 2.13 shows the Wigner map retrieved from SHG-FROG measurements, without (b) and with (c) the stretchers. Without stretching, both the NIR pulses are near transform-limited with 100 fs duration. By fine-tuning L_g of both stretchers, the time-frequency traces of the two NIR pulses can be adjusted parallel to each other, shown in Figure 2.13(c). After the stretchers, the pulses are stretched to 600 fs with $GDD \sim -80000$ fs^2.

The far-field beam profile of the stretched beams was monitored using CCD camera. In Figure 2.13(d), the spot sizes of both beams were adjusted to be 2 mm (FWHM) using two sets of telescopes with perfect Gaussian shape. No hot spot is recognized due to the filtering effect in the stretcher to the co-propagating visible light. Further stretching of the pulses can be easily achieved by enlarging L_g. The investigation of the relation between the generated MIR-THz bandwidth and the NIR pulse length will be discussed in the following sections.

2.2.3 Results: Intense narrowband THz pulse generation

The schematic drawing of the optical setup can be found in Figure 2.14. A commercial Ti:sapphire amplifier, delivering 800-nm wavelength pulses with 7 mJ and ~100 fs duration at 1 kHz repetition rate was used to feed the whole system. Two homemade OPAs were seeded by the same supercontinuum to generate CEP-stable THz radiation in the DFG process [102]. Each OPA generated signal output pulses of ~800 μJ energy and ~120 fs duration, which were tuned between 1.35 and 1.5 μm. The near-IR beams were collimated to diameters of about 2 mm, keeping the incident fluence below the DSTMS crystal's damage threshold of 150 GW/cm^2. Efficient DFG in the nonlinear DSTMS crystal requires type-0 phase matching, facilitated by polarizing both near-IR beams along to the crystal a-axis and choosing a quasi-collinear geometry with <0.1° angle [101]. The generated THz fields were transmitted through three 20-THz low-pass filters to block the residual near-infrared beams and characterized by either Fourier-transform interferometer (FTIR) or by electro-optic sampling (EOS) in a 100-μm thick GaSe crystal. For the latter, ~50 fs gating pulses were obtained by spectral broadening and compression of a low-energy replica of the fundamental 800-nm beam, using a thin sapphire crystal and a prism compressor (SF-10).

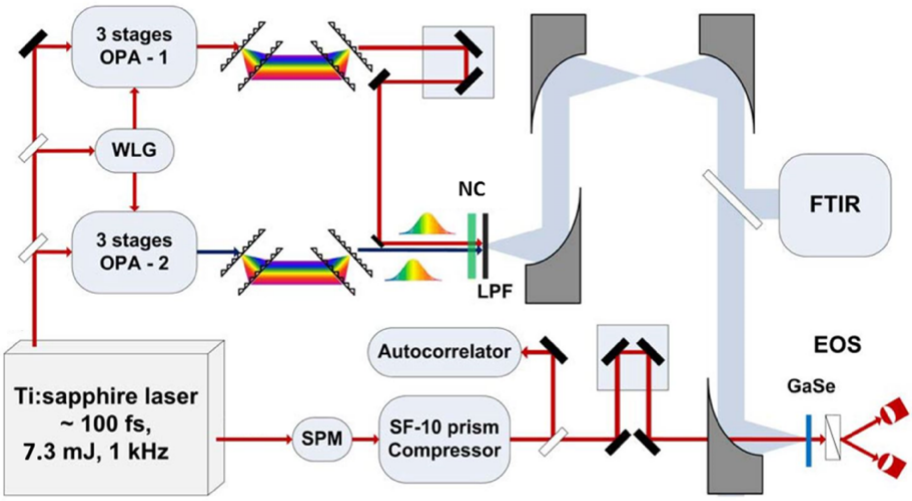

Figure 2.14. Narrowband THz setup. A Ti:sapphire regenerative amplifier serves to pump two separate three-stage optical parametric amplifiers seeded by the same white-light continuum. The signal output pulses, tuned between 1.35 and 1.5 μm wavelength, are linearly chirped by sets of high-efficiency transmission gratings and used for the DFG process in the DSTMS nonlinear crystal. The generated THz electric fields are characterized via FTIR or electro-optic sampling in a GaSe crystal, the latter using ~50 fs gate pulses.

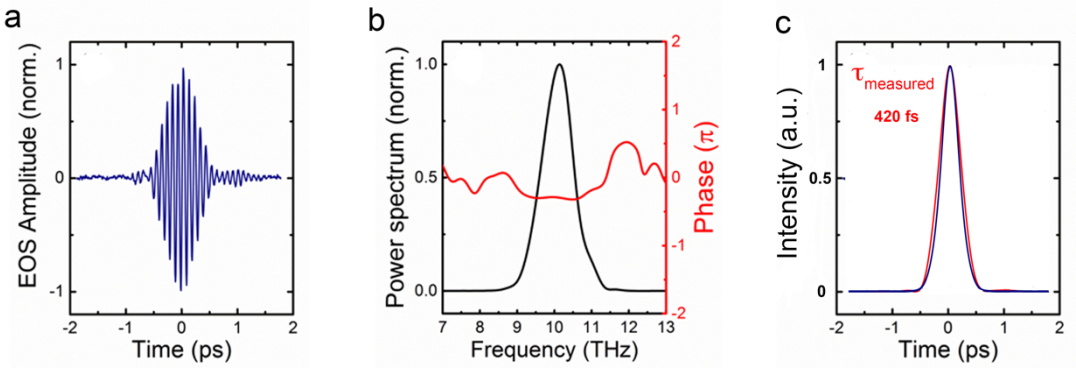

Figure 2.15. (a) The THz electric field generated by DFG in a 480 μm thick DSTMS crystal as detected via electro-optic sampling in a GaSe crystal of 100 μm thickness. **(b)** Corresponding power spectrum (black) and spectral phase (red). **(c)** Retrieved pulse duration from the EOS measurement (red) and the constructed transform limit pulse from the measurement (blue).

Figure 2.15(a) shows the electro-optic sampling measurement of a CEP-stable THz electric field generated in a 480 μm thick DSTMS crystal by mixing two OPA signal wavelengths tuned to 1475 and 1550 nm, respectively. The corresponding power spectrum with a flat spectra phase is plotted in Figure 2.15(b), which is centered at 10 THz with <1-THz bandwidth. The center frequency is in agreement with the difference of the two near-IR frequencies of 209.6 and 199.8 THz.

The retrieved THz pulse and the corresponding transform-limited pulse according to the EOS measurement are shown in Figure 2.15(c). The THz pulse duration is calculated to be ~420 fs (FWHM), which is close to the transform-limit shown in blue. The dispersion is reduced due to the narrow spectrum of the THz pulses, which warranties the generation of near transform-limited pulses.

The pulse energy of the electric field transient shown above, measured by a commercial thermopile detector (Ophir Optronics, Model 3A-P-THz), was more than 5 μJ. Two parabolic mirrors were used to first collimate and then focus the THz beam onto the electro-optic detection crystal. A spot size of 180 μm was determined from knife-edge measurements, resulting in a peak electric field of > 6 MV/cm ($E_{peak} = \sqrt{2Z_0 W_{pulse}/A_{pulse}\,\tau_{pulse}}$ with Z_0 the vacuum impedance, W_{pulse}, A_{pulse} and t_{pulse} the energy, area, and duration of the THz pulse). The corresponding peak intensity was 46.8 GW/cm^2.

2.3.4 Results: Frequency tunability and bandwidth control

These THz pulses can be frequency-tuned by changing the delay between the two chirped near-IR pulses. To characterize the generated narrowband pulses in broad spectrum range, we used Fourier-transform infrared spectroscopy (FTIR) (see appendix A). In our experiment, a pyroelectric detector is applied in the FTIR measurement for its high sensitivity and wide detecting range. A compact FTIR is placed in the vacuum chamber for THz pump spectrum characterization. Figure 2.16 shows how different delays change the generated frequency in the nonlinear crystal. The experimental data on the right confirms the tunability between 9.5 and 11 THz, which is limited by the bandwidth of the NIR pulses.

The central frequency of the THz fields could be further tuned by adjusting the wavelengths of the two mixing near-IR beams. The type-0 phase-matching condition in DSTMS is directly determined by the frequency-dependent refractive index along the crystallographic *a*-axis [101]. Due to the vibrational absorption, the phase-matching conditions for a desired THz output frequency is not only sensitive to the difference in the near-infrared photon energies, but also the frequencies themselves.

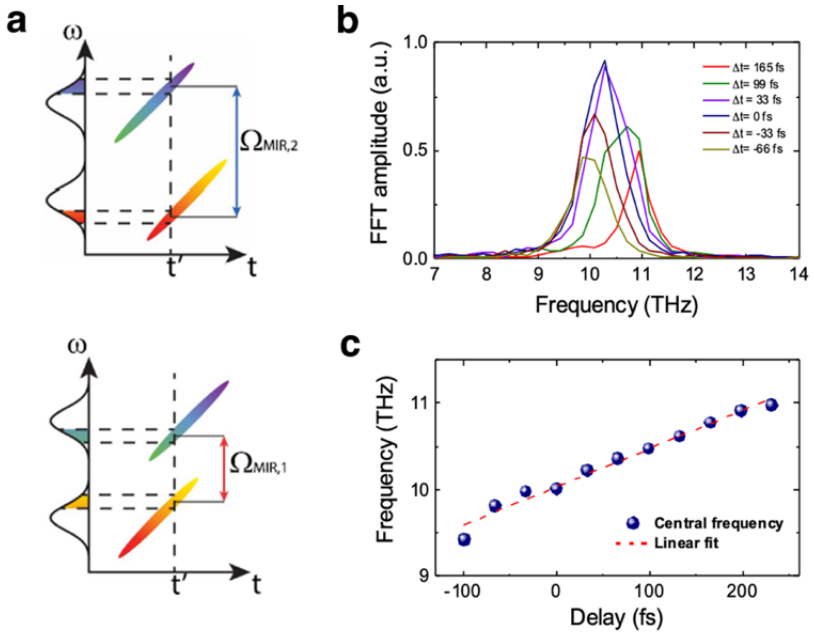

Figure 2.16. (a) Schematic explanation of the relationship between the delay of the two stretched NIR beams and the central frequency of generated MIR-THz pulses [97]. **(b)** Normalized Fourier transform amplitude of the generated THz transient around 10 THz at different time delays of the two interacting NIR beams. **(c)** The central frequency of the generated THz transient as a function of time delay.

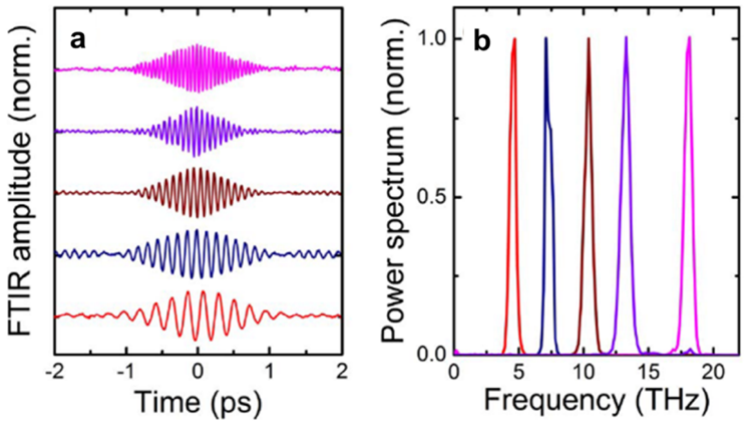

Figure 2.17. (a) Normalized FTIR interferograms and **(b)** the corresponding Fourier spectrum of the THz fields, tuned by changing the difference frequency between the two linearly-chirped near-IR pulses.

Figure 2.17(a) shows the FTIR traces of THz transients tuned across a broad spectral range below 20 THz. In Fig. 2.17(b), the corresponding Fourier spectrum confirms the tunability between 4 and 18 THz. To achieve maximum pulse energy at a desired THz frequency, the center wavelengths of the two NIR pulses were tuned simultaneously. For example, efficient 4.5 THz pulse generation was realized by mixing the two signals at 1395

and 1425 nm wavelength. The amount of chirp on the two near-IR pulses was kept constant throughout the measurements to control the spectral bandwidth below 1 THz. The pulse energy for these different frequencies varies between 3 and 7 µJ, due to the wavelength-dependent THz absorption in DSTMS.

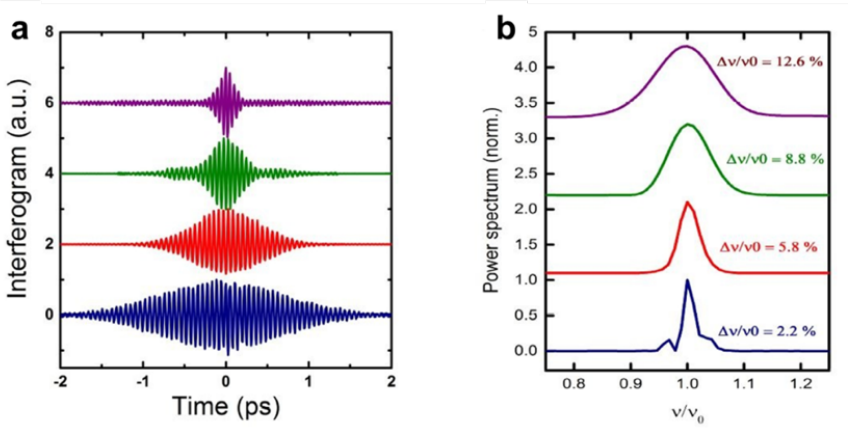

Figure 2.18. (a) Interferograms for the THz fields generated by using near-IR pulses with different duration. **(b)** The corresponding relative bandwidth $\Delta\nu/\nu_0$ (FWHM) of the THz fields shown in (a).

The control of the spectrum bandwidth was also investigated by sending NIR beams with different pulse duration. In Figure 2.18, the FTIR measurements for the generated THz transients generated with different NIR pulse duration together with the relative bandwidth $\Delta\nu/\nu_0$ are reported. Stretched NIR pulses with 200 fs to 1.5 ps duration were used in the DFG process and relative spectrum bandwidth down to 2% can be achieved. The relative bandwidth $\Delta\nu/\nu_0$ could be further minimized by sending even longer NIR pulses. The conversion efficiency of the THz generation could be compensated at the same level by keeping the peak intensity the same on the DSTMS crystal.

2.3.5 Results: Carrier envelop phase (CEP) stability

The carrier-envelope phase (CEP) stability is a big asset in vibrational control of complex materials as it enables to explore the coherent perturbation of electronic, magnetic, and vibrational modes on the sub-cycle phonon timescale [104]. The CEP of a laser pulse is the relative phase between the electric field profile and its intensity envelope. A schematic explanation of carrier envelop phase offset is depicted in Figure 2.19(a). Due to the dispersion of the ultrashort pulses, the group velocity is not equal to phase velocity, which leads to the carrier envelop phase offset. Usually, the ultrafast pulses delivered from laser source is not CEP stable, which needs additional device with a close loop to stabilize.

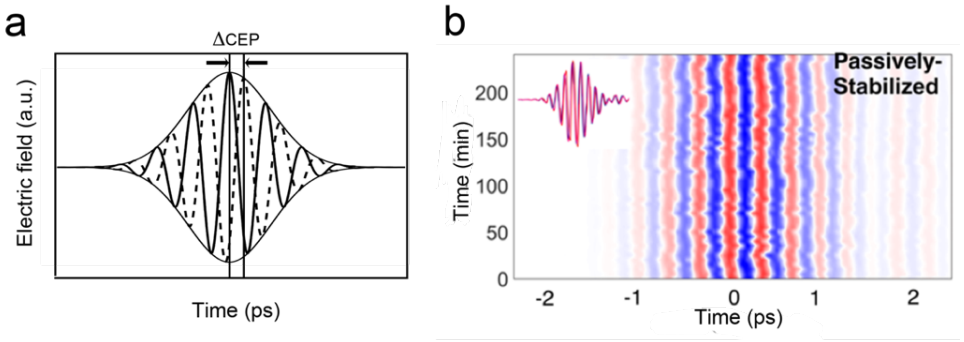

Figure 2.19. (a) Example of carrier-envelope phase shift. **(b)** CEP stability characterization of narrowband pulses. Due to the passive stabilization in the difference frequency generation process, the recorded electro-optical sampling over 240 minutes (4 hours) with negligible drift proves the generated pulses to be CEP stable. Inset: EOS traces measured with of 1-hour interval.

In phase-sensitive or time-resolved gating measurements like EO sampling, the examined pulses need to have a reproducible electric field profile, which means CEP stability. CEP stable THz pulses can be generated starting from non-CEP stable sources by using the phase relations between the pulses involved in nonlinear optical processes. Frequency mixing between two pulses with CEP of φ_1 and φ_2 generates a pulse with absolute phase given by [103]

$$\varphi_{DF} = \varphi_1 - \varphi_2 - \pi/2 \tag{2.19}$$

In the narrowband approach, the two interacting near-IR pulses are the signals from two parallel OPAs, which are seeded by the same super-continuum. Their carrier-envelope phases are mutually phase-locked, which can be written in the form of $\varphi_1 = \varphi_2 + \Delta\varphi$, in which $\Delta\varphi$ is constant. Then the generated THz pulses will process a phase of $\Delta\varphi - \pi/2$, which is passively stabilized.

However, due to the environment changes such as humidity, temperature or air fluctuation, the generated THz pulses always present a long-term drift in the CEP. If this drift cannot be ignored, fine CEP control on one of the interacting near-infrared beams will be needed to actively stabilize the carrier-envelope phase [105].

The CEP stability of the generated THz pulses was characterized by sampling the electric fields over 4 hours. In Figure 2.19(b), the phase drift of the electric field of the generated pulses is relatively small in this time interval. A quantitative analysis yields an accumulated phase shift only about 0.14 pi (or ~440 mrad) and residual fluctuations of 0.03pi (or ~95 mrad), which is more stable compared with the previous work [105].

Summary

First, the common techniques of the generation of intense THz pulses have been reviewed. Narrowband THz pulses can be produced by Free-electron lasers throughout the MIR-THz range, however, the carrier-envelope-phase stability, flexible tunability and unlimited access are unfulfillable. Alternatively, intense pulses below 5 THz or above 15 THz can be achieved via optical rectification and difference frequency generation in nonlinear optical crystals, respectively. So far, the vibrational phase control of materials in the frequency gap between 5 and 15 THz is still challenging with the conventional approaches.

To overcome the limitations, I introduced a new approach of CEP-stable THz generation based on chirped-pulse difference frequency generation in nonlinear organic crystals DSTMS, which bridging the “Terahertz-gap”. THz pulses with energy up to 7 μJ can be achieved by pumping the optical parametric source with 7-mJ 800-nm pulses delivered from a Ti:sapphire system. The corresponding conversion efficiency from the fundamental light wave to the THz wave is around 0.1 %. The tunability can be extended to nearly 100 THz with the aid of GaSe and $AgGaS_2$ crystals, occupying the spectrum range of the FELs THz source.

This novel narrowband THz source has been exploited for THz spectroscopy investigating nonequilibrium physical properties of materials. This includes studying high temperature light-induced superconductivity, which has been an elusive goal of physicists for many years. Before these results are presented in Chapter 4, the background of superconductivity will be reviewed in the next chapter.

Chapter 3

3. High-temperature superconductivity in copper oxides

Superconductivity, was first discovered by Heike Kamerlingh Onnes in 1911 while investigating mercury at cryogenic temperature. When a material becomes superconducting below its critical temperature, it exhibits two peculiar behaviors. First, the electrical resistance drops to zero, indicating lossless electronic transport. Second, if the superconductor is placed in a weak magnetic field, the flux is expelled thanks to the Meissner-Ochsenfeld effect. Over the past decades, it has been a central topic to establish the theoretical explanation of the microscopic mechanism of superconductivity. In the meantime, many experimental investigations have been undertaken to increase the critical temperature of the superconducting state by either fabricating unconventional materials or by investigating existing compounds in extreme conditions, for example using high pressure techniques.

Before the discovery of cuprate superconductors, the highest achieved superconducting transition temperature was below 40 K. In 1983, Bednorz and Müller started to investigate the so-called oxide superconductors. The idea was to create conducting oxides containing Jahn-Teller ions, which could be characterized by strong interaction of the electrons with local distortions of the crystal lattice. In 1986, they observed a dramatic drop of the resistivity in samples with varying ratios of La^{3+} and Ba^{2+} at temperatures below 35 K [106]. Within a

short period, many scientists confirmed superconductivity in these new types of oxides with the form $La_{2-x}M_xCuO_4$, where M = Ba, Sr, Ca [107]. Superconductivity was then found in the $YBa_2Cu_3O_{6+x}$ compounds above 90 K, which is higher than the boiling temperature of liquid nitrogen [54]. Even higher critical temperatures were found in other cuprates like $Bi_2Sr_2CaCu_2O_{8+x}$ [108] and $Tl_2Ba_2Cu_3O_{8+x}$ [110]. So far, the record is held by the Hg-based copper oxide with T*c* ~ 138 K at ambient pressure [111], which can be increased up to 164 K under hydrostatic pressure [112].

In this chapter, I will first give a phenomenological introduction on the basic aspects of superconductivity. Then I will start introducing superconductivity in the cuprate superconductors, describing their crystal structure, their phase diagram, and the peculiar Josephson physics.

3.1 Conventional superconductors

After H. K. Onnes discovered superconductivity in mercury, superconducting behavior was also recognized in other elemental (e.g. lead) and alloy superconductors (e.g. Nb-Ti). Most of these compounds are categorized as conventional superconductors, in which the mechanism of superconductivity can be explained by BCS theory and its related extensions. As shown in Figure 3.1(a), through the superconducting phase transition, superconductors manifest dramatic drop down to zero in the electrical resistance, differing from the normal metal with a finite value. In the meantime, if the superconductor is placed in a weak magnetic field, the interior magnetic flux will be expelled, depicted in Figure 3.1(b). The applied magnetic field penetrate into the superconductors and the decays exponentially as $B(x) = B(0)\exp(-x/\lambda_L)$, where $B(0)$ and λ_L denote the field strength at the surface, and the London penetration depth.

Superconductors can be classified into two categories based on their magnetic properties. In type-I superconductors, a relatively weak applied magnetic field $H < H_{c1}$ (H_{c1} is the critical magnetic field) will be completely expelled when the material is cooled below T_c. However, in type-II superconductors, two critical magnetic fields H_{c1} and H_{c2} ($H_{c1} < H_{c2}$) can be identified. If the applied magnetic field $H < H_{c1}$, the material still behaves like a perfect diamagnet. When $H_{c1} < H < H_{c2}$, there undergoes a mixed state of superconducting and normal state regions, which is also referred to as the vortex state. The superconducting material will be completely transformed into the normal state only when the applied magnetic

field exceeds H_{c2}. Conventional superconductors can be either type-I or type-II. Most of the elemental superconductors are type-I, while the alloy superconductors are usually type-II.

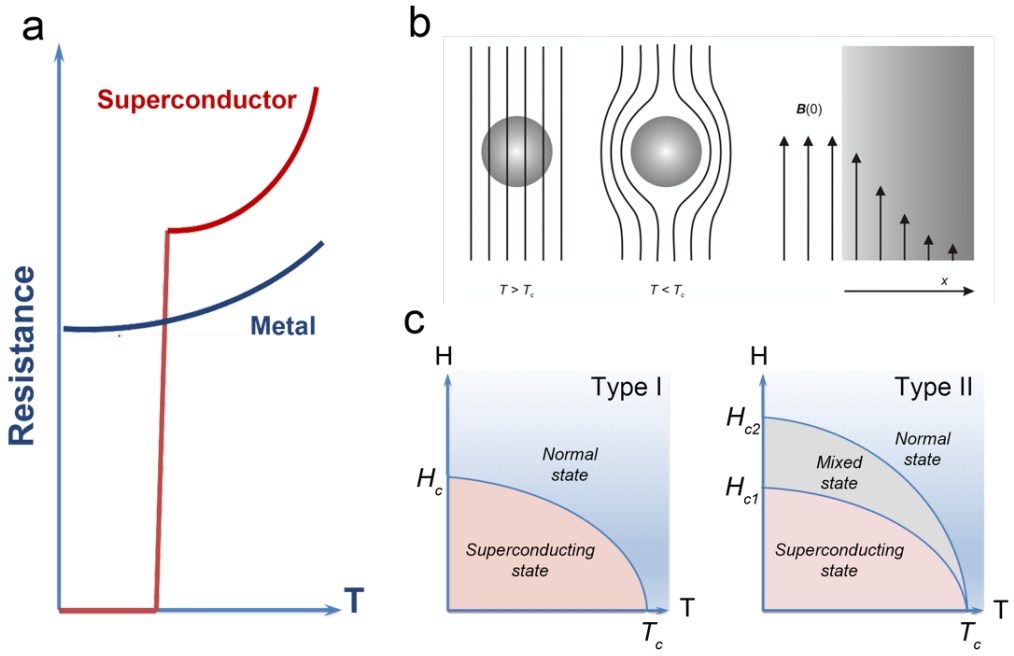

Figure 3.1. (a) The resistance as a function of temperature for a superconductor (red) and normal metal (blue). **(b)** Left: depiction of the expulsion of an external magnetic field B by a spherical superconductor (Meissner effect). Right: A magnetic field is applied perpendicular to the surface normal of a superconductor. The magnetic field decays exponentially inside the material. B(0) defines the magnetic field at the surface. From Ref. [113]. **(c)** Schematic phase diagram as a function of temperature and applied magnetic field for Type I (left) and Type II (right) superconductors.

The pairing theory proposed by Bardeen, Cooper, and Schrieffer in 1957 describes the microscopic mechanism of superconductivity in conventional superconductors, which based on the electron-phonon coupling [124]. A schematic explanation of how BCS superconductivity appears is displayed in Figure 3.2. In metals, normal electrons carry charge. The moving electrons experience resistance due to collisions and scattering from lattice vibrations as they travel. When the critical temperature is approached, the lattice vibrations are slowed down and the material is closer to a perfect crystal. A moving electron attracts nearby ions and creates a positively charged wake, which will attract other nearby electrons with opposite momentum and spin to form a Cooper pair. When more electrons are paired, they behave in the same fashion and condense, then the material turns into the superconducting state. This is analogous to boson condensation in the superfluid state. Despite the strong direct Coulomb repulsions, the weak attractions between electrons induced by the coupling to the lattice vibrations can bind the electrons into pairs at energy lower than the typical phonon energy [117].

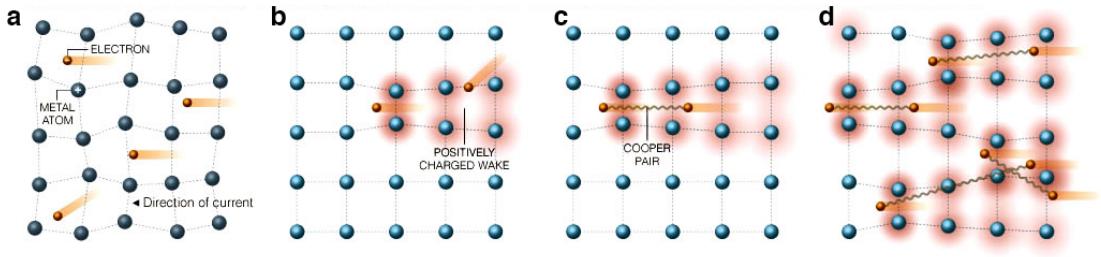

Figure 3.2. Conventional superconductivity and phonon-mediated electron-electron attraction (Cooper pair). **(a)** Electrical resistance is caused by collisions and scattering as the particles move through the vibrating lattice. **(b)** At the critical temperature, the lattice vibration slows down and a moving electron attracts nearby atoms, creating positive attraction to another nearby electron. **(c)** A weak bond pairs the two electrons to form a Cooper pair, which encounters less resistance than two separated electrons. **(d)** As more Cooper pairs form superconductivity is realized and transport without dissipation sets in. Adapted from Ref. [116].

The collective behavior of the electrons in the material is depicted in Figure 3.3(a). Above T_c, the conduction band of is fully occupied, with the normal electrons as the charge carriers. When the system is cooled down below T_c, due to the Cooper pair condensation, an energy gap emerges at the Fermi surface with a gap size much smaller than the Fermi energy. In conventional superconductors, the gap symmetry is isotropic in the momentum space, as depicted in Figure 3.2(b). In general, the superconducting gap is strongly related to temperature (see Figure 3.2(c)), with a gap size in the range of several meV, which is a perfect match with the THz light waves in terms of energy scale. So far, THz spectroscopy has proven to play an important role in probing the superconducting order parameters [4][6][7][11][29].

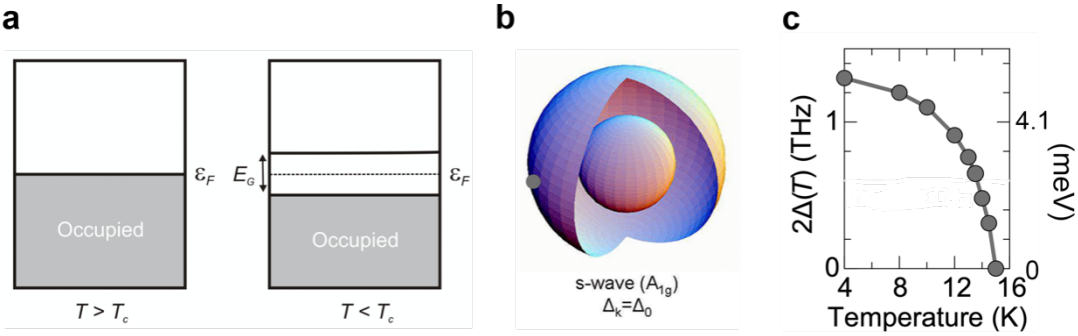

Figure 3.3. (a) Electronic state for a conventional superconductor above (left) and below (right) the transition temperature. The conduction band is occupied up to the Fermi level ε_F above T_c, while an energy gap opens around the Fermi surface below T_c. From Ref. [113]. **(b)** Gap function of s-wave symmetry, which is isotropic in the momentum space. From Ref. [113]. **(c)** Temperature dependence of the superconducting gap energy of a typical conventional superconductor NbN.

3.2 High-T_C Cuprate Superconductors

Over the past few decades, new classes of superconductors have been discovered which showing distinct features compared with the traditional superconductors. The pairing mechanism of the superconductivity in these so-called "unconventional superconductors" is different from the electron-phonon coupling, which could successfully explain the microscopic mechanism of conventional superconductivity [123]. By an "un-conventional" superconductor, the pairing symmetry is not s-wave. Typically, the superconducting gap function in unconventional superconductors is not uniform in momentum space, i.e. YBCO, which exhibits a d-wave symmetry.

The discovery of superconductivity in cuprates opened a new era of high-T_c superconductivity [107]. A series of compounds based on Cerium and Uranium were found to be superconducting at relatively low temperatures (below 20 K), which are categorized as heavy-fermions (see Figure 3.4). Up to date, the pairing symmetry has not been clearly identified in most of the heavy-fermions. Later on, iron-based pnictide superconductors have been discovered, with the highest T_C above 50 K (see Figure 3.4). It is believed that the order parameter has $s_{\pm}$ symmetry in pnictide superconductors [128]. As high-T_C superconductors, cuprates have been attracting massive attention and paved a promising path towards the discovery of "room-temperature superconductors" [6][11]. The superconducting order parameter in cuprates has been revealed to have *d*-wave symmetry with nodes on the Fermi surface [117][132]. In terms of transition temperature, copper-based and iron-based superconductors exhibit much higher T_C compared with the McMillan limit, which couldn't be explained by the BCS model.

In this thesis, I will focus on the high-T_C cuprate superconductors. It is still a big challenge to establish an effective theoretical model to explain the origin of the d-wave superconductivity. Different possible mechanisms are under active debate. Philip Anderson proposed that cuprates would exhibit a novel phase where the spins formed a liquid of singlets, the so-called RVB (resonating valence bond) state [133]. The antiferromagnetic lattice in cuprates could be melt into the spin-liquid phase and the resulting system becomes superconducting upon further hole-doping. On the other hand, the strong exchange interaction in cuprates has been also speculated to act as the attractive force of electron pairing, which is known as the spin fluctuation-based approach [134]. Furthermore, it has also been proposed that superconductivity is mediated by quantum critical fluctuations, which originates from the quantum critical point hidden under the superconducting dome. In following sections, the

generic properties of high-T_C cuprate superconductors, especially $YBa_2Cu_3O_{6+x}$ compounds, will be discussed in details.

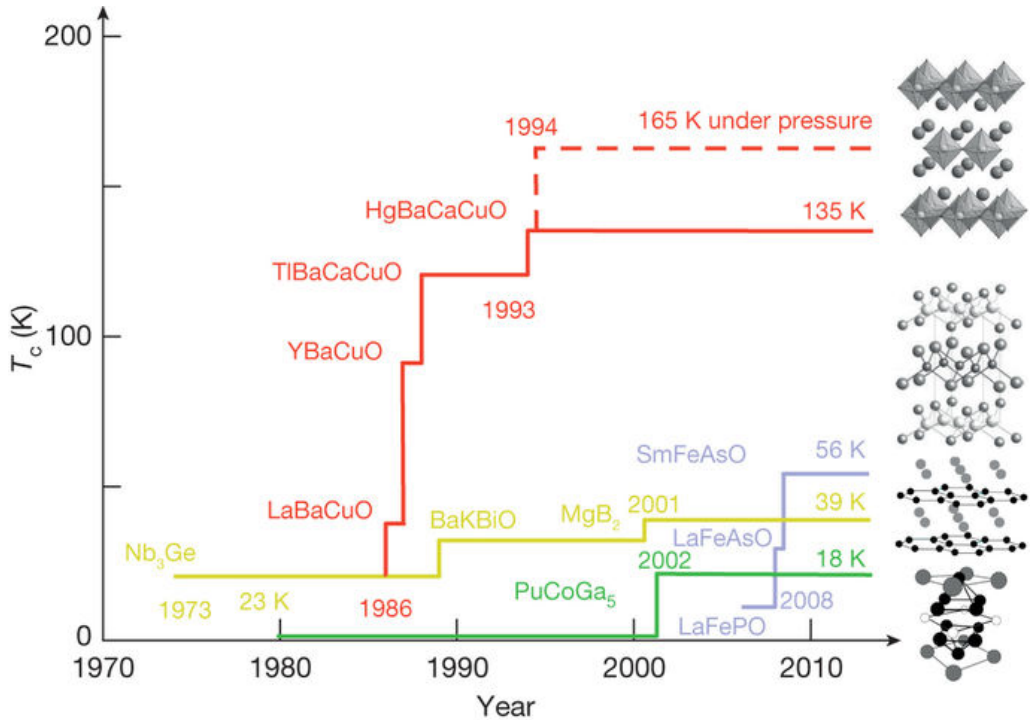

Figure 3.4. Superconducting transition temperatures versus year of discovery for various classes of superconductors. The images on the right are the crystal structures of representative materials. The timelines for conventional superconductors, heavy-fermions, cuprates, and iron-based pnictides are plotted in gold, green, red and light grey, respectively. Adapted from Ref. [117].

3.2.1 Crystal structure

All cuprates have layered structure along the crystal *c* axis with stacked copper-oxygen layers and charge-reservoir blocks (Figure 3.5(a)). In order to achieve higher T_C, cuprate compounds with a larger number of layers (typically between 1 and 3) have been synthesized. The composition of these compounds and the corresponding highest transition temperatures for each category are given in Table 3.1. It is convenient to categorize the hole-doped superconducting cuprates into several classes: the $La_{2-x}M_xCuO_4$ (LMCO) type, the $YBa_2Cu_3O_{6+x}$ (YBCO) type, and Bi-, Tl-l, Hg-type compounds as $A_mM_2Ca_{n-1}C_unO_x$, where A = Bi, Tl, Hg and M = Sr, Ba. So far, the highest T_C = 135 K (164 K under 30 GPa) has been achieved in the Hg-1223 compound.

Table 3.1. Selected representative classes of cuprate superconductors, reproduced from [144]. [a]The sequential numbers represent the composition ratio of the cations.

Superconducting compounds	T_c^{max}
LMCO-type compounds	
$La_{2-x}M_xCuO_4$ (LMCO) M = Ba, Sr, Ca	39
La_2CuO_{4+y}	45
$Ca_{2-x}Na_xCuO_2Cl_2$	26
YBCO-type compounds	
$RBa_2Cu_3O_{6+x}$ (x>0.4) (R-123) R = Y, La, Ca, Pr, Nd, Sm, …	93
$YBa_2Cu_4O_8$ (Y-124)	80
$YBa_2Cu_{3.5}O_{8-y}$ (Y-247)	87
Bi-, Tl-, Hg-type compounds	
$Bi_2Sr_2Ca_{n-1}Cu_nO_{2n+4+\square}$ Bi-22(n-1)n[a] (n = 1-3)	
$Bi_2Sr_2Ca_2Cu_3O_{10+\square}$	110
$Tl_mBa_2Ca_{n-1}Cu_nO_{2n+m+2+\square}$ Tl-m2(n-1)n[a] (m = 1,2; n = 1-4)	
$Tl_2Ba_2CaCu_nO_{6+\square}$	93
$Tl_1Ba_2Ca_2Cu_3O_{9+\square}$	133
$Tl_2Ba_2Ca_2Cu_3O_{10+\square}$	125
$HgBa_2Ca_2Cu_nO_{2n+2+\square}$ Hg-12(n-1)n[a] (n = 1-5)	
$HgBa_2CuO_{4+\square}$	98
$HgBa_2Ca_2Cu_3O_{8+\square}$	135

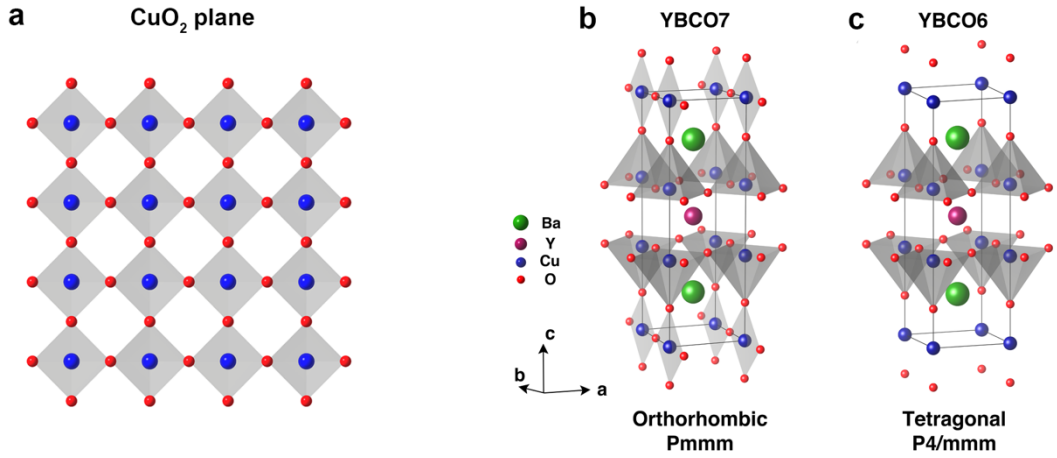

Figure 3.5. (a) Copper-oxygen plane in cuprates. **(b)** Orthorhombic structure of $YBCO_7$ (superconductor), which has *Pmmm* symmetry. **(c)** Tetragonal structure of $YBCO_6$ (insulator), which has *P4/mmm* symmetry. The octahedrons are highlighted in grey.

$YBa_2Cu_3O_{6+x}$ compounds have a typical layered perovskite-like structure with two CuO_2 planes separated by an oxygen-free layer of Y ions, which are coupled by the buffer layers Ba-O-Cu-O-Ba-O. The parent $YBCO_{6+x}$ compounds can be synthesized with two structures. Figure 3.5(b) shows the primitive unit cells of $YBCO_7$ and $YBCO_6$, the remarkable difference

in the crystal structure is the existence of Cu-O chain in $YBCO_7$. By changing the hole-doping concentration of oxygen ions along the *b*-axis, the crystal structure changes from a high symmetry tetragonal phase (*P4/mmm*) (x = 0) to an orthorhombic phase (*Pmmm*) (x = 1).

3.2.2 Phase diagram of the high-Tc $YBCO_{6+x}$

Figure 3.6 shows the phase diagram of the high-T_C cuprate superconductor $YBCO_{6+x}$. As a function of the doping x and temperature, the ground state of the material can be manipulated into antiferromagnetic insulator (AF), pseudogap (PG) phase, strange metal, normal metal and superconductor (SC). For very low doping levels (x < 0.2) the material behaves as an antiferromagnetic insulator. On the opposite side, at doping levels x > 1.2, the material turns into the normal metal phase, which can be described by Fermi liquid theory. In the range 0.25 < x < 1.4, at sufficiently low temperature the material becomes superconducting. Additionally, one finds two anomalous ranges at intermediate dopings, one is in the range below T^*, which is referred to '*pseudogap*' phase, the other is the strange metal phase, in which the behavior of electrons cannot be treated as Fermi liquid.

Antiferromagnetic (AFM) phase

A distinct feature of compounds in the underdoped regime is the presence of strong antiferromagnetic (AF) spin correlations at the Cu atoms in the parent compound. The underdoped parent $YBCO_6$ is an antiferromagnetic insulator with Néel temperature of 500 K. The formation of the long-range antiferromagnetic order can be elucidated in the following picture. In the Cu-O planes, each copper ion with $3d_{x^2-y^2}$ electronic orbital is surrounded by four oxygen atoms with O-$2p_{x,y}$ orbital. The CuO_2 planes have a half-filled energy band, which is intuitively metallic. Due to the hybridization of the Cu-$3d_{x^2-y^2}$ and O-$2p_{x,y}$ orbitals, the system becomes a charge transfer insulator with an energy gap in the range of ~2 eV. Static magnetic moments on the Cu sites align in a regular pattern with neighboring spins pointing in opposite directions, resulting in the AF phase, as evidenced by neutron scattering experiments [120][121]. To lower the energy, the electrons could virtually hop back and forth between different Cu sites, which results in the so-called "super-exchange" interaction. A strong super-exchange interaction (via oxygen ions) of the order of 1500 K between the copper spins gives rise to 2-dimenssional AF long-range order in $YBCO_{6+x}$ with high Neel temperatures T_N up to ~ 500 K. Compared with the strong in-plane super-exchange effect, the

interlayer coupling $J_{\perp} \sim 10^{-5}J$ is extremely weak, which makes the material a quasi-2D antiferromagnet.

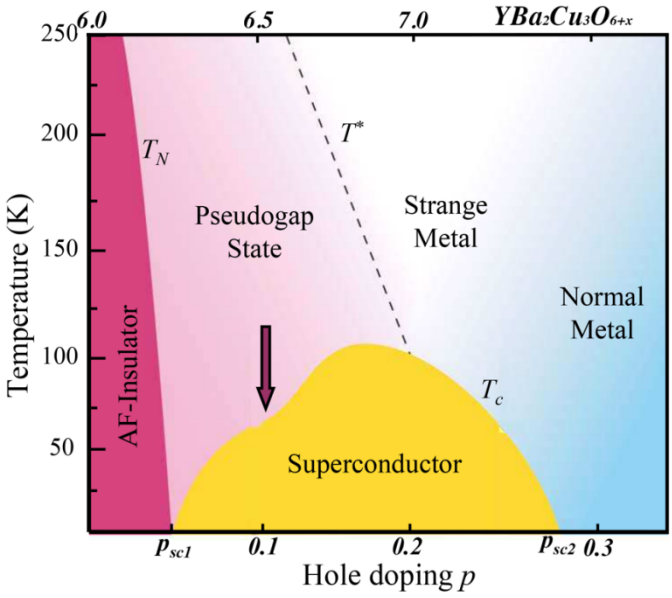

Figure 3.6. Phase diagram of the cuprate superconductors $YBCO_{6+x}$. The arrow indicates the $YBCO_{6.5}$ compound, which will be studied in Chapter 4. Adapted from Ref. [120] .

Normal metal state

Compounds in the heavily overdoped regime with $p > 0.2$ are usually referred to as normal metal. The electrons become delocalized and the system turns into a normal metallic state, which can be described by Landau-Fermi liquid theory [136]. The most prominent feature of the normal metal state is the in-plane resistivity, which varies as $\rho = \rho_0 + aT^2$ at temperatures above T_C which is widely believed to originate from scattering of fermions. Inelastic neutron scattering data indicates a dramatic suppression of magnetic spectral weight near the antiferromagnetic wave vectors, which may be interpreted as a disappearance of the spin-fluctuation pairing glue, explaining why T_C goes down.

Strange metal phase

In the strange metal phase, which in between the pseudogap phase and normal metal phase, the material exhibits unconventional conductivity which can't be explained by Fermi liquid theory. First, the electrical conductivity is usually several orders of magnitude lower than metals. Second, the resistivity scales linearly ($\rho = \rho_0 + aT$) with temperature up the highest temperature that can be measured. This is in contrast to the conventional Fermi liquid, which follows the T^2 behavior and saturates at a certain temperature. Moreover, the Hall resistivity

has a temperature dependence which is different from what would be expected in a quasiparticle picture [146]. Basically, the difference between the strange metal and a conventional metal is the absence of quasiparticles. The linear resistivity behavior might be related to the critical fluctuations at the vicinity of a quantum critical point (QCP), which takes place around optimal doping.

For high-T_C copper oxides, it was speculated that the superconductivity emerges as an instability of the strange metal phase [117]. There are numerous interesting questions which need to be answered, that might provide evidence to understand the origin of the high-T_C superconductivity and explain the related unconventional behaviors.

Superconducting state

The superconducting transition temperature T_C in cuprate superconductors exhibits a parabolic dependence on the concentration of charge carriers. A generic expression of the relationship is given by Presland et al. [136]:

$$T_c(p) = T_{c,max}[1 - \beta(p - p_{opt})^2] \tag{3.1}$$

where $T_{c,max}$ and p_{opt} denote the highest critical temperature and the optimum doping. Typical values $\beta = 82.6$ and $p_{opt} = 0.16$ are valid for a large number of copper oxides.

The in-plane electronic properties change significantly through the thermal transition at T_C, a long-range coherent state appears due to the condensation of the Cooper-pairs. The CuO_2 layers undergo a transition from a metallic phase to a superconducting phase, leading to a quasi-2D superconducting state. In the superconducting state , the Cooper pairs in the CuO_2 layers can tunnel between different layers and the system is then transformed into a 3-dimensional superconductor.

Pseudogap phase (PG)

The pseudogap phase is a distinctive region in the phase diagram where a partial gap in the electronic density of state opens and persists up to temperatures far above T_C. The feature of the gap opening in the pseudogap phase was first recognized by nuclear magnetic resonance (NMR) measurements in underdoped $YBCO_{6+x}$. Anomality was observed in both Knight shift and in spin-lattice relaxation rate measurements of the Cu nuclei in the CuO_2 planes [139]. Later on, the signatures of the pseudogap phase were also found in temperature-dependent resistivity measurements in underdoped $YBCO_{6+x}$ thin films [143]. The enhancement of in-plane anisotropy of the Nernst coefficient at T^* has also been demonstrated [140], which was

regarded as the evidence of the precursor of superconductivity. Recently, the nematicity measured via torque magnetometry in underdoped YBCO samples also revealed the in-plane anisotropy of magnetic susceptibility to increase after exhibiting a distinct kink at T*, indicating that the pseudogap phase is related to a second-order nematic phase transition, differing from a charge-density-wave transition that accompanies translational symmetry breaking [141].

Notably, the symmetry of the pseudogap is very close to the symmetry of the superconducting gap, which suggests the existence of pre-formed Cooper pairs above T_C, that exhibit only with short-range coherence. This speculation has been supported by the infrared optical measurement along the *c*-axis of the underdoped compounds. A clear Josephson plasmon resonance indicates the electron pair tunneling in the high frequency range persists up to T^* in the pseudogap phase [156]. Recent nonequilibrium measurements via vibrational excitation of certain IR-active phonons seems to unleash superconductivity up to the same T^* [11][35][195], hinting to a possible link between the presence of preformed Cooper pairs and light-induced superconductivity [142].

3.2.3 Interlayer Josephson Physics

As aforementioned, the structure of cuprates is anisotropic with conducting CuO_2 layers and charge reservoir layers stacked along the *c*-axis (Figure 3.7(a)). In the normal state, the electrons are confined in the CuO_2 planes making the system is metallic in the *ab*-plane and insulating along the *c* axis. When the system is cooled down below the critical temperature, Cooper pairs start to condense and a phase transition from the metallic phase to the superconducting phase takes place. Along the *c*-axis, Josephson tunneling of Cooper pairs sets in and dominates the electronic response. Figure 3.7(b) elucidates the tunneling of the electrons between different Josephson layers. For normal electrons, the energy barrier is given by the superconducting gap 2Δ. In contrast, Cooper pairs can tunnel through the insulating barrier with the supercurrent taking an arbitrary value between $-I_c$ and I_c.

The superconducting electrons can be described by a wave function in the form of $\psi_i = \sqrt{\rho_i}\exp(i\phi_i)$, where ρ_i denotes the superfluid density and ϕ_i corresponds to the phase of the wave function in different superconducting layers. The current flowing through the barriers can be described by the Josephson equation:

$$I_s = I_c sin\varphi \tag{3.2}$$

The Josephson current is proportional to the sine of the phase difference across the insulating layers. The *AC* Josephson effect can be written as

$$\frac{d\varphi}{dt} = \frac{2eV}{\hbar} \tag{3.3}$$

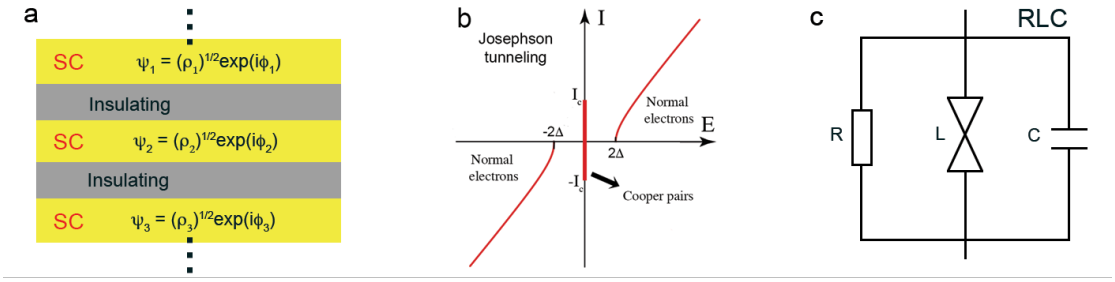

Figure 3.7. (a) Stacked Josephson junctions. Superconducting layers are stacked between insulating buffer layers. ψ_i is the wave function for the superconducting electrons. **(b)** Electron tunneling between Josephson layers. There is a 2Δ energy gap for normal electrons to tunnel through different Josephson layers, however, no energy loss for the Cooper pairs tunneling. **(c)** Equivalent RLC circuit model of the Josephson junctions.

Equation (3.3) describes the temporal evolution of the relative phase φ. $\frac{2e}{\hbar}$ is the Josephson constant, its inverse is regarded as the magnetic flux quantum Φ_0. With a voltage difference V across the insulating layer, the supercurrent will oscillate with amplitude I_c at $\frac{2eV}{\hbar}$ frequency. Josephson's equations are often sufficient to describe the zero voltage behaviors. Nevertheless, they do not model dissipation effects in the finite voltage regime Ref.[113]. The nature of the Josephson junction is analogous to the simple *RLC* circuit shown in Figure 3.7(c). The resistance R describes the dissipation contribution due to the tunneling of the non-superconducting quasi-particle excitation. The inductance L gives the inductive response, while the capacitance C corresponds to the charging effect in the junctions. The total current through the link equals the sum of the contributions from each parallel element according to the differential equation (see Ref.[113])

$$I = I_c \sin\varphi + V/R + C\dot{V} \tag{3.4}$$

Expression (3.4) can be rewritten as the following considering the Josephson equations and a substitution of dimensionless time variable $t \rightarrow \omega_J t$ to form a second-order differential equation in the phase difference

$$\ddot{\varphi} + \beta_c \dot{\varphi} + \sin\varphi = I/I_c \tag{3.5}$$

where $\beta_C = \omega_J RC$ determining the damping. These plane wave solutions behave in the fashion of plasma oscillations and the characteristic frequency is defined as $\omega_J = \sqrt{2eI_c/(\hbar C)} = 1/\sqrt{L_0 C}$, corresponding to the Josephson plasma resonance frequency in the undamped case.

As aforementioned, optical method in the THz frequency regime has been exploited to investigate the Josephson physics to probe the superconducting order parameters. Along the crystal *c*-axis of high-T_C cuprates, the most prominent feature in the superconducting state is the Josephson plasma resonance (JPR), which is accompanied by the change of optical constants (see more details in Chapter 4). A macroscopic view of the dielectric functions of the material across the layers is discussed below. The dielectric function associated to it is expressed by the following formula for compounds with a stack of intrinsic Josephson junctions:

$$\tilde{\varepsilon} = \tilde{\varepsilon}_\infty - \frac{\omega_p(q)^2}{\omega^2 - i\omega\Gamma} \tag{3.6}$$

where $\tilde{\varepsilon}_\infty$ denotes the dielectric function at infinitive frequency ($\tilde{\varepsilon}_\infty$ = 4.5 for cuprates), $\omega_p(q)$ the plasma frequency at momentum q and Γ the scattering rate. Cuprates can also be composed of inequivalent Josephson junctions, i.e. bilayer $YBCO_{6+x}$, the optical behavior can be characterized by summing up the dielectric function of different Josephson junctions in series [182]. For two different junctions, the optical response can be written as

$$\frac{\varepsilon_\infty}{\tilde{\varepsilon}} = \frac{\omega^2 z_1}{\omega^2 - \omega_1^2 + i\omega\Gamma_1} + \frac{\omega^2 z_2}{\omega^2 - \omega_2^2 + i\omega\Gamma_2} \tag{3.7}$$

According to the similarity to the RLC circuit in series, we substitute $z_2\omega_1^2 + z_1\omega_2^2$ with ω_T and the equation (3.7) can be rewritten as

$$\frac{\tilde{\varepsilon}}{\varepsilon_\infty} = \frac{(\omega^2 - \omega_1^2)(\omega^2 - \omega_2^2)}{\omega^2(\omega^2 - \omega_T^2)} \tag{3.8}$$

The response of two inequivalent Josephson junctions in series can be attributed to four plasma modes: two longitudinal plasma modes at frequency ω_1 and ω_2, and another two transverse plasma modes at ω_T and zero frequency. The corresponding simulated optical response is depicted in Figure 3.8(b).

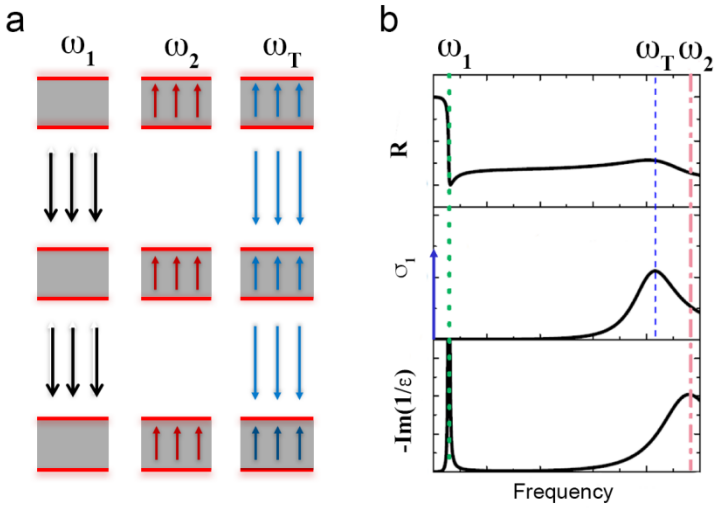

Figure 3.8. (a) Plasma modes in stacked inequivalent junctions. The superconducting planes are highlighted in red and the arrows represent the current flow. The left two are the two longitudinal modes (k || c) at frequencies ω_1 and ω_2. The right contains two transverse modes (k ⊥ c), one with the current flow in the same direction, corresponding to the condensation perpendicular to the planes. The other one with the current flow in the opposite direction represents the finite frequency transverse model, which shares the spectra weight with the zero-frequency mode. **(b)** Simulated optical constants for the plasma modes described in (a). The Josephson plasma edges for the two longitudinal plasma modes are identified in reflectivity (R) and companied with peaks in the loss function (-Im(1/ε)). The transverse plasma modes peak in the real part of optical conductivity (σ_1) at zero frequency and a finite frequency (ω_T).

Summary

After the first discovery in Mercury, more conventional superconductors were found in elemental and alloy compounds. The microscopic mechanism of the superconductivity in these materials can be described by BCS theory or its extensions. The upper limit of superconducting transition temperature in the BCS superconductors was predicted to be lower than 40 K, which is known as the McMillan limit. Remarkably, the discovery unconventional superconductivity (T_C = 92 K) in $YBa_2Cu_3O_{6+x}$ compounds opened a new era of high-T_C superconductivity.

In contrast to conventional BCS superconductors, cuprate superconductors display uncommon properties and superconductivity coexists with several competing orders. They are layered materials with a superlattice of superconducting CuO_2 layers separated by charge reservoir layers. When cooled down below T_C, the superconducting carriers condense in the form of Cooper pairs, which are confined in the quasi-two-dimensional CuO_2 layers. In the superconducting state, Cooper pairs tunnel between different layers, and the electronic and optical properties in the direction perpendicular to the CuO_2 planes are dominated by the Josephson physics.

Chapter 4

4. Controlling superconductivity in $YBa_2Cu_3O_{6.5}$

Layered cuprates exhibit high superconducting transition temperature and a rich phase diagram. Remarkably, optical excitations in cuprate compounds have been shown to induce transient superconducting correlations above the thermodynamic transition temperature, as evidenced by the terahertz frequency optical properties in the nonequilibrium state [11][33]. In underdoped $YBa_2Cu_3O_{6+x}$, this phenomenon has so far been associated with the nonlinear excitation of certain lattice modes and the creation of new crystal structures [10]. However, to date it has not been possible to systematically tune the pump frequency widely in any compound to compare the frequency-dependent photo-susceptibility for this phenomenon.

In this chapter, I will show the dynamics of the transient optical response to the photo-excitation throughout the entire optical spectrum in $YBa_2Cu_3O_{6.5}$ exploiting the newly developed optical device. The connection between the light-induced superconducting-like state and the relevant transient averaged structural changes obtained from a correlated *ab-initio* calculation based on the nonlinear phononics will also be covered. In the end, the mechanism of inducing the superconducting-like state with different excitations will be discussed based on additional experimental observations. Part of the chapter is taken from Ref. [35].

4.1 Equilibrium crystal structure and terahertz *c*-axis optical properties

In ortho-II $YBCO_{6.5}$, due to periodical modulation of the b-axis-oriented Cu-O chains, the primitive unit cell is enlarged twice along the *a*-axis (2a × b × c) as shown in Figure 4.1(a). Each intra-bilayer region consists of two conducting CuO_2 layers separated by Y atoms, and the stack of intra-bilayer units are periodically separated by Ba atoms and CuO_4 ribbons along the *c* direction. The crystal structure projected in the *ac*-plane is shown in Figure 4.1(b) with CuO_2 layers highlighted in grey. The lattice parameters are a = 7.71539 Å, b = 3.90590 Å and c = 12.02474 Å.

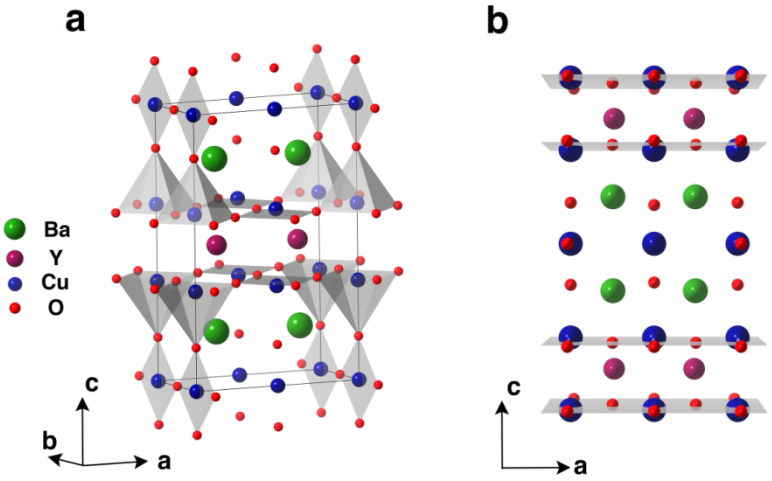

Figure 4.1. (a) Crystallographic unit cell of orthorhombic $YBa_2Cu_3O_{6.5}$ (ortho-II). Bilayers of conducting CuO_2 planes, stacked along the *c*-axis, forming the Josephson junctions. **(b)** Crystal structure projected in the *ac*-plane. The CuO_2 layers highlighted in grey.

In this thesis, $YBa_2Cu_3O_{6.5}$ single crystal with dimensions 1.5 × 1.5 × 0.3 mm^3 grown in Y-stabilized zirconium crucibles was investigated in a narrowband THz pump - THz probe experiment [150]. The hole-doping of the Cu-O planes was adjusted by controlling the oxygen content of the Cu-O chain layer δ by annealing in flowing O_2 and subsequent rapid quenching. A sharp superconducting transition at T_c = 52 K ($\Delta T_C \sim 2$ K) was determined by *dc* magnetization measurements [6].

The equilibrium superconducting transition in high-T_C cuprates shows distinctive features in the terahertz-frequency optical response. In Figure 4.2, the selected optical properties measured in $YBa_2Cu_3O_{6.5}$ above and below T_C are reported. Through the superconducting transition from 100 K (black, $T \gg T_C$) to 10 K (red, $T \ll T_C$), the real part of

the *c*-axis optical conductivity evolves from that of a semiconductor with thermally-activated carriers to a gapped spectrum (see Figure 4.2(a)). Simultaneously, a zero-frequency-peak emerges, which is indicative of dissipation-less DC transport. This peak is not seen directly in $\sigma_1(\omega)$, but is reflected in a $\sim 1/\omega$ divergence in the imaginary conductivity, $\sigma_2(\omega)$ (see Figure 4.2(b)). In the meantime, a sharp edge in the optical reflectivity of the superconducting state develops at the Josephson plasma resonance (JPR) $\omega \simeq \omega_{JPR} \simeq 30$ cm^{-1} [6][11], accompanied by a sharp peak in the energy loss function at the same frequency as shown in Figure 4.2(c-d).

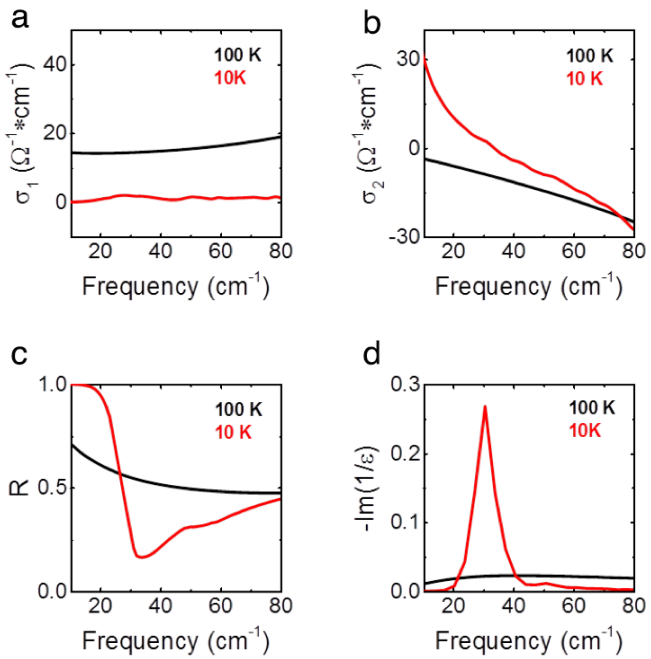

Figure 4.2. *C*-axis THz-frequency optical properties in the equilibrium superconducting ($T < T_C$, red curves) and normal ($T > T_C$, black curves) state in $YBa_2Cu_3O_{6.5}$. **(a-b)** The real and imaginary parts of optical conductivity $\sigma_1(\omega)$, $\sigma_2(\omega)$, **(c)** the reflectivity $R(\omega)$, and **(d)** the energy loss function -Im(1/ε) are reported.

4.2 *C*-axis optical phonons

In $YBCO_{6.5}$, overall 72 vibrational modes are theoretically predicted

$$\Gamma = 11A_g + 3\,B_{1g} + 11B_{2g} + 8B_{3g} + 2A_u + 13B_{1u} + 11B_{2u} + 13B_{3u} \qquad (4.1)$$

For the ortho-II structure, the Raman-active modes are of type A_g, B_{1g}, B_{2g}, and B_{3g}, so there are 33 Raman-active modes. The infrared-active modes are of type A_u, B_{1u}, B_{2u} and B_{3u}, corresponding to 39 infrared-active modes. The theoretical prediction of the eigenfrequencies of these modes are listed in Table C.2 (see Appendix C).

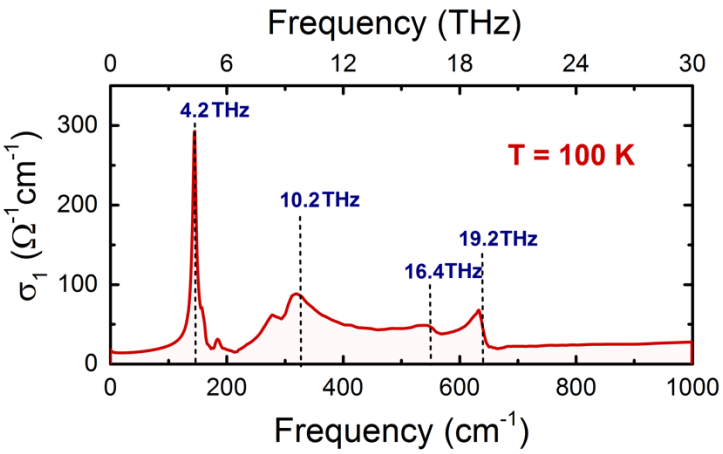

Figure 4.3. Real part of optical conductivity σ_1 along c-axis of $YBCO_{6.5}$ at 100 K (above Tc). Four dominant modes peak at 140 cm^{-1} (4.2 THz), 337 cm^{-1} (10.2 THz), 547 cm^{-1} (16.4 THz) and 640 cm^{-1} (19.2 THz) are noted in blue and indicated with dashed lines.

Here, the discussion is restricted to the infrared-active B_{1u} phonon modes polarized along the *c*-axis. Some of them can be identified in optical conductivity σ_1 displayed in Figure 4.3. The associated atomic motions for modes are summarized as follows [151][152][154][156].

- The 140 cm^{-1} (4.2 THz) mode, often referred to as "Barium mode", can be associated with atomic motions involving Barium atom stretching, CuO_2 plane bulking and apical-O stretching in the oxygen-filled chain.

- The 155 cm^{-1} (4.65 THz) mode, appearing as a shoulder of the 140 cm^{-1} mode, involving the motion of the ions in the Cu-O chains as well as the apical-oxygen ions. This mode is less pronounced when the hole-doping concentration increases.

- The 191 cm^{-1} (5.7 THz) mode, which is ascribed to the Ba-Y stretching motion. This mode is more pronounced when the hole-doping concentration is increased.

- The 279 cm^{-1} (8.4 THz) mode, associated with the atomic motions involving chain-oxygen vibrational and in-plane copper stretching along the c-axis.

- The 337 cm^{-1} (10.2 THz) mode, mainly gains spectral weight from the in-planar Cu-O bending and the displacement of Yttrium ions. It has a strong temperature dependence and shares its spectral weight with the 'transverse plasmon' at ~ 400 cm^{-1}.

- The 547 cm^{-1} (16.4 THz) mode involves pure apical-oxygen stretching motion in the oxygen-filled chain. This mode is referred to as the "YBCO7" mode, as it gets stronger

when increasing the hold-doping.

- The 640 cm^{-1} (19.2 THz) also involves pure apical-oxygen stretching motion, but in the oxygen-vacant chain. This mode is often called "YBCO6" mode, as it becomes more pronounced in the underdoped compounds and loses spectral weight for $x \rightarrow 1$.

Four dominant peaks are found at 140 cm^{-1} (4.2 THz), 337 cm^{-1} (10.2 THz), 547 cm^{-1} (16.4 THz) and 640 cm^{-1} (19.2 THz), whose atomic motions is sketched in Figure 4.4. These atomic motions are calculated based on first principle calculation with narrowband excitation at the eigenfrequency of the modes (see more information in Appendix C).

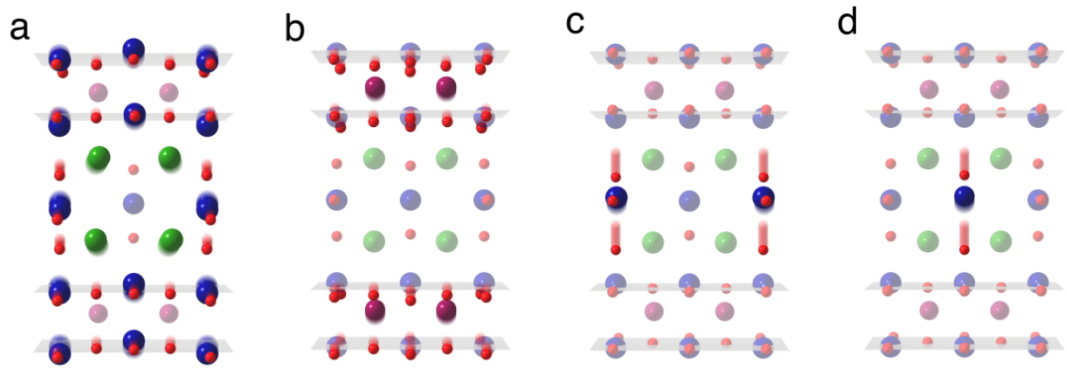

Figure 4.4. Atomic displacement along the normal coordinates of four dominant IR-active optical phonons polarized along c-axis in $YBa_2Cu_3O_{6.5}$ at **(a)** 4.2 THz, **(b)** 10.1 THz, **(c)**16.4 THz, and **(d)** 19.2 THz. The CuO_2 layers are highlighted in grey and transparency is applied to quasi-stationary atoms.

Resonant phonon excitation

The optical setup used to photo-excite $YBa_2Cu_3O_{6.5}$ with tunable narrowband pump pulses and to probe its low-frequency THz response is sketched in Figure B.1 (Appendix B). It was fed by a 1-kHz repetition rate Ti:sapphire regenerative amplifier, delivering 7-mJ, 80-fs pulses at 800 nm wavelength. We used 90% of the pulse energy to generate the excitation pulses. Two parallel home-built optical parametric amplifiers (OPA) were seeded with the same supercontinuum to produce carrier-envelope-phase (CEP) stable THz pump pulses in a subsequent difference frequency generation (DFG) process. The two OPA signal outputs of ~120 fs duration were directly sent to a 1-mm thick GaSe crystal to generate the broadband pump pulses at 19.2 THz with relative bandwidth $\Delta\nu/\nu \sim 20\%$. For the generation of narrowband pulses with relative bandwidth $\Delta\nu/\nu < 10\%$, the two signal outputs were linearly chirped to a pulse duration of ~600 fs before the DFG process in either a 0.5 mm thick DSTMS organic crystal or in the same 1-mm GaSe crystal used for the broadband pulses. The

pulse energies achieved were always at the few-μJ level. The maximum peak electric fields of the focused beams at the sample surface were 2.9 and 2.7 MV/cm for 4.2 and 10 THz, respectively, and about 3.1 MV/cm for both 16.4 and 19.2 THz pulses. They could be attenuated by inserting a pair of free-standing wire grid polarizers.

Excitation pulses with frequencies above the phonon resonances and up to the near-infrared and visible light regime were either generated by difference-frequency mixing the two OPA outputs in an GaSe crystal, or were taken directly as the output of one of the OPAs, as the fundamental 800 nm pulses from the Ti:sapphire amplifier, or as their second harmonic generated via type-I phase matching in a BBO crystal.

Time-resolved terahertz spectroscopy

Single-cycle THz probe pulses with spectral components between 10 and 80 cm^{-1} were generated via optical rectification of 500-μJ pulses at the fundamental 800 nm wavelength in a 0.5 mm thick ZnTe crystal. The THz electric field of the probe pulses reflected from the sample surface was detected via electro-optic sampling in a 500-μm thick optically contacted ZnTe crystal.

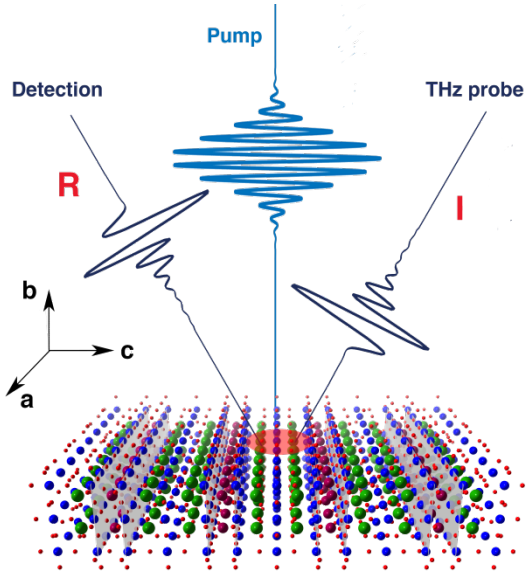

Figure 4.5. THz pump - THz probe geometry in the $YBCO_{6.5}$ experiment. The THz pump pulses, polarized along the *c*-axis, were shone onto the *ac*-plane surface of the $YBCO_{6.5}$ sample. Broadband THz pulses with incident angle at 30 degrees, also polarized along the *c*-axis, were used to probe the pump-induced changes in the $YBCO_{6.5}$ optical response functions. "I" and "R" stand for "incident" and "reflected" pulse, respectively.

Figure 4.5 illustrates the pump-probe geometry in the experiment. *C*-axis polarized MIR-THz pulses with frequency resonating with the target phonon mode were sent to the *ac*-

surface of a $YBa_2Cu_3O_{6.5}$ single crystal. Broadband THz pulses with an incident angle of 30 degrees were used to probe the pump-induced dynamics after the excitation.

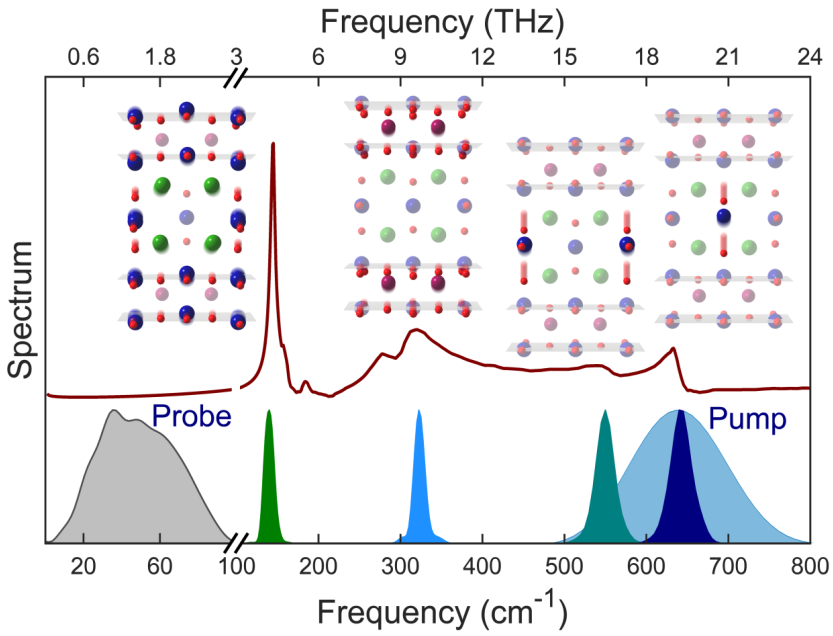

Figure 4.6. Equilibrium *c*-axis optical conductivity, $\sigma_1(\omega)$ (red) of $YBCO_{6.5}$ at 100 K ($T > T_C$, red solid line), along with the frequency spectra of THz probe (grey) and of broadband 19 THz pump pulses (light blue) and different narrowband pump pulses, tuned to be resonant with four different optical phonons at 4.2 THz, 10.1 THz, 16.4 THz, and 19.2 THz. The insets sketch the atomic motions related to each of these modes, with CuO_2 layers highlighted in grey and transparency applied to quasi-stationary atoms [35].

Figure 4.6 depicts the *c*-axis vibrational modes (red curve and insets) together with the spectrum of the pump pulses (lower panel). It is evident that with the newly designed narrowband source, the IR-active modes at 4.2 THz, 10.1 THz, 16.4 THz, and 19.2 THz can be selectively excited.

In the following sections, experiments performed at temperature both above and below T_C with the same broadband ~4-THz-wide pulses used in Ref.[6][11] will be firstly discussed. Afterwards, the transient optical response of $YBCO_{6.5}$ upon narrowband resonant excitation of different IR-active modes will be investigated.

Importantly, in all these experiments the pump pulses were focused onto the sample at a fluence of ~8 mJ/cm^2. Note that in the narrowband experiments, the pulses were four times longer than in the broadband experiments (~600 fs vs. ~150 fs). As these two measurements used the same pump fluence, the peak electric fields were of 3 and 6 MV/cm for narrowband (long pulse) and broadband (short pulse) excitation, respectively.

4.3. Data acquisition and processing

Time-domain THz spectroscopy was used to characterize the transient response of $YBa_2Cu_3O_{6.5}$ induced by optical excitation. The spectral response at each time delay after excitation was obtained by keeping fixed the delay τ between the pump pulse and the electro-optic sampling gate pulse and scanning the single-cycle THz probe pulse with internal delay t across.

The stationary probe electric field $E_R(t)$ and the differential electric field $\Delta E_R(t,\tau)$ reflected from the sample were recorded simultaneously by feeding the electro-optic sampling signal into two lock-in amplifiers and mechanically chopping the pump and probe beams at different frequencies of ~357 and 500 Hz, respectively. The differential signal $\Delta E_R(t,\tau)$ was sampled at the ~143 Hz difference frequency of the two choppers. This approach minimized the cross-talk between the two detected signals whilst reducing the noise level of the measurements.

The electric field $E_R(t)$ and the differential field $\Delta E_R(t,\tau)$ were independently Fourier transformed to obtain the complex-valued, frequency-dependent $\tilde{E}_R(\omega)$ and $\Delta\tilde{E}_R(\omega,\tau)$. The photo-excited complex reflection coefficient $\tilde{r}(\omega,\tau)$ was determined by [6][11]

$$\frac{\Delta\tilde{E}_R(\omega,\tau)}{\tilde{E}_R(\omega)} = \frac{\tilde{r}(\omega,\tau)-\tilde{r}_0(\omega)}{\tilde{r}_0(\omega)} \tag{4.2}$$

where $\tilde{r}_0(\omega)$ denotes the stationary reflection coefficient.

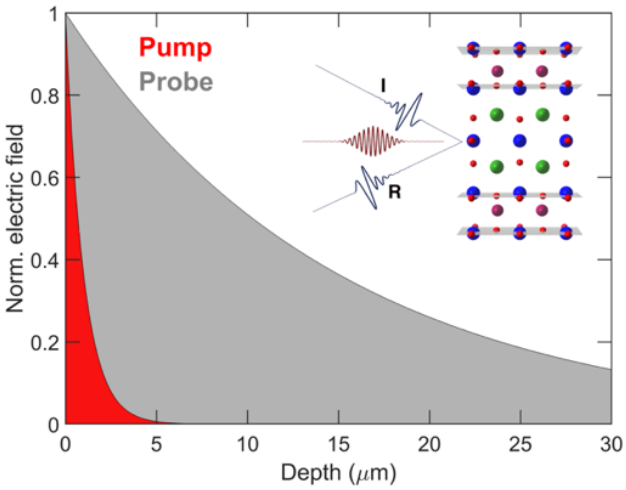

Figure 4.7. Penetration depth for the pump and probe beam in the experiment. The electric field of both pump (red) and probe (grey) exponential decay as a function of penetration. The inset illustrates the pump and probe beam together with the $YBa_2Cu_3O_{6.5}$ in the horizontal plane.

The penetration depth of the excitation pulses is a factor of ~2-10 smaller than that of the low-frequency THz probe pulses (Figure 4.7), implying that we were not probing a homogeneously excited sample volume. This mismatch was considered in the data analysis. At each frequency, the penetration depths of the electric fields into the material were calculated by $d(\omega) = \frac{c}{2\omega \cdot \mathrm{Im}[\tilde{n}_0(\omega)]}$ (here $\tilde{n}_0(\omega)$ is the stationary complex refractive index), yielding values of ~10–20 μm for the THz probe and in the range of ~1-5 μm for the pump pulses.

An accurate estimate of the photo-induced optical response functions was then achieved by treating the sample as a multi-layer system, in which only a thin layer below the sample surface is homogeneously excited while the bulk layer below remains unperturbed. The complex reflection coefficient is then expressed as

$$\tilde{\mathrm{r}}(\omega,\tau) = \frac{\tilde{\mathrm{r}}_A(\omega,\tau)+\tilde{\mathrm{r}}_B(\omega)e^{2i\delta(\omega,\tau)}}{1+\tilde{\mathrm{r}}_A(\omega,\tau)\tilde{\mathrm{r}}_B(\omega)e^{2i\delta(\omega,\tau)}} \tag{4.3}$$

Here, $\tilde{\mathrm{r}}_A(\omega,\tau)$ and $\tilde{\mathrm{r}}_B(\omega,\tau)$ correspond to the reflection coefficients at the interfaces vacuum/ photoexcited layer and photoexcited layer/unperturbed bulk, respectively, while $\delta = 2\pi d\tilde{n}(\omega,\tau)/\lambda_0$, with $\tilde{n}(\omega,\tau)$ being the complex refractive index of the photo-excited layer and λ_0 the probe wavelength.

Numerically solving this equation allowed us to retrieve $\tilde{n}(\omega,\tau)$ from the reflection coefficient $\tilde{\mathrm{r}}(\omega,\tau)$ obtained in the experiment. The complex optical conductivity for the homogeneously excited volume of the material is expressed as $\tilde{\sigma}(\omega,\tau) = \frac{\omega}{4\pi i}[\tilde{n}(\omega,\tau)^2 - \varepsilon_\infty]$, with $\varepsilon_\infty = 4.5$ as a standard value for high-T_C cuprates.

At each pump-probe time delay τ, the transient *c*-axis optical response functions were fitted either with a model including the response of a Josephson plasma or with a simple Drude-Lorentz model for normal conductors. A single set of fit parameters was always used to simultaneously reproduce the real and imaginary part of the optical conductivity, $\sigma_1(\omega)$ and $\sigma_2(\omega)$.

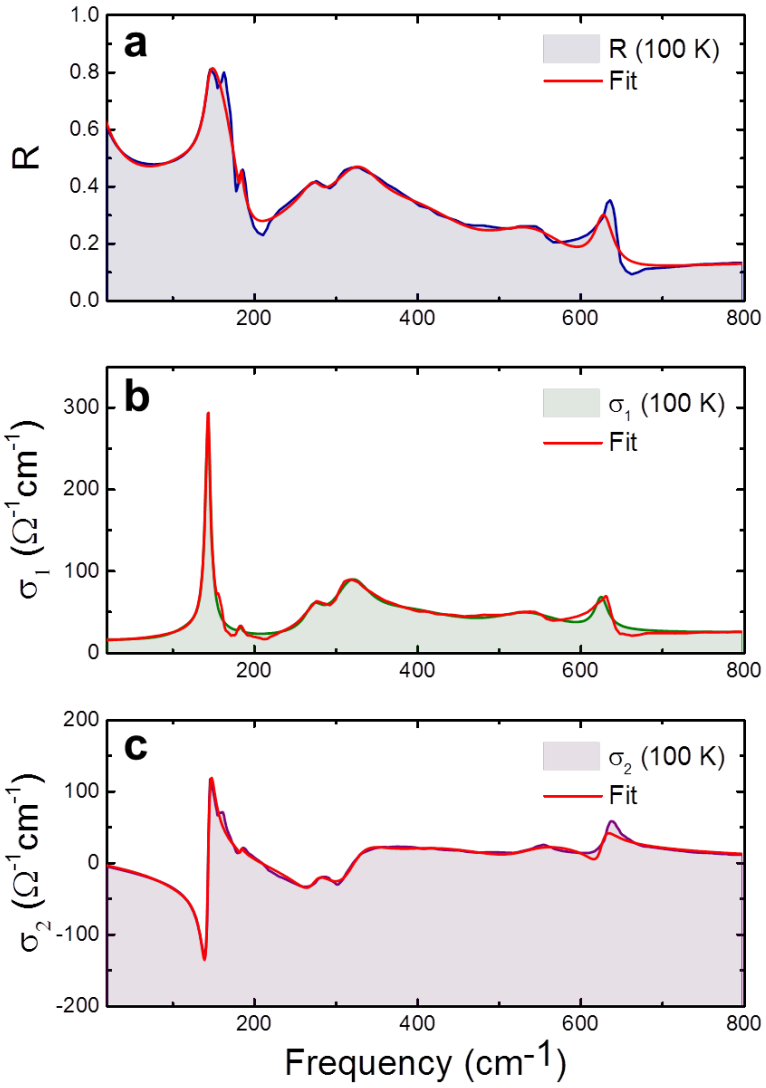

Figure 4.8. Equilibrium c-axis optical properties of $YBCO_{6.5}$ at 100 K fitted with Drude-Lorentz model. The colorful curves with shadows are **(a)** reflectance, (b) real part and **(c)** imaginary part of optical conductivity. The red curves are the fits with one set of fitting parameters which are listed in Table 4.1.

The phonon modes in the mid-infrared ($150\ \text{cm}^{-1} \lesssim \omega \lesssim 700\ \text{cm}^{-1}$) and the high-frequency electronic absorption ($\omega \gtrsim 3000\ \text{cm}^{-1}$) were constructed by fitting the equilibrium spectra with Lorentz oscillators, for which the complex dielectric function is expressed as:

$$\tilde{\varepsilon}_{HF}(\omega) = \sum_i \frac{S_i^2}{(\Omega_i^2 - \omega^2) - i\omega\Gamma_i}. \tag{4.4}$$

Here, Ω_i, S_i, and Γ_i are the central frequency, strength, and damping coefficient of the i-th oscillator, respectively. In all fitting procedures to the transient data, these high-frequency terms were kept fixed.

By fitting the equilibrium spectra with 9 Lorentz oscillators in the form given by formula (4.4), the reflectivity (Figure 4.8(a)), and the real and imaginary part of optical conductivity (Figure 4.8(b-c)) of $YBCO_{6.5}$ perpendicular to the CuO_2 at 100 K (normal state) can be reproduced. The corresponding fitting parameters are listed in Table 4.1, which are used in the evaluation of the light-induced state as the high-frequency phonon contribution to the optical constants.

Table 4.1. Fitting parameters for the equilibrium c-axis optical properties of $YBCO_{6.5}$ at 100 K. Typical value at 4.5 for ε_{inf} and 9 oscillators are taken into consideration.

No.	Parameter	Value	No.	Parameter	Value
0	ε_{inf}	4.5	**15**	$\omega_{P,5}$	441.341
1	$\omega_{P,Drude}$	444.06	**16**	γ_5	56.184
2	γ_{Drude}	222.512	**17**	$\omega_{0,5}$	321.689
3	$\omega_{P,1}$	264.235	**18**	$\omega_{P,6}$	553.069
4	γ_1	68.299	**19**	γ_6	172.165
5	$\omega_{0,1}$	132.189	**20**	$\omega_{0,6}$	392.627
6	$\omega_{P,2}$	359.951	**21**	$\omega_{P,7}$	366.502
7	γ_2	8.486	**22**	γ_7	102.636
8	$\omega_{0,2}$	144.331	**23**	$\omega_{0,7}$	536.725
9	$\omega_{P,3}$	39.177	**24**	$\omega_{P,8}$	212.796
10	γ_3	3.195	**25**	γ_8	19.556
11	$\omega_{0,3}$	184.599	**26**	$\omega_{0,8}$	627.183
12	$\omega_{P,4}$	206.293	**27**	$\omega_{P,9}$	14352.1
13	γ_4	27.436	**28**	γ_9	98382
14	$\omega_{0,4}$	274.177	**29**	$\omega_{0,9}$	855.97

The low-frequency Drude contribution to the complex dielectric function is expressed as

$$\tilde{\varepsilon}_D(\omega) = \varepsilon_\infty[1 - \omega_P^2/(\omega^2 + i\Gamma\omega)], \tag{4.5}$$

where ω_P and Γ are the Drude plasma frequency and momentum relaxation rate, which were left as free fitting parameters, while ε_∞ was kept fixed to 4.5.

The dielectric function of the Josephson plasma is expressed instead as

$$\tilde{\varepsilon}_J(\omega) = \varepsilon_\infty + \tilde{\varepsilon}_N(\omega). \tag{4.6}$$

Here, the free fitting parameters are the Josephson plasma frequency, ω_J, and $\tilde{\varepsilon}_N(\omega)$, a weak "normal fluid" component [163][182] (overdamped Drude term), which was introduced to reproduce the positive offset in $\sigma_1(\omega)$.

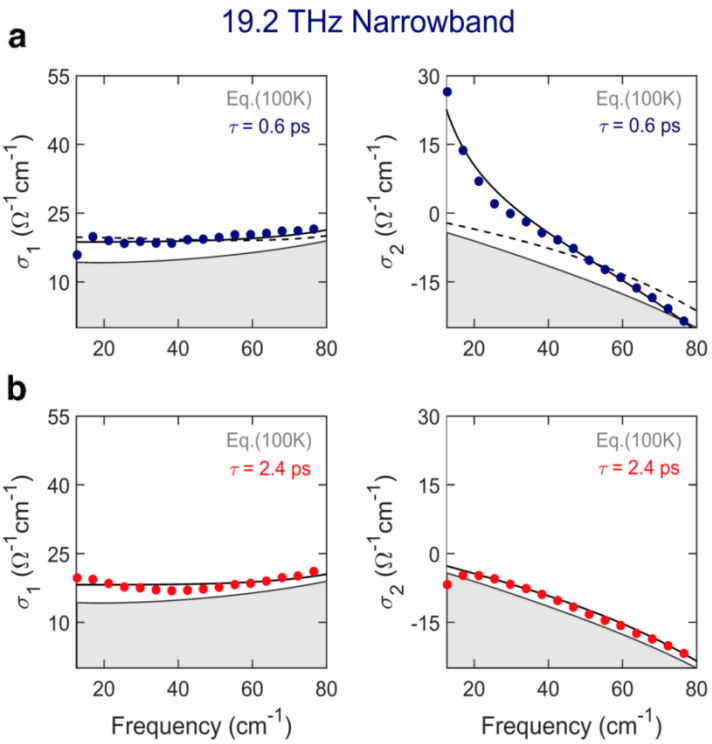

Figure 4.9. Fits to the transient complex optical conductivity measured after narrowband excitation at ω_{pump}= 19.2 THz (T = 100 K). **(a)** Real and imaginary part of the optical conductivity measured at τ = 0.6 ps pump-probe time delay (blue dots). Grey curves with shading are the corresponding equilibrium spectra (shown also in panels b). The black solid line is a fit with the Josephson plasma model. The dashed black curve is instead a failed fit attempt using a simple Drude term for normal conductors. **(b)** Real and imaginary conductivity measured at τ = 2.4 ps time delay (red dots). This dissipative response could be well reproduced by the Drude-Lorentz model (black solid lines).

As an example, the photo-induced optical conductivity for 19.2 THz narrowband excitations on resonance with the more effective apical oxygen mode at different time delays τ = 0.6 ps and 2.4 ps and the corresponding fits are reported in Figure 4.9 In Figure. 4.9(a), at early time delay (τ = 0.6 ps), the Josephson plasma model (black solid lines) is able to reproduce the experimental data. Notably, a Drude response alone (dashed lines) would not capture the measured low-frequency increase in $\sigma_2(\omega)$. At later time delays (Figure. 4.9(b)), for which the system has already evolved into a dissipative response, the experimental data could instead be well reproduced by the simple Drude model for normal conductors.

4.4 Light-induced superconductivity above T_C

The discovery of a light-induced highly coherent state above the thermodynamic superconducting transition temperature has opened up new perspectives for the control of

high-T_C superconductivity on ultrafast time scales. In this section, the pump-induced *c*-axis electrodynamics of $YBCO_{6.5}$ above T_C will be investigated when different IR-active phonons are resonantly excited.

4.4.1 Broadband excitation of apical-oxygen phonons

The nonequilibrium dynamics of $YBCO_{6.5}$ at 100 K (above T_C) after broadband excitation (4 THz bandwidth) have been investigated when the "YBCO6" and "YBCO7" modes are simultaneously excited. The pump-induced change at the peak of the THz probe electric field, measured at T = 100 K, is reported in Figure 4.10(a). The pump-probe signal displays a ~0.2 ps rise time. After reaching the maximum, the light-induced signal decays back to the equilibrium within a few picoseconds, a relaxation time which is much faster compared with that found below T_c (> 10 ps). In Figure 4.10(b), the stationary probe EOS trace and the light-induced ΔE at τ = 0.4 ps time delay are reported.

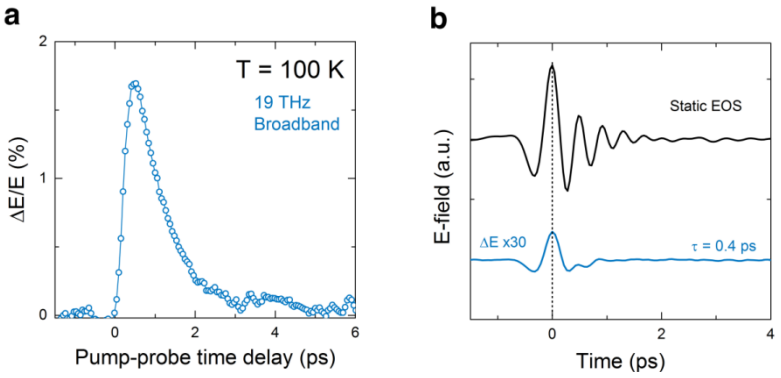

Figure 4.10. (a) Pump-induced changes at the peak of the THz probe electric field as a function of pump-probe time delay, measured in $YBCO_{6.5}$ at T = 100 K (> T_C) for broadband 19 THz excitation. **(b)** Stationary reflected probe electric field and corresponding pump-induced electric field changes at τ = 0.4 ps time delay.

In Figure 4.11, we report the frequency- and time-delay-dependent pump-induced optical properties measured after broadband 19 THz excitation at 100 K. The peak of the coherent response was found at τ = 0.4 ps (white dashed line), where the increase of transient σ_2 reached its maximum. At later time delays, also the real part of optical conductivity σ_1, gets more pronounced. The pump-induced divergence in σ_2 is compared with the superconducting transition in the equilibrium state. Importantly, for the very same time delay, the increase in σ_1 is negligible, an observation which allows to exclude any metallic response from normal quasiparticles and is rather suggestive of coherent, dissipation-less transport, compatible with transient superconductivity.

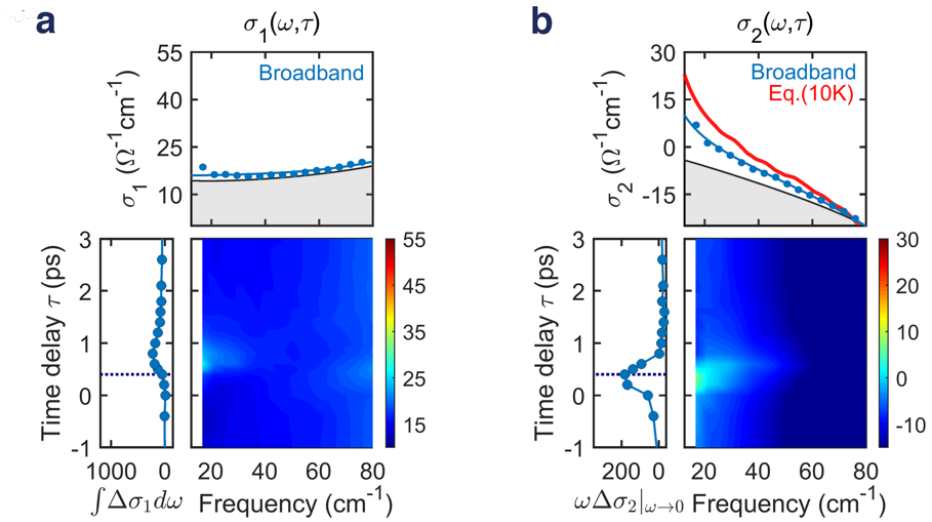

Figure 4.11. (a) Color plots: Frequency- and time-delay-dependent complex optical conductivity measured after broadband excitation at T = 100 K. Upper panels: corresponding $\sigma_1(\omega)$ and $\sigma_2(\omega)$ line cuts displayed at equilibrium (lines) and at the peak of the coherent response ($\tau \simeq 0.5$ ps, circles). Lines are fits to the transient spectra with a model describing the response of a Josephson plasma. For comparison, we also report the equilibrium $\sigma_2(\omega)$ measured in the superconducting state at T = 10 K (red line). Side panels: Frequency-integrated dissipative ($\int \Delta\sigma_1(\omega)d\omega$) and coherent ($\omega\sigma_2(\omega)|_{\omega\to 0}$) responses, as a function of pump-probe time delay. The delay corresponding to the spectra reported in the upper panels ($\tau \simeq 0.5$ ps) is indicated by a dashed line.

We define two figures of merit to describe the transient optical response. $\int \Delta\sigma_1(\omega)d\omega$, the integrated change in σ_1 (side plot in Figure 4.11(a)), represents the dissipation and quasiparticle heating inside the gap. In the side plot of Figure 4.11(b), the low-frequency limit $\omega\sigma_2(\omega)|_{\omega\to 0}$ indicated by the red dashed line represents the quantity proportional to the superfluid density in a superconductor. We plot $\int \Delta\sigma_1(\omega)d\omega$ and $\omega\sigma_2(\omega)|_{\omega\to 0}$ as a function of time delay, showing how the dissipative part of the optical response ($\int \Delta\sigma_1(\omega)d\omega$) increases only at later time delays compared to the superconducting component, reaching a maximum after the peak in $\omega\sigma_2(\omega)|_{\omega\to 0}$, has relaxed.

4.4.2 Narrowband mode-selective phonon excitation

"YBCO6" and "YBCO7" modes

A direct comparison of the contribution from the two apical-O modes to the light-induced coherent state in $YBCO_{6.5}$ above T_C was performed by vibrationally exciting the system at 19.2 THz and 16.4 THz with fluence ~ 8 mJ/cm^2 and field strength ~ 3 MV/cm. The pump-induced changes of the peak probe field are reported in Figure 4.12(a) for both narrowband

excitations, which exhibit nearly identical responses. The difference in the field change, ΔE, at the selected time delay (0.6 ps) for both excitations is also negligible, which can be seen in Figure 4.12(b).

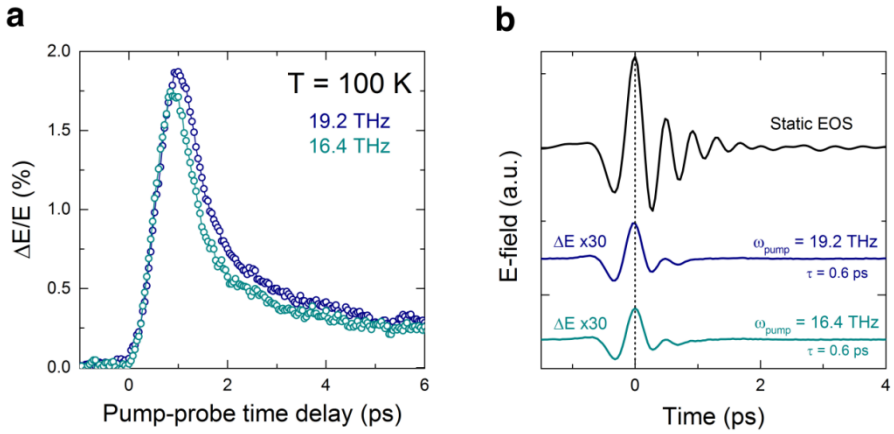

Figure 4.12. (a) Pump-induced changes at the peak of the THz probe electric field as a function of pump-probe time delay, measured in $YBCO_{6.5}$ at T = 100 K (below Tc) for narrowband excitation at 16.4 THz and 19.2 THz excitations. **(b)** The static reflected probe electric field and corresponding pump-induced electric field changes for 19.2 THz and 16.4 THz at pump-probe delay τ = 0.6 ps.

In Figure 4.13, the pump-induced optical conductivity measured after narrowband 19.2 THz and 16.4 THz excitations at T = 100 K are plotted as a function of frequency and pump-probe time delay. At τ = 0.6 ps time delay, the coherent σ_2 response reaches its maximum, while the σ_1 evolves at later times, reaching the maximum at $\tau \sim 1$ ps. In the narrowband measurement, the temporal separation between σ_1 and σ_2 are more pronounced (~ 0.5 ps) compared with the broadband measurement. The solid lines in the upper panels are the numerical fits of the transient optical conductivity using a model describing the optical response of a Josephson plasma.

If we look at the corresponding transient optical constants at τ = 0.6 ps, for narrowband excitation at 19.2 THz, we observed the same $\sigma_2(\omega)$ spectrum measured in the equilibrium superconducting state.

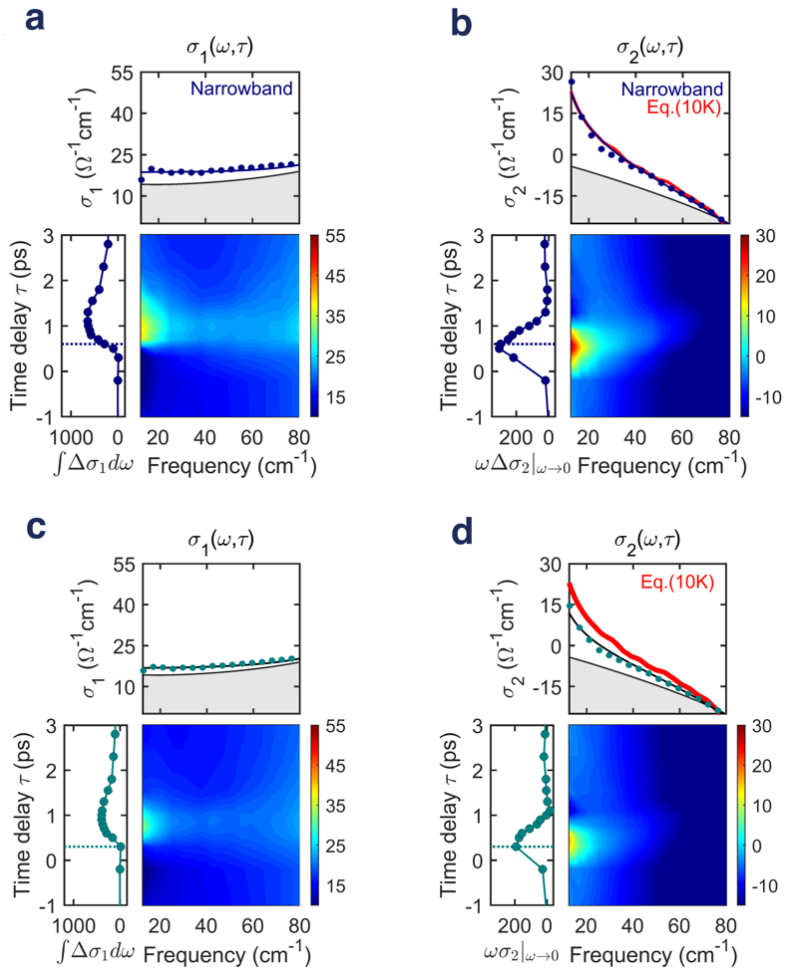

Figure 4.13. (a-b) Color plots: Frequency- and time-delay-dependent complex optical conductivity measured after broadband excitation at T = 100 K. Upper panels: corresponding $\sigma_1(\omega)$ and $\sigma_2(\omega)$ line cuts displayed at equilibrium (grey lines) and at the peak of the coherent response ($\tau \simeq 0.6$ ps time delay, blue circles). Black lines are fits to the transient spectra with a model describing the response of a Josephson plasma. For comparison, we also report the equilibrium $\sigma_2(\omega)$ measured in the superconducting state at T = 10 K (red line). Side panels: Frequency-integrated dissipative ($\int \Delta\sigma_1(\omega)d\omega$) and coherent ($\omega\sigma_2(\omega)|_{\omega\to 0}$) responses, as a function of pump-probe time delay. The delay corresponding to the spectra reported in the upper panels ($\tau \simeq 0.5$ ps) is indicated by a dashed line. **(c-d)** Same quantities as in (a-b), measured for narrowband excitation at 16.4 THz, in which the apical-O mode in the Oxygen-filled chain is resonantly excited.

"Barium mode" and "Cu-O planar bending mode"

The investigation was also extended to the lower energy phonon modes on the "Barium mode" at 4.2 THz and the Cu-O bending mode at 10.2 THz in the insulating state at 100 K. The dynamical evolution of the pump-induced changes in the complex optical conductivity, reflectivity, and energy loss function at 100 K are shown for narrowband excitation at 4.2 THz, and 10.1 THz in Figure 4.14. For both excitations, the changes in σ_2 for both lower energy modes are less pronounced compared with the high-frequency excitations with no

positive value exits at the lowest measured frequency. The light-induced change in other optical constants is marginal as well.

As aforementioned, the THz excitation of the system can be separated into two processes: the coherent excitation of the target phonon mode and the incoherent energy dissipation process. In a phonon excitation process, the driving force is proportional to the applied pump field and the ratio between the Born effective charge and the effective mass of the driven phonon. The latter is the intrinsic property of the driven phonon. To study the photo-susceptibility of the light-induced effect by exciting different phonon modes, so we experimentally keep the pump electric field and pump fluence to be constant.

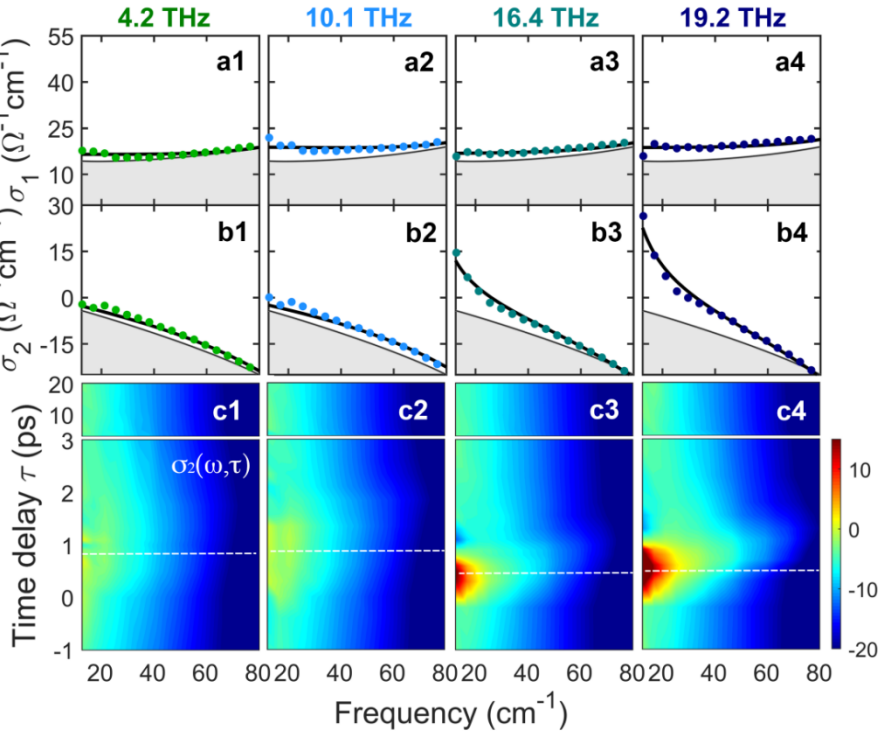

Figure 4.14. Transient *c*-axis optical response induced by mode-selective phonon excitations above T_C. **(a-b)** Complex optical conductivity, $\sigma_1(\omega) + i\sigma_2(\omega)$, measured before (black lines) and after (colored circles) resonant stimulation of the phonon modes shown in Figure 4.9 with ~3 MV/cm peak electric fields. The black solid lines are fits to the transient spectra performed with either a simple Drude-Lorentz model for normal conductors (a1, a2, b1, b2) or a model describing the response of a Josephson plasma (a3, a4, b3, b4). The corresponding time delays are chosen at the maximum change in $\sigma_2(\omega)$, which are indicated in **(c)** by the white dashed lines.

A direct comparison of the light-induced complex optical conductivity for different excitation at 4.2 THz, 10.2 THz, 16.4 THz and 19.2 THz with ~3 MV/cm field strength is given in Figure 4.14. When the two high-frequency modes at 16.4 THz and 19.2 THz were

excited, a superconducting-like response ($\sigma_2(\omega) \propto 1/\omega$) was induced, which could be fitted by a model describing the optical response of a Josephson plasma. In contrast, excitation of the two low-frequency modes (at 4.2 THz and 10.1 THz) induced a moderate increase in dissipation and no superconducting component. This observation could be well reproduced, for all time delays, by a simple Drude-Lorentz model for normal conductors.

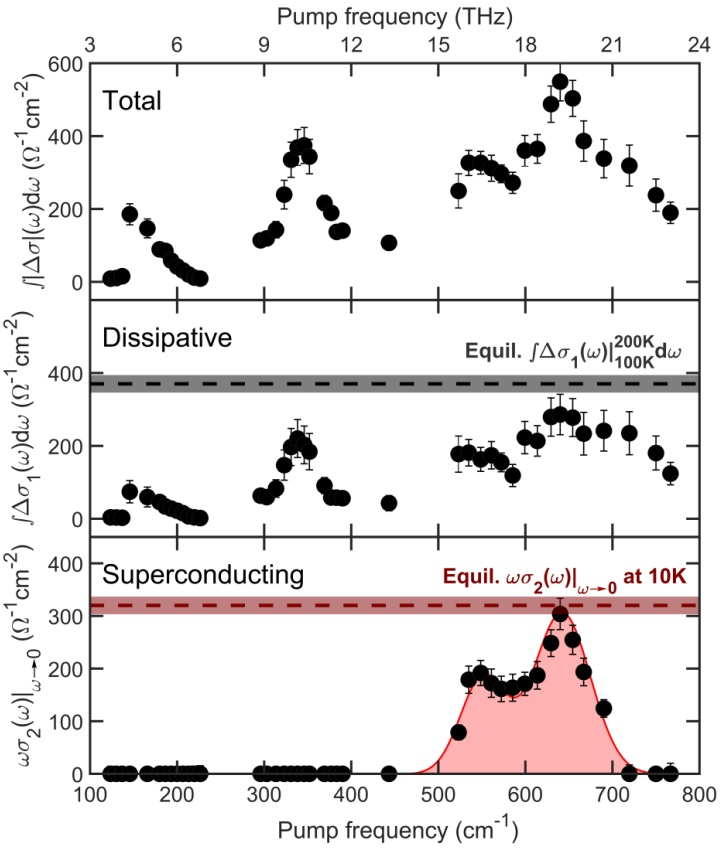

Figure 4.15. Evolution of the photo-induced response at T = 100 K as a function of excitation frequencies. Distinct quantities, extracted from the transient optical conductivity at $\tau \simeq 0.5$ ps time delay, are displayed as a function narrowband excitation frequency: **(a)** The total, frequency integrated change in optical conductivity $\int|\Delta\sigma(\omega)|d\omega$, **(b)** The frequency integrated dissipative response, $\int\Delta\sigma_1(\omega)d\omega$, and **(c)** The superconducting response represented by the low-frequency limit $\omega\sigma_2(\omega)|_{\omega\to 0}$. The red shaded region represents the frequency range around the apical oxygen phonon modes, where a transient superconducting-like response could be identified. Horizontal dashed lines indicate the thermally-induced increase in $\int\sigma_1(\omega)d\omega$ when heating the sample from 100 K to 200 K (black) and the equilibrium superfluid density, $\omega\sigma_2(\omega)|_{\omega\to 0}$, measured at T = 10 K (red) [35].

The same experiments as those reported in Figure 4.14 were systematically repeated for 42 pump frequencies throughout the far-infrared spectrum (3 – 24 THz). Figure 4.15 reports the analysis of the transient optical properties at the optimum time delay of the coherent response. The top panel shows the total spectrally integrated probe signal, which is the modulus of the complex optical conductivity. In the middle plot, the dissipative component of

the signal ($\int \Delta\sigma_1(\omega)d\omega$) and the superconducting contribution $\omega\sigma_2(\omega)|_{\omega\to 0}$ are depicted in the middle and lower panel, respectively. The thermally-induced increase ($\int \Delta\sigma_1(\omega)d\omega$) from 100 K to 200 K (middle panel) and the equilibrium superfluid density measured at10 K (lower panel) are included for better comparison.

For excitation in the vicinity of 16.4 THz and 19.2 THz, the nonequilibrium state includes a dissipative $\int \Delta\sigma_1(\omega)d\omega$ response that coexists with a superconducting-like imaginary conductivity ($\omega\sigma_2(\omega)|_{\omega\to 0}$) identical to the superfluid density at equilibrium superconducting state. On the other hand, when the pump frequency is tuned below 15 THz, no superconducting component is observed, whereas the dissipative response is approximately the same as that observed for pump frequency below 15 THz.

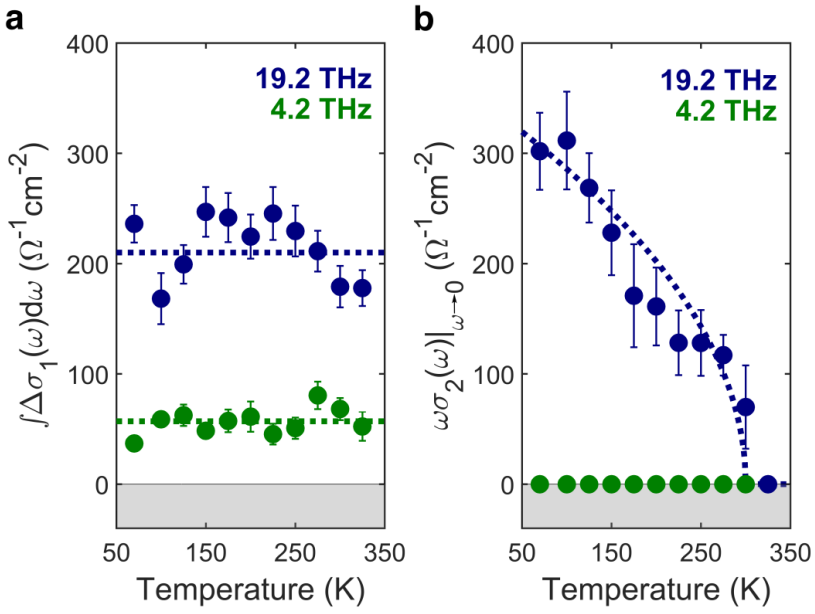

Figure 4.16. Temperature-dependent **(a)** dissipative response, $\int \Delta\sigma_1(\omega)d\omega$, and **(b)** superconducting-like response, $\omega\sigma_2(\omega)|_{\omega\to 0}$, measured for resonant narrowband excitation of the lowest-frequency (4.2 THz) and highest-frequency (19.2 THz) phonon modes. The dashed lines are guides to the eye [35].

The different nature of the dissipative and the superconducting-like signal is further underscored by the temperature-dependent $\int \Delta\sigma_1(\omega)d\omega$ and $\omega\sigma_2(\omega)|_{\omega\to 0}$ reported in Figure 4.17. In Figure 4.16(a), the dissipative responses for both excitations are temperature-independent and persist up to 325 K. On the other hand, the superconducting-like response (Figure 4.16(b)), which is observed only for high-frequency pumping (blue), displays a strong reduction with increasing temperature, almost disappearing for T > 300 K. This is consistent with the observation reported in Ref.[6].

4.5 Enhancement of superconductivity below T_C

In this section, I discuss in detail a systematic study of optically-enhanced superconductivity below T_C, as well as of optically-induced superconductivity above T_C via mode-selective excitation of different phonons along the *c*-axis of the bi-layer cuprate $YBCO_{6.5}$.

The $YBCO_{6.5}$ sample was first investigated in its superconducting state, at T = 10 K. The equilibrium optical properties along the c-axis were presented previously in Figure 4.2, with the most prominent signatures of a Josephson plasma resonance at ~ 33 cm^{-1} (~ 1 THz) and a divergence in lower frequency in σ_2. The equilibrium superconducting response could also be directly measured in THz time-domain setup, in which the pump pulses were switched off. The superconducting transition across T_C could be characterized by measuring the reflected THz transient in the equilibrium superconducting (10 K) and normal (60 K) state. Figure 4.17(a) depicts the detected THz field reflected from the sample at both temperatures, whilst figure 4.17(b) illustrates the corresponding normalized Fourier transform amplitudes**.** Clearly, the spectral weight at 30 cm^{-1} in the normal state transfers to the lower frequency range upon cooling, which is indicative of a sharp reflectivity edge appearing through the superconducting transition. This is shown in Figure 4.17(c), where we display the THz reflected field ratios ($T < T_c$, divided by $T > T_c$). These equilibrium THz time domain spectra were taken regularly, in order to control the stability of the doping level, as well as the sample quality.

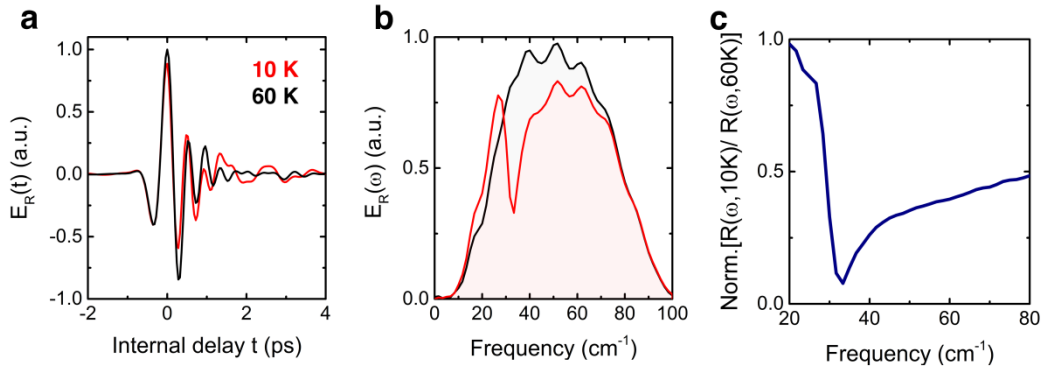

Figure 4.17. (**a**) Stationary electric field profile measured after reflection from $YBa_2Cu_3O_{6.5}$ at $T < T_C$ (red) and $T \gtrsim T_C$ (black). (**b**) Fourier transform amplitude of both quantities shown in panel (a). (**c**) Normalized reflectivity ratio extracted from the spectra in panel (b), showing a Josephson Plasma Resonance at $\omega \simeq 33$ cm^{-1}, in agreement with literature data [154]. Figure taken from Ref. [35].

4.5.1 Broadband excitation of the apical-oxygen modes

We investigated the nonequilibrium dynamics of $YBCO_{6.5}$ below the superconducting transition temperature after broadband ($\Delta\nu\sim$ 4 THz) excitation at ~20 THz. The pump pulses were polarized perpendicular to the CuO_2 planes, which induced atomic motions of both "YBCO6" and "YBCO7" modes.

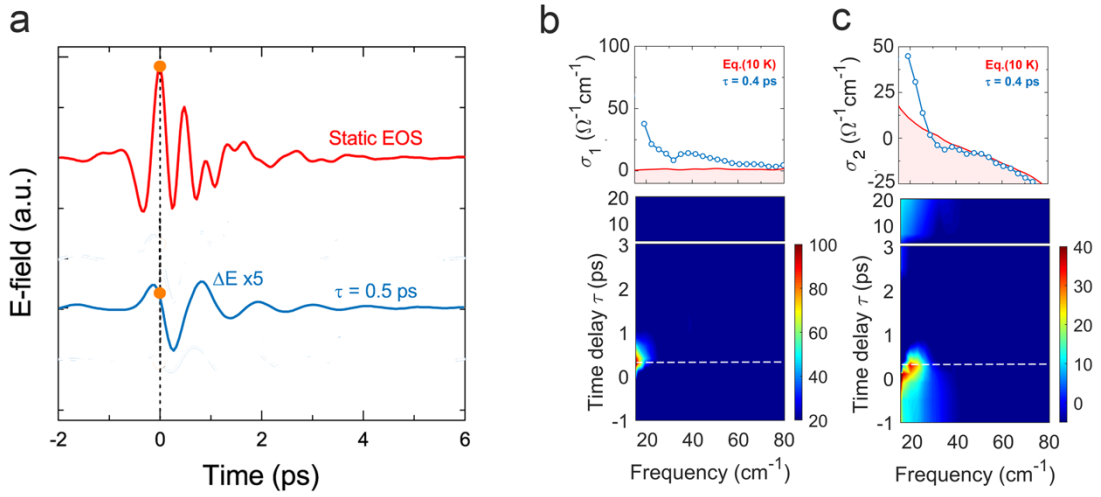

Figure 4.18. (a) Stationary reflected probe electric field and corresponding pump-induced electric field changes for 20 THz broadband excitations at a pump-probe delay τ = 0.5 ps. **(b-c)** Frequency- and time-delay-dependent pump-induced optical conductivity measured after broadband excitation at 20 THz (T = 10 K, below T_C). The white dashed lines indicate the pump-probe time delay τ = 0.5 ps.

The reflected stationary probe field and the corresponding pump-induced field changes at early and later time delays are reported in Figure 4.18(a). The phase shift in individual *ΔE* traces is highlighted marked by the yellow dots. By varying the pump-probe time delay, the frequency- and time-delay-dependent pump-induced optical properties were measured. In Figure 4.18(b), the complex optical conductivity is shown in color plots as a function of frequency and time. As indicated by the white dashed lines, for time delays right after excitation we observed a transient response characterized by an increased σ_2 at low frequency. We take the presence of a positive transient $\sigma_2(\omega)$, which monotonously increases for $\omega\rightarrow0$ as $\sim1/\omega$, as a fingerprint for an optically-driven superconducting-like response. Here, the quantity $\omega\sigma_2(\omega\rightarrow0)$, which becomes maximum for a time delay τ = 0.4 ps, is proportional to the *c*-axis superfluid stiffness and can be taken as an indicator of the strength of the transient coherent response. The corresponding optical properties measured at this specific time delay are reported in the upper panel in Figure 4.18(b). Notably, the light-induced enhancement of superconductivity, expressed by $\omega\sigma_2(\omega\rightarrow0)$, was accompanied by a slight upturn in σ_1,

which can be explained, within a two-fluid scenario, as being due to heating of unpaired quasiparticles.

4.5.2 Narrowband mode-selective phonon excitation

"YBCO6" modes

By exploiting the new narrowband THz source, the light-induced dynamics in $YBCO_{6.5}$ was studied by exciting the "YBCO6" mode with intense 20 THz narrowband pulses. The central frequency "YBCO6" modes are slight hardened at 10 K compared with the ones in the normal state. Figure 4.19(a) depicts the measurement of the pump-induced change of the peak probe electric field for both narrowband excitation at 20.5 THz. The measured $\Delta E/E$ under 20.5 THz excitation exhibited similar behavior as the broadband excitation.

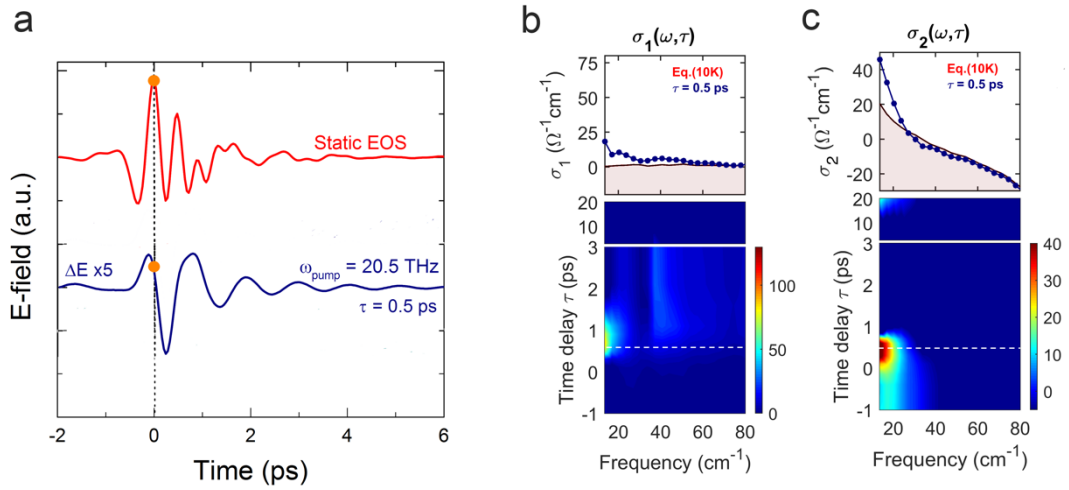

Figure 4.19. (a) Stationary reflected probe electric field and corresponding pump-induced electric field changes for 20.5 THz narrowband excitations at a pump-probe delay τ = 0.5 ps. **(b-c)** Frequency- and time-delay-dependent pump-induced optical conductivity measured after narrowband excitation at 20.5 THz (T = 10 K, below T_C). The white dashed lines indicate the pump-probe time delay τ = 0.5 ps.

The corresponding time delay evolution of the pump-induced optical constants is shown in Figure 4.19(b-c). The color plots show the frequency- and time-dependent measurement of the nonequilibrium optical conductivity after the narrowband excitations, while the upper panels show the light-induced optical conductivity for 20.5 THz narrowband excitations together with the value at equilibrium. The data shows an enhanced response which is quite similar to that following broadband excitations. For example, at the time delay corresponding

to the maximum enhancement of superconducting coherence (τ = 0.5 ps), we found a significant increase in σ_2 accompanied by an offset in σ_1. These results suggest that superconducting coherence below T_C can be individually enhanced by large-amplitude excitations of the "YBCO6" mode, which involves motion of apical-O atoms in the oxygen-vacant chains.

"Barium mode"

Similar nonequilibrium measurement was extended to the lower energy phonon modes using the narrowband source. When the central frequency of the pump pulse was tuned to 4.2 THz, the "Barium mode" was resonantly excited. This mode, as described before, can be associated with complex atomic motions involving Barium atom stretching, CuO_2 plane bulking and the apical-O stretching in the oxygen-filled chains.

Figure 4.20 summarizes the related optical constants for narrowband excitation at 4.2 THz at 10 K below T_C. As depicted in Figure 4.20(a), the equilibrium superconducting coherence is suppressed by vibrational excitation of the "Barium mode". Figure 4.20(b-c) reveal the pump-induced at 0.5 ps, where the value σ_2 was completely below zero.

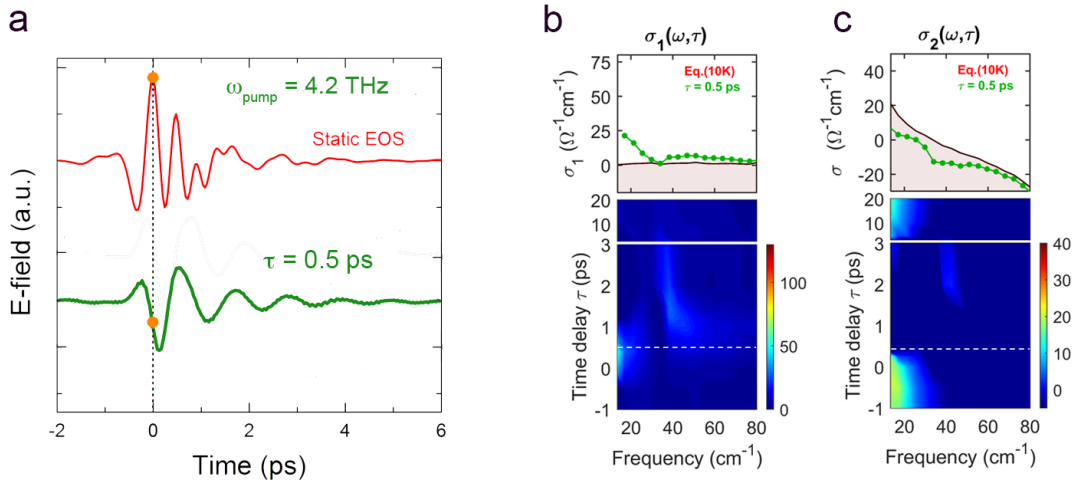

Figure 4.20. (a) Stationary reflected probe electric field and corresponding pump-induced electric field changes for 4.2 THz narrowband excitations at a pump-probe delay τ = 0.5 ps. **(b-c)** Frequency- and time-delay-dependent pump-induced optical conductivity measured after narrowband excitation at 4.2 THz (T = 10 K, below T_C). The white dashed lines indicate the pump-probe time delay τ = 0.5 ps.

Overall, a mode-selective investigation of light-enhanced superconductivity in bi-layer cuprates $YBCO_{6.5}$ has been realized with the newly developed narrowband THz source. The transient enhancement of coherence along the *c*-axis has been evidenced to take place only

via excitations around 20.5 THz, corresponding to the atomic motion involving the apical-O ions in the oxygen-vacant chains.

4.6. Discussion

In this section, the experimental observations in the narrowband vibrational phase control of cuprate $YBCO_{6.5}$ will be further discussed together with the calculated structure deformations and the change of electronic properties. The transient optical properties of $YBCO_{6.5}$ along the *c*-axis induced by higher energy photons in a second measurement will be also reported, providing insights into the explanation of the induced superconductivity in cuprates.

Light-induced state and structure deformation

Following the procedure described in Appendix C.1, the time-dependent crystal structures for different excitation frequencies between 2.5 and 22 THz were calculated based on ab-initio calculation. According to the nonlinear phononics theory, the large-amplitude excitations of the IR-active modes result in transient displacements of A_g modes, involving an average lattice distortion. Figure 4.21 shows the maximum changes of selected bonds (distance of the apical-O atoms from the CuO_2 planes, inter-bilayer distance of the CuO_2 planes, and buckling of the CuO_2 planes) calculated from these average phonon displacements. Peak electric field and pulse duration for all driving frequencies were kept fixed at 3 MV/cm and 0.6 ps, respectively.

For excitations between 5 and 10 THz, a significant shift of the apical-O atoms closer to the CuO_2 planes is presented, accompanied by a buckling within the CuO_2 layers and an increase in the intra-bilayer distance. In contrast, very different rearrangements were found for driving frequencies within the range for which photo-induced superconducting coherence was observed. Prominently, the apical-O atoms moved away from the CuO_2 planes for resonant driving of the 20.5-THz phonon, while excitation of the 16.5-THz mode shifted the atoms closer to the planes. In both cases, we also calculated different signs for the CuO_2 plane buckling and the intra-bilayer distance, which increased for 16.5-THz but decreased for the 20.5-THz excitation.

In the nonequilibrium state above T_C, the light-induced superconducting-like states were observed by individually pumping each of the apical-O modes using narrowband pulses at 16.4 THz and 19.2 THz. On the other hand, the excitations of “Barium mode” at 4.2-THz and

the "planar Cu-O bending mode" 10-THz only induce modest dissipation. The prominent feature given by the pump-frequency dependence measurement in the pseudogap phase of $YBCO_{6.5}$ is the frequency band in the vicinity of the two apical-O modes in Figure 4.21, as highlighted in grey. However, the observed frequency band for light-induced superconductivity is not consistent with the transient crystal structures given by the DFT calculation. These results put some doubts on the significance of anharmonic phonon coupling as a possible mechanism for optically-driven superconductivity in $YBa_2Cu_3O_{6+x}$, as posited earlier in Ref. [10].

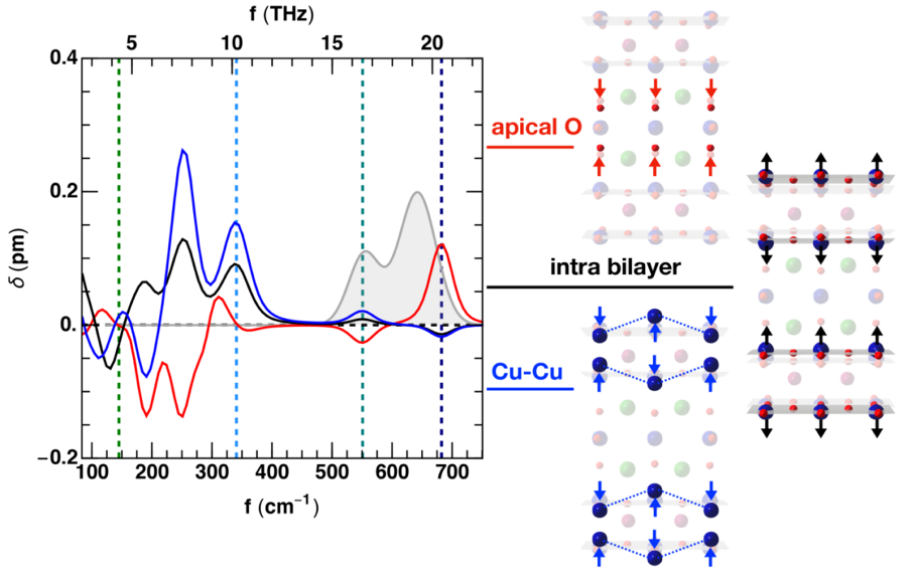

Figure 4.21. Transient average distortions of the apical-O positions (red), the intra-bilayer distance (black) and the planar Cu buckling (blue) in $YBa_2Cu_3O_{6.5}$, derived from ab-initio calculations of nonlinear phonon-phonon interactions for different excitation frequencies. The grey shaded area depicts the experimentally determined frequency range of the optically-enhanced superconducting response shown in Figure 4.17. The excitation parameters of 600 fs pulse duration and 3 MV/cm peak electric field, used in the calculations, reproduce the experimental conditions. Arrows in the illustrations shown on the right correspond to positive displacements [35].

Modulation of electronic properties

The experimental data suggests the significant role that the apical-O ions play in the transient superconducting-like state. It is plausible that, instead of inducing a transient lattice deformation via nonlinear phononics, the polar motion of the apical-O modes could directly modify the electron structures, favoring the pair formation and interlayer tunneling.

It is evident that the apical-O ions play a critical role in the superconductivity in $YBCO_{6+x}$ compounds at equilibrium. The copper-oxygen bond length along the *c*-axis has

been carefully investigated in neutron diffraction [191], x-ray absorption spectroscopy (XAS) [192] and other techniques. For example, R. J. Cava *et al*. demonstrated the changes in the structural and electronic properties as a function of oxygen stoichiometry by means of neutron scattering. An abrupt increase in positive charge was observed in the plane Cu(2) layer through the transition from semiconductor to superconductor [191]. The importance of charge transfer in controlling T_C of layered cuprates was further evidenced by S. D. Conradson *et al*. in the copper K-edge XAS measurement [192]. In an optimally-doped $YBCO_7$ sample, the mean square relative displacement of some Cu(2)-O(4) bonds became smaller with a slight increase in the Cu(1)-O(4) distance across the superconducting transition, which confirmed the role of the Cu(1) chains as a charge reservoir and the significance of the O(4) in bridging different superconducting layers [193].

If the charge transfer between the CuO_2 layers and the insulating layers is the key for the light-induced superconducting-like state, a direct control of the electronic properties by exciting the material with higher energy photons becomes interesting. To better understand the microscopic process, a second pump-probe experiment studying the transient optical responses of 12 new pump wavelengths ranging from 10 μm to 400 nm was performed.

In Figure 4.22, we report similar measurements with excitations at higher photon energies, and display the transient complex conductivity at the peak of the light-induced response for three representative excitation frequencies: 29 THz ($\lambda_{pump} = 10.4$ μm), 214 THz ($\lambda_{pump} = 1.4$ μm), and 375 THz ($\lambda_{pump} = 800$ nm). Similar to what reported Figure 4.23 for frequencies right above 19 THz, the response at 29 THz ($\lambda_{pump} = 10.4$ μm) displays no superconducting-like component. However, for excitation frequencies of 214 THz ($\lambda_{pump} = 1.4$ μm) and 375 THz ($\lambda_{pump} = 800$ nm) a transient $\sigma_2(\omega) \propto 1/\omega$ is observed again, resembling that induced by driving resonant with the apical oxygen phonons.

A complete pump frequency dependence for the superconducting component $\omega\sigma_2(\omega)|_{\omega\to 0}$ is displayed in Figure 4.23(a). For almost all of our data shown here, excluding those taken for $\lambda_{pump} = 800$ nm and $\lambda_{pump} = 400$ nm, we kept not only the peak driving field (~3 MV/cm) but also the pump pulse length (~600 fs) fixed. At $\lambda_{pump} = 800$ nm and $\lambda_{pump} = 400$ nm, for which the pulses were shorter (~100 fs), two different data points are taken both at ~8 mJ/cm^2 (~7 MV/cm) and ~1.5 mJ/cm^2 (~3 MV/cm).

The data confirm the presence of two pump frequency resonances of comparable amplitude, one in the MIR phonon region and one in the NIR/visible regime. A negligible response of the imaginary conductivity is found for all driving frequencies between the apical

oxygen phonon (~ 21 THz) and ~ 42 THz, whereas for higher pump frequencies a second resonance emerges, with a strength that follows the increase in pump absorption on the charge transfer resonance (visualized by the equilibrium optical conductivity, $\sigma_1^{equil}(\omega_{pump})$.

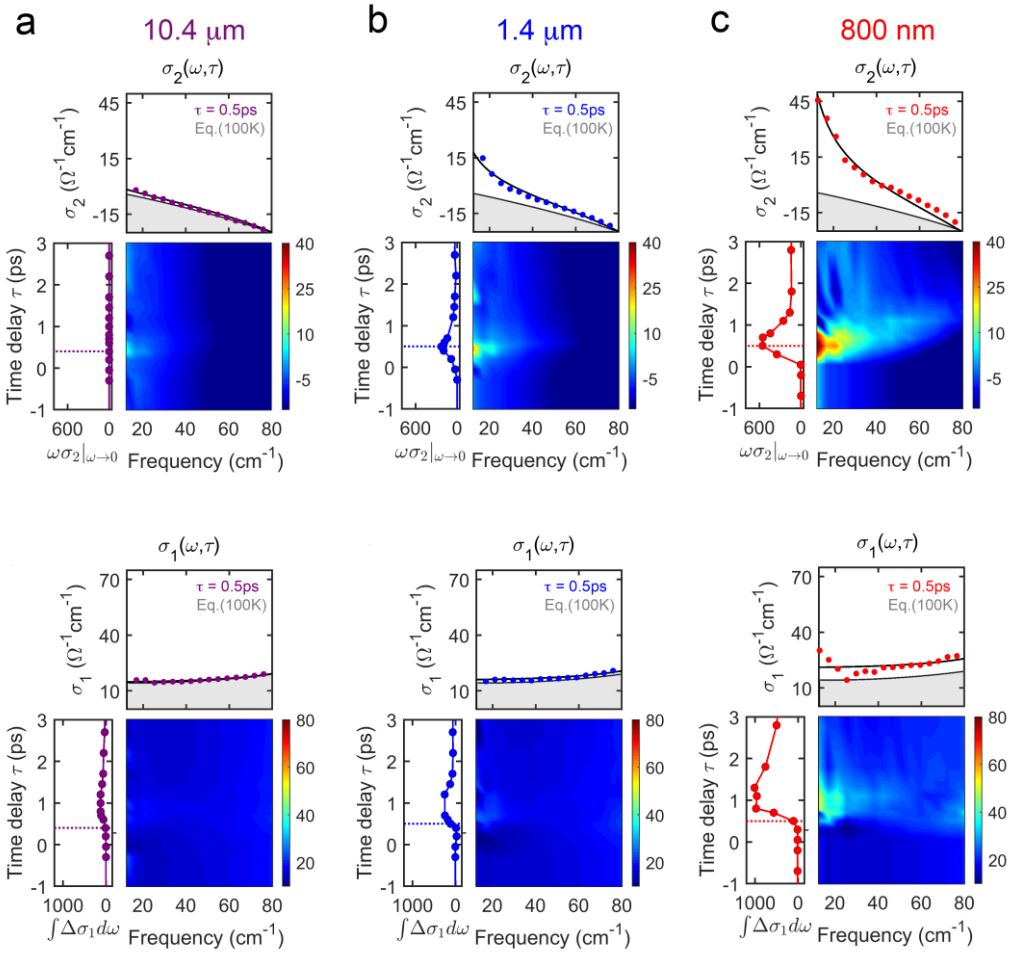

Figure 4.22. (a) Frequency- and time-delay-dependent complex optical conductivity measured at T = 100 K for excitation at 10.4 μm (color plots). Upper panels: corresponding $\sigma_1(\omega)$ and $\sigma_2(\omega)$ line cuts displayed at equilibrium (grey lines) and at the time delay corresponding to the peak of the response (purple circles). Black lines are fits to the transient spectra with a Drude-Lorentz model. Side panels: Frequency-integrated dissipative ($\int\Delta\sigma_1(\omega)d\omega$) and coherent ($\omega\sigma_2(\omega)|_{\omega\to 0}$) responses, as a function of pump-probe time delay. The delay corresponding to the spectra reported in the upper panels is indicated by a dashed line. (**b-c).** Same quantities as in (a)**,** measured for excitation at 1.4 μm and 800 nm.

Note that for these higher frequencies, the reconstruction procedure of the transient optical properties is less reliable than those for the MIR excitations, as the penetration depth mismatch of pump and probe pulses becomes larger. Indeed, at all times, the raw response (optically induced change of the reflected THz probe electric field) is largest at the two phonon resonances involving the motions of apical-oxygen ions. The error bars for high

excitation frequencies (see Figure 4.23(a)) reflect this uncertainty. Nevertheless, error analysis indicates that the appearance of a divergent imaginary conductivity is robust.

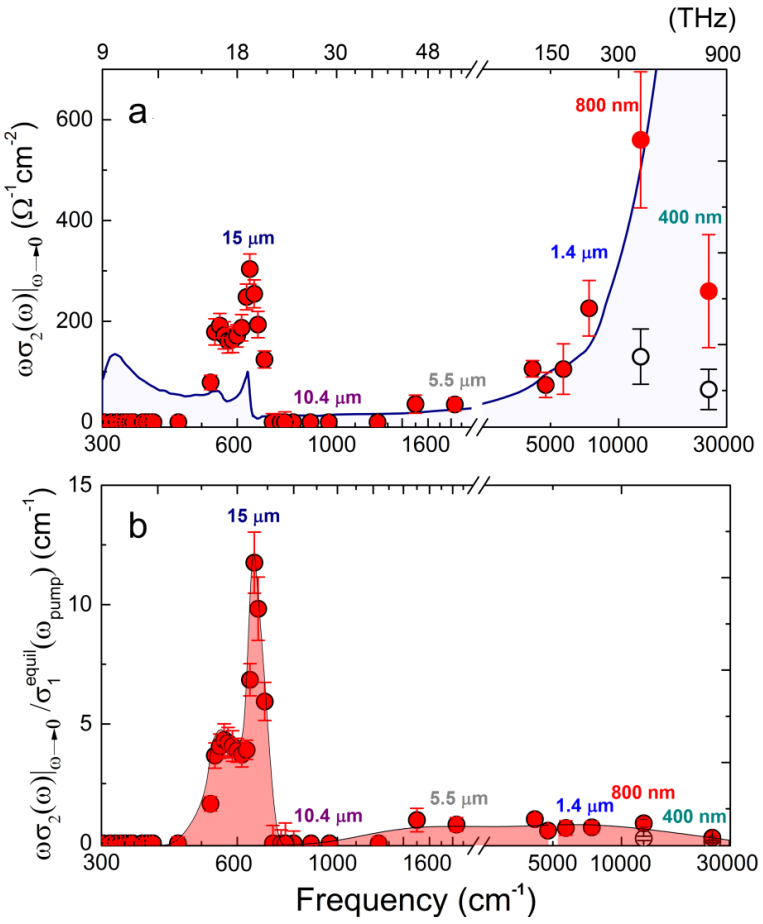

Figure 4.23. (a) Pump frequency dependence of the superconducting response, represented by the low-frequency limit $\omega\sigma_2(\omega)|_{\omega\to 0}$ (red circles). The equilibrium optical conductivity, $\sigma_1^{equil}(\omega_{pump})$, is shown as a blue line. **(b)** Normalized response, $\omega\sigma_2(\omega)|_{\omega\to 0}/\sigma_1^{equil}(\omega_{pump})$ (red circles).

Figure 4.23(b) displays the same data after normalization against the oscillator strength of the material at each pump frequency. The normalized quantity $\omega_{probe}(\omega_{probe})|_{\omega\to 0}$ / $\sigma_1^{equil}(\omega_{pump})$, which takes into account the degree of excitation of the material for a given pump electric field, is taken as a reporter as a wavelegth dependent "photo-susceptibility" of the material.

It is unclear which quantity (the unnormalized or the normalized) is the relevant parameter. The former quantity suggests two resonances of approximately equal strength, the latter quantity shows that for a given coupling, or for a given pump polarization, the effect on the phonon is stronger. The key finding is the second resonance at the charge transfer band

appears to reinforce the notion that changes in the electronic properties of the planes. At the doping level studied here, charge-order melting is not expected to play an important role, as is the case of $YBa_2Cu_3O_{6.6}$ [177] and for $La_{1.875}Ba_{0.125}CuO_4$ [161]. At these frequencies, for the excitation polarized along the *c* axis, we expect a rearrangement of the electronic structure with some qualitative analogy to the direct action of the apical oxygen modes. It is also possible that a similar mechanism to that responsible for the larger resonances at 19.2 and 16.4 THz is at play. We have noted that for the two apical oxygen modes parametric excitation of interlayer fluctuations would be resonant with the sum frequency of the intra and inter bilayer modes. Here, a similar parametric coupling may be at play, without the frequency resonance and hence less efficient. Clearly, further studies that make use of the new pump device available here are needed, with special attention to measurements of time dependent lattice dynamics [10] and inelastic excitations [179][181].

Summary

To summarize, the photo-susceptibility of different IR-active phonon modes in the nonequilibrium superconducting state in $YBCO_{6.5}$ along the *c*-axis was investigated for the first time using narrowband THz pulses delivered by the newly developed optical source. Below T_C, a transient enhancement of the superconducting state longer than 1 ps was induced only by resonant excitations of the apical-O mode in the oxygen-vacant chains at 20 THz. In contrast, depletion of superconducting coherence was observed, when vibrational modes at lower frequency (i.e. “Barium mode ”at 4 THz) were resonantly excited. Then a similar investigation was performed in the normal insulating state at 100 K. A systematic tuning of the excitation wavelength in the far-infrared region (3 - 25 THz) revealed a unique frequency-band in the vicinity of the two apical-O phonons inducing a transient superconducting-like state. The optimum coherence response induced by the THz excitation was comparable to the coherent response in the equilibrium superconducting state at 10 K. The light-induced coherence showed a strong temperature-dependence persisting throughout the pseudogap state, indicating a possible link to pre-existing short-range superconducting fluctuations up to T*.

So far, the light-induced superconducting-like state was associated with a transient rearrangement of the intra- and inter-bilayer distances of the Josephson junctions due to nonlinear couplings between the driven IR-active phonon mode to an A_g Raman-active mode [10]. However, compared with the calculated transient structure changes based on nonlinear phononics, the frequency-dependent photo-susceptibility measurements of the light-induced phase did not show a consistent trend, which questions the previous hypothesis.

Considering the electronic structure changes across the superconducting transition in $YBCO_{6+x}$, the large-amplitude excitations of the apical-O atoms might induce an equivalent charge transfer from the CuO_2 plane to charge reservoir layer, enhancing the electron pairing and Josephson tunneling. To verify this speculation, the transient optical properties induced by electronic excitations with higher driving frequencies (25 - 750 THz) was explored. A second weaker resonance is observed around the charge transfer band edge at ~350 THz above T_C. These observations highlight the importance of coupling from the THz excitations to the electronic structure of the CuO_2 planes, either mediated by a phonon or by charge transfer.

Conclusion and outlook

Resonant excitation of infrared-active vibrational modes using intense THz light pulses has become a powerful tool in controlling the functional properties of strongly correlated electron materials. Insulator-metal transitions as well as the control of ferroelectricity and superconductivity have been demonstrated in this way. So far, however, this approach was restricted to the excitation of phonons with frequencies above 15 THz, limited by the lack of powerful sources at lower THz frequencies.

Vibrational modes of these materials at lower frequencies could have not yet been exploited to manipulate the electronic and magnetic phases and control functional properties. Due to the strong absorption in conventionally used nonlinear optical crystals, there is to date no powerful table-top source that could efficiently excite these vibrational modes to sufficiently large amplitudes.

To overcome these limitations, I developed a table-top source of narrowband THz pulses tunable across the "THz frequency gap". The basic idea of this approach is the difference frequency-mixing of two equally chirped near-infrared pulses in a nonlinear organic crystal DSTMS. The near-infrared pulses were generated as the signal pulses from two home-built optical parametric amplifiers and chirped using pairs of transmission gratings. Pulse energies up to ~7 μJ were achieved in the THz-gap with an overall power conversion efficiency from the fundamental Ti:sapphire amplifier system to the terahertz of ~ 0.1 %. The tunability of this source was extended up to 100 THz with the aid of GaSe or $AgGaS_2$ crystals. Notably, this source can substitute the FEL-based THz source with higher pulse energy and more flexible tunability.

The source was then applied to investigate the possibility of manipulating the superconducting order parameter in the high-T_C cuprate $YBa_2Cu_3O_{6.5}$. Optical excitation induced a few picoseconds short-lived superconducting-like state far above the thermodynamic transition temperature, revealed by time-resolved measurements of the

transient optical properties. To understand the microscopic mechanism underlying this phenomenon, the photo-susceptibility of the light-induced state in $YBa_2Cu_3O_{6.5}$ was measured for many excitation frequencies throughout the entire optical spectrum.

The experimental observations for excitation in the far-infrared region (3 - 25 THz) are summarized as follows. Below the critical temperature T_C, enhanced superconducting coherence was induced when the apical-O mode in the oxygen-vacant chains was excited. In contrast, depletion of the superconducting state was observed by driving the low-frequency vibrational modes, for instance the "Barium mode" at 4 THz. Above T_C, a frequency-band associated with the excitations of apical-O phonons in both the oxygen vacant and filled chains was found to induce a transient superconducting-like state. The light-induced coherence shows a strong temperature dependence, persisting to T^* of the pseudogap phase and therefore indicating a link to the pre-existing short-range superconducting fluctuations.

Transient deformations of the crystal structure, based on the model of nonlinear phononics, were calculated via ab-initio methods, including all the cubic and quartic coupling terms between the resonantly driven infrared-active modes and other phonons. Overall, no direct connection between the calculated transient crystal structures and the emergence of the transient superconductivity was found. Hence, this result suggests that besides anharmonic phonon coupling, which was evidenced earlier in time-resolved x-ray diffraction experiments [22], further mechanisms are likely to be at play when triggering superconductivity in $YBa_2Cu_3O_{6+x}$ with light.

The experiment was then extended to optical excitations between 25 - 750 THz. A second resonance in the susceptibility of the light-induced superconducting state was observed at the edge of this charge transfer band at ~350 THz. The existence of the second resonance indicates that the way light couples to the electronic structure of the CuO_2 planes in order to drive superconductivity is not exclusively mediated by phonons.

However, the nature of the light-induced superconducting state is still ambiguous. It is believed that superconducting fluctuations persist in the pseudogap phase without a long-range coherence. A possible hypothesis for the mechanism of non-equilibrium superconductivity could then be the transient synchronization of the random phases of different Josephson junctions by the applied electric field. It has recently been noted that the frequency of the two apical oxygen phonons matches approximately the sum of the inter- and intra-bilayer Josephson plasma frequencies in $YBa_2Cu_3O_{6.5}$ ($\omega_{JPR,1} \simeq$ 1 - 2 THz and $\omega_{JPR,2} \simeq$ 14 THz, respectively) [195]. Hence, a mechanism in which driven lattice excitations couple to the in-plane electronic structure may become resonantly enhanced at these frequencies

[173]-[176]. To gain deeper understanding of the nonequilibrium process, further studies based on the new pump device are needed, with special attention to measurements of time-dependent lattice dynamics [10] and inelastic excitations [179]-[181].

In general, the experiments discussed in this thesis demonstrate the capability of the newly developed source in controlling superconductivity in high-T_C cuprates. This source paves the way for research on a broader class of quantum materials. Recent findings of a nonequilibrium superconducting phase in potassium-doped fullerides were proposed to be associated with the symmetry-breaking following the resonant excitation of a C_{60} vibrational mode [197]. The phenomenon was observed in a broad frequency range coinciding with the electronic absorption band, which supports another scenario of electron cooling mechanism by the optical excitations [198]. Making use of the present source, a systematic pump-frequency dependent measurement across the broad electronic absorption band would provide new insight into this effect. Moreover, by exploiting the accessible bandwidth of the powerful THz source, the low-energy excitations in the unconventional iron-based superconductors could also be exploited to manipulate the interplay between superconductivity and the competing electronic and magnetic orderings [199][200].

APPENDICES

APPENDIX A

A. Detection methods of THz transients

The detection methods for THz detection used in this work, such as electro-optic sampling (EOS), Fourier-transformation-IR-spectroscopy (FTIR) will be briefly introduced in this appendix.

Electro-optic sampling

Electro-optic (EO) sampling is a delicate detection technique in measuring the electric field profile of a THz transient. The THz pulse induces a transient birefringence in the detection crystal, which is linearly proportional to the electric field. This birefringence can be measured by the polarization rotation of the gating pulse. The schematic drawing of typical EO sampling and two typical descriptions of the induced birefringence are depicted in Figure A.1. The gating pulse is spatially and temporally overlapped with the THz transient, and decomposed in two orthogonal polarization components after interacting with the THz field in the EO crystal. Afterward, the THz-induced birefringence is detected with balanced photodiodes.

The EO sampling process in the non-inversion-symmetric nonlinear crystal can be understood as a Pockels effect. It describes the modulation of the refractive index in the material by an applied electric field given by

$$\Delta n = n_0^3 * r_{eff} * E \tag{A.1}$$

with n_0 the static refractive index, r_{eff} the effective electro-optic tensor, and E the THz field strength. Pockels effect is a linear EO effect, so that the THz field can be instantaneously reconstructed by monitoring the birefringence (Figure A.1(b)). On the other hand, EO sampling can also be understood as a frequency mixing process. Figure A.1(c) shows the spectra of sum and difference frequency fields (green) with a large overlap with the probe spectrum (red). The polarization state of each frequency component is generally elliptically-polarized and can be expressed as the sum and difference frequency fields [183].

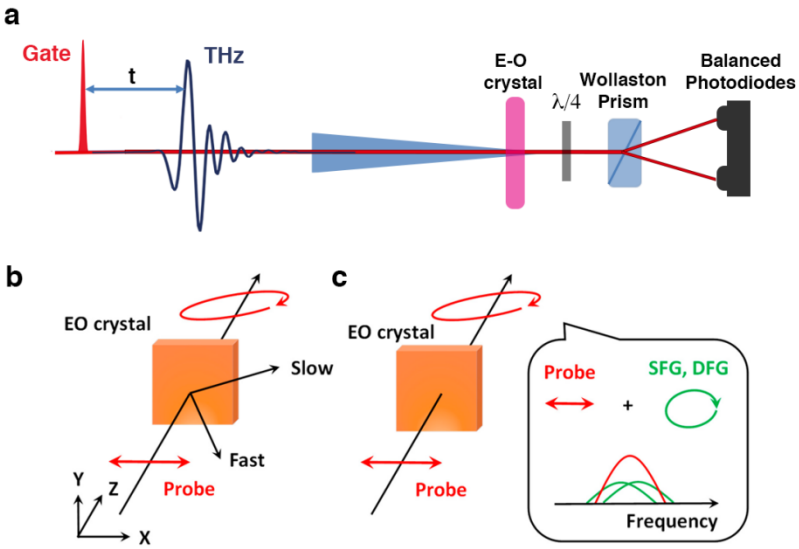

Figure A.1. (a) Schematic illustration of Electro-optic sampling. **(b-c)** Two different description of the birefringence in the Electro-optic sampling: **(b)** Pockels effect description and **(c)** frequency-mixing description. EO: electro-optic, SFG: sum frequency generation, DFG: difference frequency generation**.** (b-c) are adapted from Ref. [183]

To improve the sampling process, appropriate EO crystals with modest thickness and dry atmosphere are required. Nonlinear crystals such as inorganic compounds ZnTe, GaP, GaSe, GaAs, and organic compounds DAST, DSTMS can be good candidates for sampling different THz pulses. For instance, a (110) cut ZnTe with a thickness of 500 μm is used for the EO sampling of the broadband THz probe pulses in the pump-probe measurement, which supports broad detection bandwidth. However, due to the phonon absorption line (lowest at 4.3 THz) in ZnTe crystal, the detection bandwidth is limited. If a broader detection range is needed, GaP crystal can be used with good phase-matching conditions up to 7 THz. The THz transients generated with organic crystals above 7 THz can be sampled a thin GaSe (< 100 μm) crystals in a purging box with clean nitrogen.

Fourier-transformation-IR-spectroscopy

THz pulses can also be characterized in the frequency domain by using Fourier-transformation-IR-spectroscopy (FTIR). A simple schematic description of the FTIR setup used in the experiment is shown in Figure A.2(a). The incoming THz beam is separated into two arms by a beam splitter and combined again on the same beam splitter. Motorized stage is used to continuously controlled to temporally overlap the recombined THz beams on the detector for interferogram measurement. The interferogram recorded via FTIR measurement plays an important role in determining the frequency information for the generated THz pulses.

A sensitive detector is the key part of the FTIR measurement. Conventional detector like MCT Bolometer (Mercury Cadmium Telluride, HgCdTe) has been the only choice for decades in sensitive FTIR devices. It has many drawbacks, for example, big dimension, cryogenic cooling for low noise, and limited detection frequency range typically within 3-5 μm and 8-12 μm. On the other hand, a Golay Cell is a ”photo-acoustic” device that is sensitive in a broad spectral response, which has been widely used for THz detection. A THz beam transmits heats the thin metallic film and the gas in the gas cell distorts the mirrored back wall, which is measured by a photodiode. Golay Cell is slightly more sensitive, with a large sensing area and a fixed window, however, it has a slow response time, big dimension and requires AC voltage for operation.

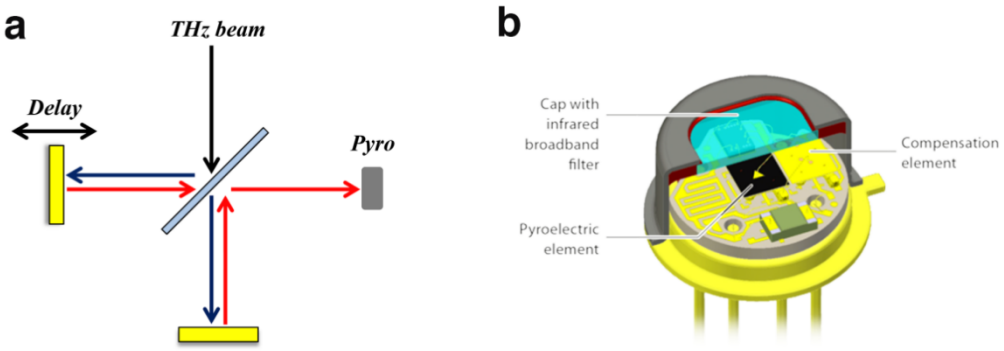

Figure A.2. (a) Schematic description of Fourier-transformation-IR-spectroscopy (FTIR). **(b)** Pyroelectric detector from InfraTec.

A pyroelectric detector is based on a thin, permanently poled, ferroelectric crystal (i.e. $LiTaO_3$) that exhibits a pronounced pyroelectric effect. The instantaneous polarization is a function of the rate of temperature change in the crystal. By applying conductive electrodes to the top and bottom surfaces of the crystal, the resulting charge can be coupled out of the

device and calibrated. It can be operated at room temperature with a broad spectral response covering most of the electromagnetic spectrum, including the THz region. It is sensitive, inherently fast and compact, which is recently popular in THz detection.

In this thesis, electro-optic sampling and FTIR are frequently used for the characterizations of the generated narrowband THz pump pulses and broadband probe pulses. In general, there are also other techniques which could be used for dedicated detection in the THz frequency range, such as Photoconductive antenna detection and THz-lensing detection.

APPENDIX B

B. Application of narrowband pulses in THz spectroscopy

The novel narrowband THz source discussed in Chapter 2 has been exploited in the THz spectroscopy to investigate the nonequilibrium physical properties of condensed matters, especially light-induced superconductivity. Figure B.1 schematically shows the narrowband THz pump / THz probe setup. Single-cycle THz probe pulses with spectral components between 10 cm^{-1} and 80 cm^{-1} were generated via optical rectification of pulses at the fundamental 800 nm wavelength in a ZnTe crystal. The THz electric field of the probe pulses reflected from the sample surface was detected via electro-optic sampling in another optically contacted ZnTe crystal.

For the generation of narrowband pulses with relative bandwidth $\Delta\nu/\nu < 10\%$, the two signal outputs were linearly chirped to a pulse duration of > 600 fs before the DFG process in either a 0.5-mm thick DSTMS organic crystal or the same 1-mm GaSe crystal. The pulse energies achieved were always at the few-μJ level. To achieve good spatial overlap between the narrowband pump beam and the broadband THz probe beam, the pump beam is first collimated and focused by a 2-inch parabolic gold mirror with an effective focus length of 75 mm. The beam size of the THz probe beam is ~ 400 μm (frequency integrated), whilst the pump spot size can be adjusted by moving the focus plane via a motorized stage beneath the parabola. The highest pump fluence can be achieved up to 10 mJ/cm^2 and the corresponding pump electric field will be > 2 MV/cm. The THz pulses could be attenuated by inserting a pair of free-standing wire grid polarizers.

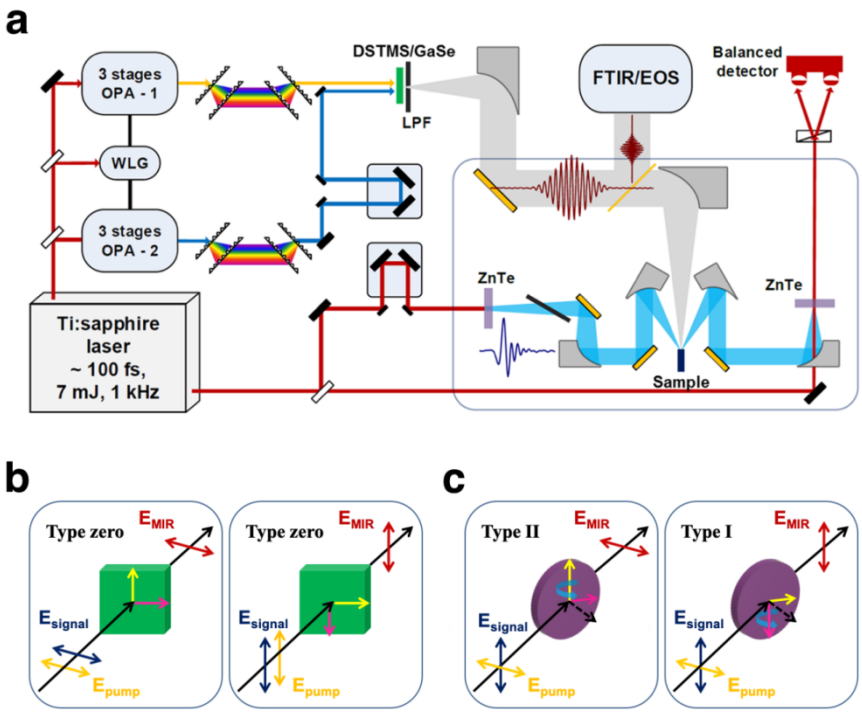

Figure B.1. (a) Narrowband THz pump / THz probe setup. OPA, optical parametric amplifier. WLG, white light generation. LPF, long-pass filter. Two near-infrared signal outputs from two parallel OPAs were linearly chirped and sent to a nonlinear crystal (DSTMS/GaSe) for difference frequency generation (DFG). The generated pump pulses were separated from the near-infrared inputs and characterized by either Fourier-transform spectroscopy (FTIR) or electro-optic sampling (EOS). The transient optical properties were measured by detecting the THz electric field generated from a ZnTe crystal via optical rectification and reflected from the sample surface, as a function of pump-probe time delay. **(b-c)** Phase-matching condition and DFG process for MIR-THz light polarized in horizontal (left) and vertical (right) plane in DSTMS **(b)** and GaSe **(c)** crystal.

The two chirped pulses will be sent to nonlinear crystal for DFG. We use organic crystal DSTMS for the narrowband generation between 3 and 15 THz and GaSe crystal for higher frequencies. However, in GaSe, the perfect phase-matching condition can be achieved in a broad spectrum range from 15 to 30 THz. This combination allows us to generation intense narrowband pulses tunable across 3 to 30 THz. The phase-matching is slightly different in two cases. Figure B.1(b-c) depicts the phase-matching condition for DSTMS and GaSe. For example, if horizontally polarized light is needed, the crystal a-axis of DSTMS and the polarization of both the pump and signal should be in horizontal plane, which is type-zero phase-matching. In the case of GaSe, the pump and signal beam should be cross-polarized. To rotate the polarization by 90 degrees, the pump, signal and DSTMS crystal should all be rotated 90 degrees, while only the GaSe crystal needs to rotated to switch from type II to type I phase-matching for higher frequencies.

The frequency tunability of the narrowband source is extended by mixing the two NIR beams in a 1-mm GaSe crystal. By fine-tuning the time delay between the interacting stretched NIR pulses is depicted in Figure B.2. Fine-tuning of the central frequency can be realized by varying the frequency difference between the two interacting in GaSe.

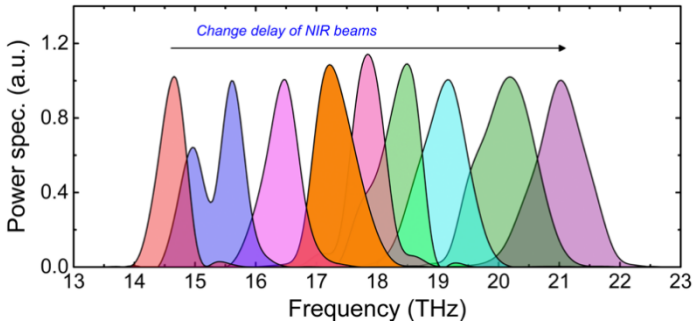

Figure B.2 Power spectrum of the generated MIR pulses using GaSe crystal.

A schematic explanation of the Narrowband pump / THz probe experimental setup is illustrated in Figure B.3(a). There are two time-delays t and τ, the former is the delay between the sampling pulse and the THz pulse, mapping out the THz spectrum, whilst the latter refers to the delay between the sampling pulse and pump beam and reflects the time after excitation of the sample. The setup of the pump generation is built in a purging box filled with clean nitrogen gas, in order to get rid of the vapor absorption of the THz beam. One motorized translation stage is applied to introduce delay τ between the pump and probe beams, while a second stage for only the sampling pulses to control the delay t.

The stationary probe electric field $E_R(t)$ and the differential electric field $\Delta E_R(t,\tau)$ reflected from the sample were recorded simultaneously by feeding the electro-optic sampling signal into two lock-in amplifiers and mechanically chopping the pump and probe beams at different frequencies of ~357 and 500 Hz, respectively. The differential signal $\Delta E_R(t,\tau)$ was sampled at the ~143 Hz difference frequency of the two choppers. This approach minimized the cross-talk between the two detected signals whilst reducing the noise level of the measurements [106].

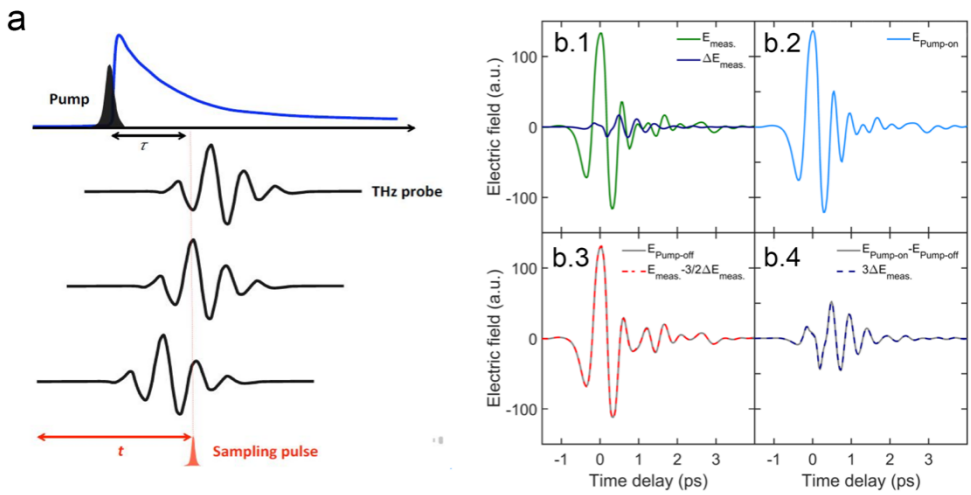

Figure B.3 (a) Measurement of the time- and frequency-dependent THz response at a single time delay τ during the material dynamics. The ultrafast response at each time delay τ is recorded by fixing the delay between the pump pulse and sampling pulse and by scanning the THz transient across it (varying the delay t). **(b)** Calibration measurement for the reconstruction of the stationary and differential electric field of probe pulses. **(b.1)** The measured signals from the lock-in amplifiers $E_{meas.}(t)$ and $\Delta E_{meas.}(t,\tau)$. **(b.2)** The light-induced electric field $E_R^{pump-on}(t,\tau)$ with the pump beam always on. **(b.3)** Stationary electric field $E_R(t)$ ($E_R^{pump-off}(t,\tau)$) and the reconstructed signal $E_{meas.}(t) -$ (3/2) $\Delta E_{meas.}(t,\tau)$ from the measurement. **(b.4)** Differential electric field $\Delta E_R(t,\tau)$ and the reconstructed signal $3\Delta E_{meas.}(t,\tau)$ from the measurement. $E_R(t)$ and $\Delta E_R(t,\tau)$ can be perfectly reconstructed.

The stationary field $E_R(t)$ is measured by chopping the probe beam at 500 Hz and blocking the pump beam. Then the light-induced reflectance $E_R^{pump-on}(t,\tau)$ is measured by keeping the pump beam always on. The differential electric field $\Delta E_R(t,\tau)$ was achieved as $E_R^{pump-on}(t,\tau)$ - $E_R(t)$. Then we chopped the pump and probe beams with one chopper at different frequencies and get the measured signals $E_{meas.}(t,\tau)$ and $\Delta E_{meas.}(t,\tau)$. The calibration we use is obtained as follows:

$$E_R(t,\tau) = E_{meas.}(t,\tau) - (3/2)\Delta E_{meas.}(t,\tau); \quad \text{(B.1)}$$

$$\Delta E_R(t,\tau) = 3\Delta E_{meas.}(t,\tau). \quad \text{(B.2)}$$

As can be seen in Figure B.3(b.3-b.4), the stationary electric field and the light-induced change of the probe pulses are perfectly reconstructed using the calibration method.

APPENDIX C

C. Simulations for the narrowband measurements on $YBCO_{6.5}$

C.1 Ab-initio calculations of the structural dynamics

In this section, the optically-driven rearrangement of the crystal structure will be reported by combining effective Hamiltonian modeling with first-principle computations. The content in this subsection is taken from the Ref. [35]. This approach is based on an anharmonic crystal potential that consists of three distinct contributions [21][184][185]:

1. The harmonic potential of each phonon mode

$$V_{harm} = \sum \frac{\omega_i^2}{2} Q_i^2, \tag{C.1}$$

with ω_i and Q_i representing the eigenfrequency and coordinate of the i-th mode, respectively.

2. The anharmonic potential containing higher-order terms of the phonon coordinates and combinations of different phonon modes

$$V_{anharm} = \sum g_{ijk} Q_i Q_j Q_k + \sum f_{iklm} Q_i Q_k Q_l Q_m, \tag{C.2}$$

with g_{ijk} and f_{iklm} indicating third and fourth order anharmonic coefficients, respectively.

3. The coupling of each individual phonon mode to an external electric field

$$V_{efield} = \sum Z_i^* Q_i E_{field} \,, \tag{C.3}$$

with Z_i^* representing the mode effective charge [27][186].

The structural dynamics are then determined by the equations of motion for each phonon mode, given by

$$\ddot{Q}_i + 2\gamma_i \dot{Q}_i + \nabla_{Q_i}\left(V_{harm} + V_{anharm} + V_{efield}\right) = 0. \tag{C.4}$$

Here, we introduced a phenomenological damping term γ_i, which accounts for contributions to the finite lifetime which are not already considered within the anharmonic potential. Importantly, the equations are restricted to phonon modes at the Brillouin zone center, due to the long wavelengths of the THz excitation pulses.

Various studies have shown that this approach can describe the structural dynamics induced by the resonant excitation of infrared-active modes in a solid [10][14]. However, only a small subset of all possible phonon coupling constants was considered in these cases, predominantly due to computational limitations. In the present simulations, this reduction was overcome by utilizing the approaches given in Refs. [184][187]. We list all technical and numerical details at the end of this Section.

We simulated the THz-driven structural dynamics of the ortho-II structure of $YBa_2Cu_3O_{6.5}$, which exhibits 73 non-translational phonon modes at the Brillouin zone center. The most relevant phonon modes for *c*-axis polarized THz excitation are 13 B_{1u} modes, which exhibit a finite electric dipolar moment along this direction. In addition, there are 11 A_g modes, which fulfill the symmetry requirements to exhibit a finite third-order type coupling to the B_{1u} modes [10][184]. A full list of the eigenfrequencies of these modes is presented at the end of this Section.

The calculated effective charges for the B_{1u} modes, needed to describe their excitation by a THz electric field according to Eq. (c.3), are shown in Figure C.1(a). We assumed here that the Born effective charge of each atom equals its ionic charge. In agreement with experimental observations [33], we obtain large values for the two highest-frequency apical-O modes at 16.5 THz and 20.5 THz, for the 10-THz mode affecting the CuO_2 layers, and for the

mode at 4 THz that involves Ba displacements. Note also that all phonon frequencies match within a few percent the values determined from the experiment.

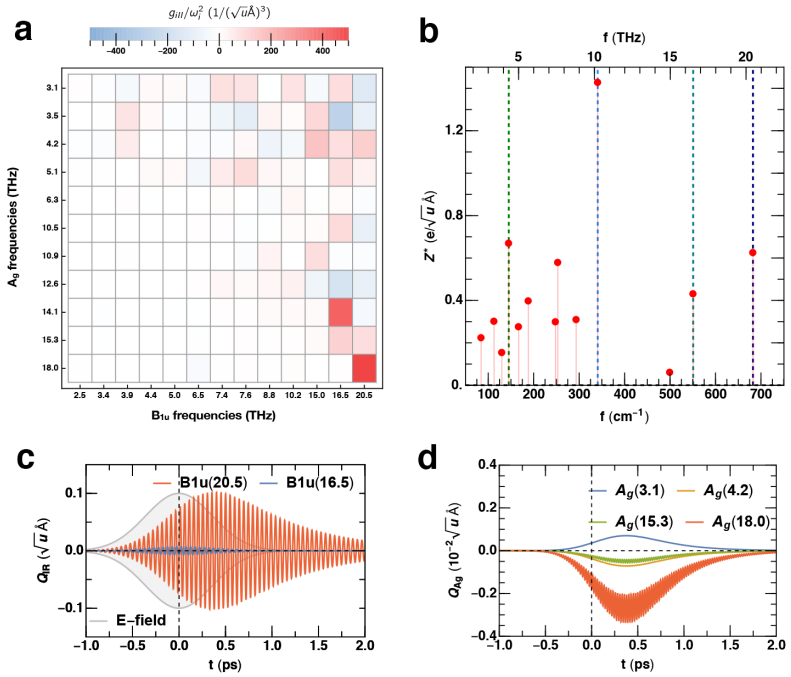

Figure C.1. (a) Third-order anharmonic coupling coefficients of the type $Q_{Ag}Q_{IR}^2$ for all B_{1u} and A_g modes. **(b)** Mode effective charges for the polar B_{1u} modes of the $YBa_2Cu_3O_{6.5}$ ortho-II structure. **(c)** Oscillations of two B_{1u} modes at 16.5 and 20.5 THz driven by a narrowband THz pulse at 20.5 THz (grey area). **(d)** Dynamics of the four A_g modes exhibiting stronger coupling to the 20.5-THz B_{1u} mode driven in (c).

Group symmetry dictates three sets of third-order couplings for the phonon modes considered. The first is the coupling of the square of the optically-excited B_{1u} modes to a single A_{1g} mode, proportional to $Q_{IR,i}^2 Q_{Ag}$. The second is the coupling of two different B_{1u} modes to a single A_{1g} mode ($Q_{IR,i}Q_{IR,j}Q_{Ag}$), and the third is the coupling between three A_{1g} modes ($Q_{Ag,i}Q_{Ag,j}Q_{Ag,k}$). For the fourth-order coupling terms, we only considered the terms of the form Q_i^4 and neglected expressions mixing two or more phonon modes. Thus, we took into account, in total, 1067 third-order and 24 fourth-order coupling coefficients. Note that, in the earlier studies of Refs. [10] [184], at maximum 24 coupling coefficients were considered. As an example, Figure C.1(b) shows a subset of the computed anharmonic coupling coefficients, representing the two-mode coupling of the type $Q_{IR,i}^2 Q_{Ag}$. Both the two highest-frequency B_{1u} polar modes couple strongly to two different A_{1g} modes, similar to the observations reported for $YBa_2Cu_3O_7$ in Ref. [184].

Figure C.1(c-d) show the dynamics of two selected B_{1u} modes and four anharmonically coupled A_g modes. The time traces have been triggered by an electric field pulse $E(t) =$

$e^{\frac{2t^2 ln(2)}{FWHM^2}} cos(\omega t)$ with a 3 MV/cm peak field and 0.6 ps pulse duration (FWHM) at 20.5 THz. The resonantly excited 20.5-THz B_{1u} mode oscillates with an amplitude that is about one order of magnitude larger than that of the off-resonant B_{1u} mode at 16.5 THz. The dominant A_g modes, anharmonically coupled to the B_{1u} phonons, are transiently displaced from their equilibrium positions with significant amplitudes ($|Q_{Ag}| < 10^{-5}\sqrt{u}$Å). They reach their maximum displacements at about 0.4 ps time delay, for which also the resonantly driven 20.5-THz B_{1u} mode reaches its peak amplitude.

C.2 Numerical approach for the ab-initio calculations

We employed first-principles total energy calculations in the framework of the density functional theory (DFT) to compute all harmonic and anharmonic terms included in the equations (C.1), (C.2), and (C.3). This part is taken from Ref.[35]. Specifically, we used the implantation of DFT, applying the linearized augmented-plane wave method (LAPW) within the ELK-code [189]. We approximated the exchange-correlation functional by the local density approximation. In addition, we performed careful tests of all relevant numerical parameters entering the computation. The setting for well-converged results corresponded to a truncation at l_{max} = 10 of the angular expansion of wave functions and potential within the muffin-tin radii (2.6, 2.8, 1.85 and 1.4 a.u. for Y, Ba, Cu, and O, respectively). A $|G|_{max}$=20 a.u.$^{-1}$ limited the potential and density expansion within the interstitial region. We set $R_{MT} \times k_{max}$=8.0 for truncating the plane-wave wavefunction expansion. The Brillouin zone was sampled within our computations by a 11×19×5 k-point mesh. The same configuration was also employed in a previous study [196] and, within this setting, the forces (most relevant for phonons and anharmonic terms) were made to converge by less than 0.1 meV/Å.

Before computing the coefficients of the anharmonic potential, we first structurally relaxed the unit cell of $YBa_2Cu_3O_{6.5}$, for which we considered the ortho-II structure, following previous studies and the experimental setting [196]. As lowest energy state, we obtained the atomic configuration given in Table C.1.

The phonon eigensystem was computed by frozen-phonon calculation using symmetry-adapted distortions generated with the Phonopy package [190]. We list all modes at the zone center in Table C.2. Next, we applied the prescription in Ref. [15] to calculate the anharmonic constants of third order and took the approach of Ref. [184] for the quartic order terms. We computed the mode-effective charges appearing in equation (4.4) by using the nominal

averaged ionic charges of each atom as Born charges. Explicitly, we have for Yttrium 3+, Barium 2+, Copper 2+ and Oxygen 2-.

Table C.1. DFT minimized structural configuration of the $YBa_2Cu_3O_{6.5}$ ortho-II cell with $a = 7.55$ Å, $b = 3.81$ Å, and $c = 11.50$ Å.

element	Wykoff position	*x*	*z*	element	Wykoff position	*x*	*z*
Y	l	0.251	0.500	O1	e	0.000	0.000
Ba	x	0.244	0.187	O2	w	0.250	0.378
Cu1	a	0.000	0.000	O3	r	0.000	0.378
Cu2	b	0.500	0.000	O4	t	0.500	0.378
Cu3	q	0.000	0.356	O5	q	0.000	0.161
Cu4	s	0.500	0.355	O6	s	0.500	0.153

Table C.2. Computed DFT eigenfrequencies of the phonon modes at the center of the Brillouin zone for the $YBa_2Cu_3O_{6.5}$ ortho-II structure.

Label	f (THz)	Label	f (THz)	Label	f (THz)	Label	f (THz)
A_g	3.1	B_{1u}	7.4	B_{2u}	17.0	B_{3u}	8.1
A_g	3.5	B_{1u}	7.6	B_{2u}	17.4	B_{3u}	8.4
A_g	4.2	B_{1u}	8.8	B_{2g}	1.8	B_{3u}	10.3
A_g	5.1	B_{1u}	10.2	B_{2g}	2.6	B_{3u}	10.5
A_g	6.3	B_{1u}	15.0	B_{2g}	4.1	B_{3u}	11.8
A_g	10.5	B_{1u}	16.5	B_{2g}	4.2	B_{3u}	13.4
A_g	10.9	B_{1u}	20.5	B_{2g}	6.5	B_{3u}	18.3
A_g	12.6	B_{1g}	2.9	B_{2g}	7.4	B_{3g}	2.0
A_g	14.1	B_{1g}	3.8	B_{2g}	8.7	B_{3g}	4.1
A_g	15.3	B_{1g}	9.7	B_{2g}	10.0	B_{3g}	5.4
A_g	18.0	B_{2u}	2.4	B_{2g}	11.3	B_{3g}	6.5
A_u	2.8	B_{2u}	3.6	B_{2g}	11.4	B_{3g}	10.3
A_u	10.8	B_{2u}	4.7	B_{2g}	18.1	B_{3g}	11.1
B_{1u}	2.5	B_{2u}	5.2	B_{3u}	2.5	B_{3g}	16.6
B_{1u}	3.4	B_{2u}	5.6	B_{3u}	2.9	B_{3g}	17.2
B_{1u}	3.9	B_{2u}	8.0	B_{3u}	3.7		
B_{1u}	4.4	B_{2u}	10.3	B_{3u}	3.8		
B_{1u}	5.0	B_{2u}	11.5	B_{3u}	4.7		
B_{1u}	5.6	B_{2u}	16.6	B_{3u}	5.4		

C.3 Phonon excitation with narrowband pulses

The optical properties can be fitted by treating the optical phonons as Lorentz oscillators, the complex dielectric function can be described as

$$\tilde{\varepsilon}(\omega) = \sum_i \frac{s_i^2}{(\Omega_i^2 - \omega^2) - i\omega\Gamma_i} \tag{C.5}$$

where, Ω_i, S_i, and Γ_i denote the central frequency, strength, and damping coefficient of the i-th oscillator, respectively. If an optical phonon is driven by ultrashort THz pulses in the form of

$$E(\omega_p, t) = E_0 \, exp\left(-\frac{2\,log(2)t^2}{\tau^2}\right) cos(\omega_p t), \tag{C.6}$$

the dynamics of the coordinate Q_{IR} for the driven phonon is given by the equation of motion

$$\ddot{Q}_{IR} + 2\gamma_{IR}\dot{Q}_{IR} + \omega_{IR}^2 Q_{IR} = f(t) \tag{C.7}$$

where Q_{IR}, ω_{IR} and γ_{IR} correspond to the coordinate, frequency and damping coefficient of the oscillator, respectively.

It is significant to investigate the dynamics of the driven oscillator with various parameters of the driving field. By tailoring the pump pulses, the light-induced effect could be enhanced which is usually proportional to the maximum displacement of the driven mode. Conceptually, the stronger the pump electric field is, the lager the amplitude the phonon can be driven. However, it is evident in the following simulation that, the phonon coordinate will be driven to even larger amplitude if the mode is driven by suitable narrowband pulses.

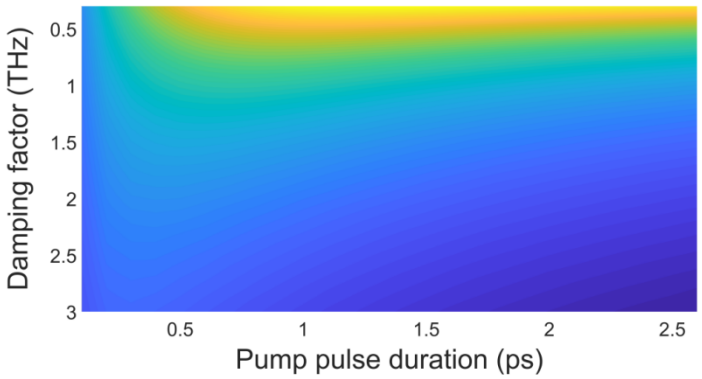

Figure C.2 The maximum amplitude of the investigated oscillator as a function of the damping coefficient and pump pulse duration. The phonon frequency is set be to 19.2 THz. The pump pulses are set to be transform-limited.

Figure C.2 illustrates the simulated maximum amplitude of the driven oscillator as a function of pump pulse duration and the damping factor. The pump pulses are set to be transform-limited with the same pulse energy. If the phonon is underdamped, for example, with a damping factor less than 1 THz, the maximum amplitude will be reached with the pump pulses longer than 500 fs. In this case, the oscillator can be continuously driven by the incident electric field to large-amplitude. In contrast, in the overdamped regime, the optimum

pump pulse duration is decreased to below 400 fs. In this case, the peak electric field at each period of the light will matter.

Here, I specify the phonon to be the apical-O mode in the O-deficient chains. Figure C.3(a) shows the atomic motions projected in the *ac*-plane. The displacement of the oxygen ions in the oxygen-vacant chains will transiently modify the electronic properties in the CuO_2 planes, which results in a better coherent state along the *c*-axis. Figure C.3(b) shows the simulated of the maximum amplitude resonantly pumped by THz pulses with different durations. The damping coefficient is set to be 1 THz, which is extracted from the linewidth of the phonon [33]. The optimum pulse duration is around 600 fs for this specific mode.

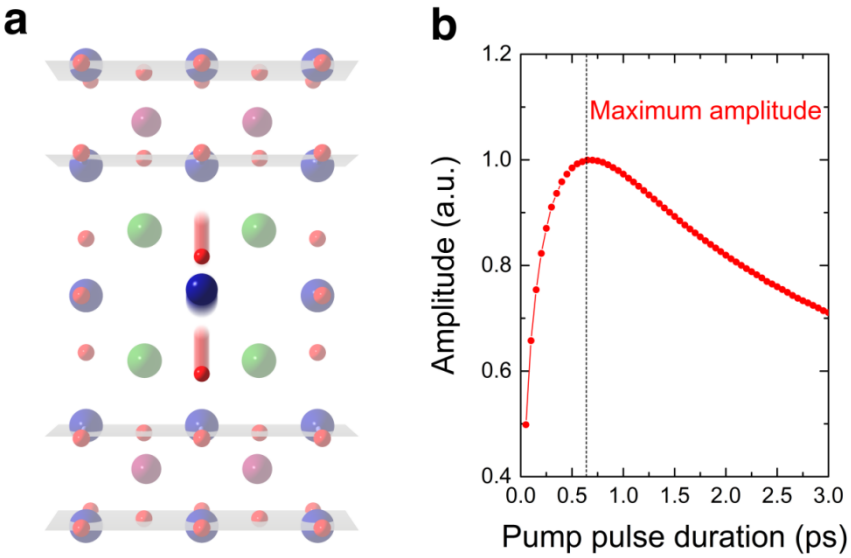

Figure C.3. (a) Atomic motion of the apical-oxygen mode in the O-deficient chain at 19.2 THz of $YBCO_{6.5}$ projected in ac-plane with CuO_2 layers highlighted in grey. **(b)** The simulated maximum amplitude of 19.2-THz mode by transform-limited MIR pulses with different pulse durations. The damping coefficient is extracted from the linewidth of the phonon. The dashed line indicates the best pulse duration of around 600 fs.

Figure C.4 depicts the solution of the equation of motion of the 19.2-THz mode along with the coordinates of the driven IR-active mode for both cases with damping extracted from the linewidth of the phonon. In frequency domain (Figure C.4(a)), the spectrum of the pump of 150 fs (broadband) and 600 fs (narrowband) is depicted together with the real part of conductivity at normal state (100 K). The amplitude of the 19.2-THz mode driven by 150 fs (upper) and 600 fs (lower) pump pulses with the same pulse energy. The narrowband pulses with 600 fs duration are efficient in exciting the 19.2-THz mode in $YBCO_{6.5}$.

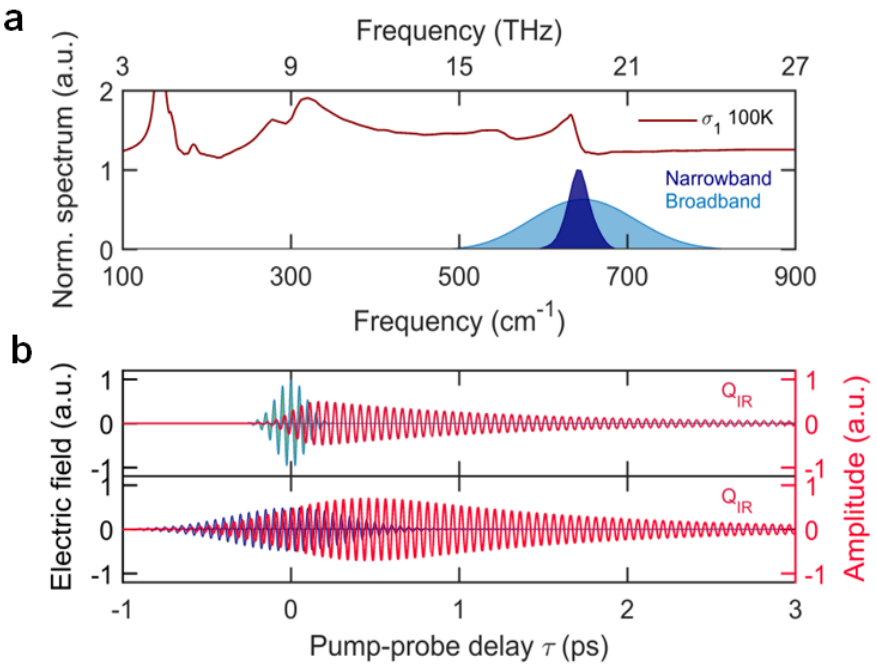

Figure C.4. (a) Equilibrium *c*-axis optical conductivity, $\sigma_1(\omega)$, of $YB_2Cu_3O_{6.5}$ at 100 K ($T > T_C$, red solid line), along with the frequency spectra of THz probe (grey), broadband pump (light blue), and 19.2 THz narrowband pump (dark blue) pulses. **(b)** The amplitude of the 19.2-THz mode driven by 150 fs (upper) and 600 fs (lower) pump pulses with the same pulse energy.

C.4 Estimation of pump-induced heat

Compared with near-IR excitation, the ultrafast dynamics can be investigated selectively with much lower heating effect and longer coherence time by applying THz light fields. However, when large-amplitude excitation takes place, the change of effective lattice temperature must be considered due to the relatively high pump fluence. Adapting the two-temperature model described in Ref. [164], final lattice temperature can be estimated after electron-phonon thermalization which occurred in a short period (~ 1 ps). The absorbed energy in the excited volume under certain pump fluence will result in a temperature increase, which is dominated by the heat capacity of the investigated material. This relation can be expressed as

$$Q_{pump} = \int_{T_i}^{T_f} N * C_S(T) dT \tag{C.8}$$

Here, Q_{pump} is the total energy absorbed from the pump pulse, N is the number of moles in the excited volume, T_i is the initial temperature and T_f is the final temperature after electron-phonon thermalization. Further, the heat capacity in $YBCO_{6+x}$ can be written as

$$C_S(T) = \gamma T + \beta T^3 \tag{C.9}$$

The value for $YBCO_{6.5}$ has been given by Ref. [201] with $\gamma \sim 2.3$ mJ mol^{-1} K^{-2} and $\beta \sim 0.394$ mJ mol^{-1} K^{-4}. The energy deposited in the material can be calculated as $Q_{pump} = F^*A(1\text{-}R)$, where F is the pump fluence, A is the area of the pump beam on the sample using the FWHM (~ 0.4 mm) as the diameter, and R is the reflectivity at 19.2 THz is ~ 0.35. The excited volume is estimated as a cylindrical disk with a diameter of 0.4 mm and height equal to the penetration depth (~ 0.7 μm for 19.2 THz).

The final temperature T_f is calculated numerically and plotted versus pump fluence in Figure C.5. The dashed line indicates Tc at 52 K. For an initial temperature T_i = 10 K below T_C (red curve), the pump beam with 8 mJ/cm^2 will heat the excited volume up to ~100 K. Interestingly, with higher than 1 mJ/cm^2 pump fluence, the system will be transferred into normal state due to thermalization. This estimation is consistent with the experiment results at 10 K, which manifested a strong suppression of the superconducting state after 1 ps. When the measurement was conducted at 100 K above T_C, the temperature increase is marginal.

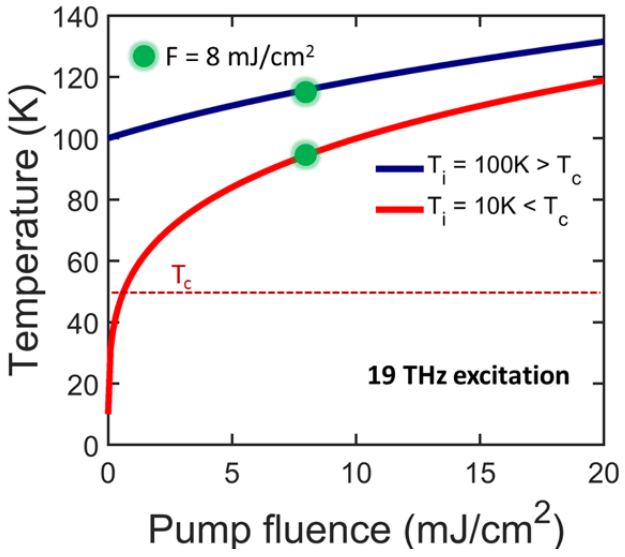

Figure C.5. Calculated final lattice temperature after electron-phonon thermalization as a function of pump fluence after 19 THz excitation in $YBCO_{6.5}$. The red curve and blue curve are corresponding to different initial temperature at 10 K (superconducting) and 100 K (insulating), respectively. The red dashed line is superconducting transition temperature Tc at 52 K.

APPENDIX D

D. Uncertainties in determining the transient optical properties

Different sources of uncertainty and their propagation in the data analysis will be discussed. Data set measured at T = 100 K for narrowband excitation at 19.2 THz will be examined.

Static optical properties

First of all, the propagation of the uncertainty in equilibrium optical properties is taken into account. According to the Kramer-Krönig relation, each optical constant can be reconstructed given just one of these coefficients. Usually, the static optical constants are determined by the measurement of reflectivity. The uncertainty of the reflectivity measurement will result in uncertainty in other optical constants and propagate into the light-induced optical properties based on these static optical constants.

Figure D.1 shows different sets of static optical properties with ± 5% and ± 10% statistic errors in Reflectivity for $YBCO_{6.5}$ at 100 K. Deviations in the real and imaginary part of the static optical conductivity are inherited from the uncertainty of the Reflectivity, depicted with different transparence.

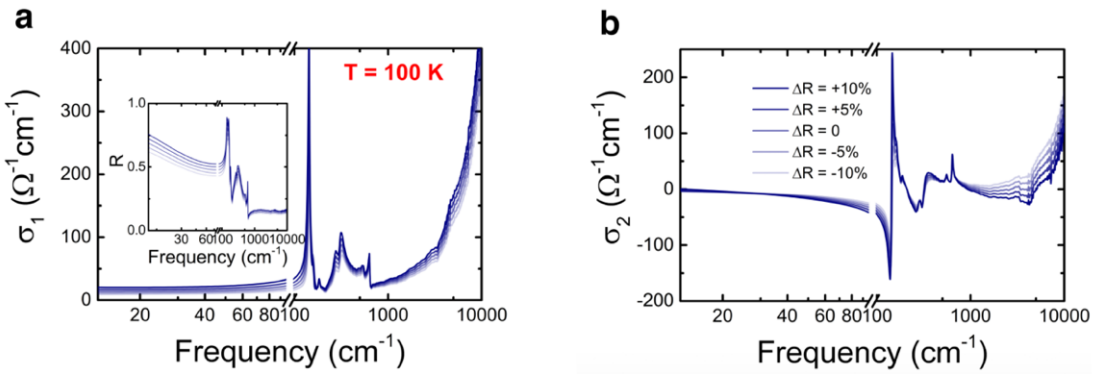

Figure D.1. (a) The real part of optical conductivity obtained from Kramer-Krönig transformation with ± 5% and ± 10% statistic error in the measured Reflectivity. Inset: Reflectivity with ± 5% and ± 10% statistic error in the measurement. **(b)** The imaginary part of optical conductivity.

Penetration depth

At each frequency, the penetration depths of the electric fields into the material were calculated by $d(\omega) = \frac{c}{2\omega \cdot \mathrm{Im}[\tilde{n}_0(\omega)]}$ ($\tilde{n}_0(\omega)$, stationary complex refractive index). The frequency-dependent penetration depth along the *c*-axis at 100 K is shown in Figure D.2. As discussed in Appendix D, the penetration depth mismatch is important to determine the size of the light-induced optical constants. The uncertainty in penetration depth could either come from the uncertainty in the Reflectivity measurement, or the spectrum measurement of the pump beam. In the narrowband measurement, the spectral bandwidth is quite narrow, resulting in a lower uncertainty in the data analysis.

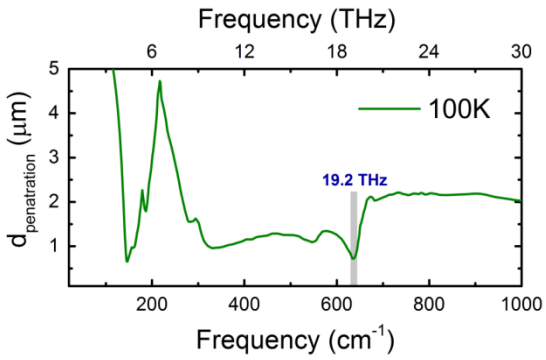

Figure D.2. Frequency-dependent penetration depth for the pump light wave along the *c*-axis in $YBCO_{6.5}$ at 100 K. The value for 19.2 THz is 0.7 μm, which is highlighted in grey.

Analytic models of photo-excited materials

Due to the mismatch in the penetration depth between the pump and probe beams, an accurate model is needed to reconstruct the light-induced optical constants changes in the excited

materials. If a large penetration depth mismatch exists, a single-layer model can be applied assuming a homogenously excited layer on top of an unperturbed bulk (Figure D.3(a)). On the other hand, a more accurate solution can be applied, which treats the system as a multilayer with the pumped volume described as a stack of thin layers. In the multilayer model, the refractive index decays exponentially into the material.

Figure D.4 summarizes the three sources of the uncertainty mentioned above. Typical uncertainty in the absolute value of the measured equilibrium reflectivity is about ± 2-3%. Figure D.4(a-b) shows as colored bands the propagated error bars in the equilibrium and transient optical properties for a ± 5% uncertainty in R(ω). The response appears to be only marginally affected.

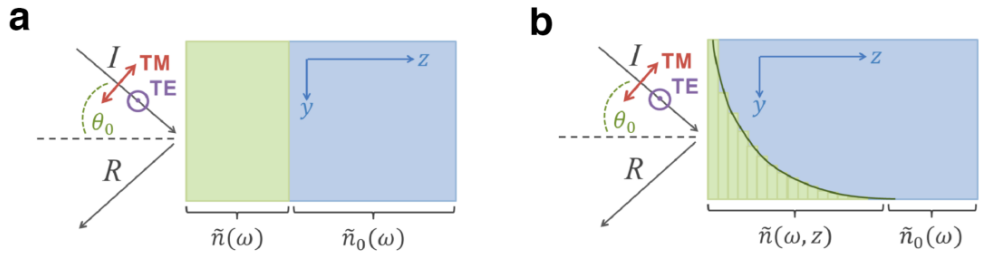

Figure D.3. Different models for penetration depth mismatch in data analysis. **(a)** Single-layer model. The material is modeled as a single excited layer on an unperturbed bulk. **(b)** Multi-layer model. The system is modeled as a multilayer, with the pumped volume described as a stack of thin layers with the z-independent refractive index. The refractive index decays exponentially into the material. Figures are taken from [202].

Another possible source of error resides in the value of the pump penetration depth used in the layered-system analysis. In Figure D.4(c-d) depicts how a ± 20% and a ± 40% change in the pump penetration depth would affect the transient optical properties.

Finally, in Figure D.4(e-f) we show the effect of a different choice of the model for describing the pump-probe penetration depth mismatch. The "single" photo-excited layer description, used for all data analyzed in Chapter 4 is compared with an exponential "multi-layer" decay model (used, for example, in Ref. [7]). Importantly, in all cases considered here, the impact of the different sources of error on the calculated optical conductivities is negligible.

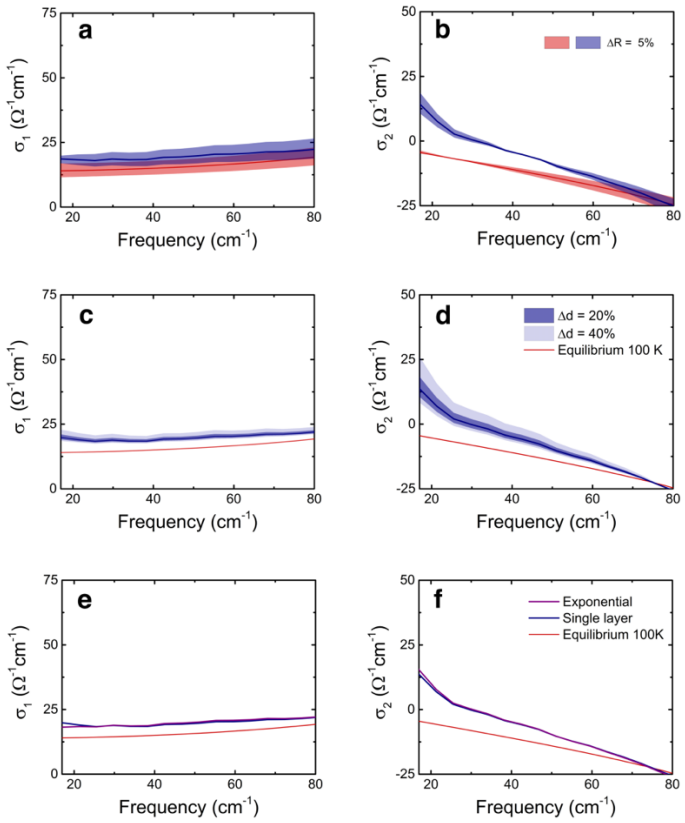

Figure D.4. Effects of different sources of uncertainties in the determination of the transient optical conductivity of $YBa_2Cu_3O_{6.5}$ at T = 100 K and $\tau = 0.6$ ps time delays after narrowband excitation at 19.2 THz. In all panels, equilibrium values are shown in red, while transient spectra are in blue. Error bars displayed as colored bands, have been propagated as follows: **(a-b)** ±5% uncertainty in the equilibrium R(ω); **(c-d)**, ±20% and ±40% change in the pump penetration depth d= 0.7 μm. **(e-f)** different analytic models for pump-probe penetration depth mismatch: **(e)** single-layer model and **(f)** multi-layer model. Pump penetration depth is set to 0.7 μm in both cases.

Acknowledgements

Here I want to take this chance to express my gratitude to the people who helped and supported me during my life in Hamburg. First of all, I would like to thank my supervisor Prof. Andrea Cavalleri for offering me the opportunity in MPSD and inspiring me to fulfill the project which was thought to be impossible. Thanks to his patience and constructive advice which always help me out of the troubles in the past five years. I am grateful to the support from Dr. Michael Först, not only for the experimental skills he taught me in the lab but also for helping me improving scientific writing and presentation skills. Thank you for always supporting me behind my back throughout my Ph.D. I want to thank Dr. Michael Fechner, Dr. Daniele Nicolleti and Dr. Michele Buzzi for valuable discussion for my project and thesis. I also want to thank Thomas, Matthias, Alex, Ken, Ankit, Tobia, Toru, Roman, and Andrea Cartella for sharing their time and wonderful thoughts with me in the lab.

Thanks to my wife Lan, thank you for giving up the cozy life in China to company me in Germany throughout the good and bad days, especially bringing our lovely daughter to this world. Thanks to my little daughter Chunxi for all the joy and experience she brings to us. I should also thank our parents for the endless support and care they give to our small family. Thanks to Haiyun, Yunyun, Yizhou, Eryin, David, Sven, Dalong and other guys who spent time with me playing basketball, making Chinese food and playing boardcard, which brings me a lot of fun.

I should also thank most of the people in MPSD for helping me smoothly go through my life here in Hamburg. I want to thank my co-supervisor Franz X. Kärtner for sharing his research in China, which motivates me to pursue my research in Germany. Thanks to Sonia, Julia, and Neda for their significant contribtions to IMPRS, from which I benefit a lot. Thanks to Michael Volkmann, Boris, Birger, Ulrike, and Tania for helping me manufacture and purchase stuff for my scientific project.

Last but not least, I would like to say thank you to Regina, Michele, James, Gregor, Mariana, Benedikt, Meredith, Rashmi, Wanzheng, Jörg, Käthja, and all the people have ever help me here. Without all these people, I couldn't manage to move on and finish my Ph.D.

Bibliography

[1] M. Rini, R. Tobey, N. Dean, J. Itatani, Y. Tomioka, Y. Tokura, R. W. Schoenlein and A. Cavalleri, Control of the electronic phase of a manganite by mode-selective vibrational excitation. *Nature* **449**, 72 (2007).

[2] A.D. Caviglia, R. Schenwitzi, P. Popovich, W. Hu, H. Bromberger, R. Singla, M. Mitrano, M.C. Hoffman, S Kaiser, P. Zubko, S. Gariglio, J.-M. Triscone, M. Först, and A. Cavalleri, Ultrafast strain engineering in complex oxide heterostructures. *Phys. Rev. Lett.* **108**, 136801 (2012)

[3] T. Nova, A. Disa, M. Fechner and A, Cavalleri, Metastable ferroelectricity in optically strained $SrTiO_3$. *Science* **364**, 1075 (2019).

[4] D. Fausti, R.I. Tobey, N. Dean, S. Kaiser, A. Dienst, M.C. Hoffmann, S. Pyon, T. Takayama, H. Takagi and A. Cavalleri, Light induced Superconductivity in a Stripe-ordered Cuprate. *Science* **331**, 189 (2011).

[5] M. Först, R.I. Tobey, H. Bromberger, S.B. Willins, V. Khanna, A.D. Caviglia, Y.-D. Chuange, W.S. Lee, W.F. Schlotter, J.J. Turner, M.P. Minitti, O. Krupin, Z.J. Xu, J.S. Wen, G.D. Gu, S.S. Dhesi, A. Cavalleri, and J.P. Hill, Melting of charge stripes in vibrationally driven $La_{1.875}Ba_{0.125}CuO_4$: assessing the respective roles of electronic and lattice order in frustrated superconductors. *Phys. Rev. Lett.* **112**, 157002 (2014).

[6] W. Hu, S. Kaiser, D. Nicoletti, C. R. Hunt, I. Gierz, M. C. Hoffmann, M. Le Tacon, T. Loew, B. Keimer and A. Cavalleri, Optically enhanced coherent transport in $YBa_2Cu_3O_{6.5}$ by ultrafast redistribution of interlayer coupling. *Nat. Mat.* **13** 705 (2014).

[7] M. Mitrano, A. Cantaluppi, D. Nicoletti, S. Kaiser, A. Perucchi, S. Lupu, P. Di Pietro, D. Pontiroli, M. Ricco, S. R. Clark, D. Jaksch, and A. Cavalleri, Possible light-induced superconductivity in K_3C_{60} at high temperature. *Nature* **530**, 461 (2016).

[8] M. Först, A.D. Caviglia, R. Schenwitzi, R. Mankowsky, P. Zubko, V. Khanna, H. Bromberger, S.B. Willins, Y.-D. Chuange, W.S. Lee, W.F. Schlotter, J.J. Turner, G.L. Dakovski, M.P. Minitti, J. Robinson, S.R. Clark, D. Jaksch, J.-M. Triscone, J.P. Hill, S.S. Dhesi, and A. Cavalleri, Spatially resolved ultrafast magnetic dynamics launched at a complex-oxide hetero-interface. *Nat. Mat.* **14**, 883 (2015).

[9] R. Mankowsky, A. von Hoegen, M. Först and A. Cavalleri, Ultrafast reversal of the ferroelectric polarization. *Phys. Rev. Lett.* **118**, 197601 (2017).

[10] R. Mankowsky, A. Subedi, M. Först, S.O. Mariager, M. Chollet, H. Lemke, J. Robinson, J. Glownia, M. Minitti, A. Frano, M. Fechner, N. A. Spaldin, T. Loew, B. Keimer, A. Georges and A. Cavalleri, Nonlinear lattice dynamics as a basis for enhanced superconductivity in $YBa_2Cu_3O_{6.5}$. *Nature* **516,** 71 (2014).

[11] S. Kaiser, C. R. Hunt, D. Nicoletti, W. Hu, I. Gierz, H. Y. Liu, M. Le Tacon, T. Loew, D. Haug, B. Keimer, and A. Cavalleri, Optically induced coherent transport far above Tc in underdoped $YBa_2Cu_3O_{6+\delta}$. *Phys. Rev. B* **89**, 184516 (2014).

[12] D. Nicoletti, and A. Cavalleri, Nonlinear light-matter interaction at terahertz frequencies. *Adv. Opt. Phot.* **8**, 3, 401 (2016).

[13] R. Mankowsky, M. Först, and A. Cavalleri, Nonequilibrium control of complex solids by nonlinear phononics. *Rep. Prog. Phys* **79**, 064503 (2016).

[14] M. Kozina, M. Fechner, P.Marsik, T. van Driel, J. M. Glowernia, C. Bernhard, M. Radovic, D. Zhu, S. Bonetti, U. Staub and M.C. Hoffmann, Terahertz-driven phonon upconversion in $SiTO_3$. *Nat. Phys.* **15**, 387 (2019).

[15] S. Rajasekaran, E. Casandruc, Y. Laplace, D. Nicoletti, G. D. Gu, S. R. Clark, D. Jaksch and A. Cavalleri, Parametric amplification of a superconducting plasma wave. *Nat. Phys.* **12**, 1012 (2016).

[16] A. von Hoegen, R. Mankowsky, M. Fechner, M. Först and A. Cavalleri, Probing the Interatomic Potential of Solids with Strong-Field Nonlinear Phononics. *Nature*, **555**, 79 (2018).

[17] R. Mankowsky, Nonlinear phononics and structural control of strongly correlated materials. *Doctoral thesis*, Physics department, University of Hamburg. (2015).

[18] M. Först, C. Manzoni, S. Kaiser, Y. Tomioka, R. Merlin, and A. Cavalleri, Nonlinear phononics as a new ultrafast route to lattice control. *Nat. Phys.* **7**, 854 (2011).

[19] R. Matsunaga, Y. I. Hamada, K. Makise, Y. Uzawa, H. Terai, Z. Wang, and R. Shimano, Higgs Amplitude Mode in the BCS Superconductors $Nb_{1-x}Ti_xN$ induced by Terahertz Pulse Excitation, *Phys. Rev. Lett.,* **111**, 057002 (2013).

[20] M. Först, R. Mankowsky, and A. Cavalleri, Mode-selective control of the crystal lattice. *Acc. Chem. Res.* **28**, 380 (2015).

[21] A. Subedi, A. Cavalleri, and A. Georges, Theory of nonlinear phononics for coherent light control of solids. *Phys. Rev. B* **89**, 220301(R) (2014).

[22] P. G. Radaelli, Breaking symmetry with light: ultrafast ferroelectricity and magnetism from three phonon coupling. *Phys. Rev. B* **97**, 085145 (2018).

[23] O. Schubert, M. Hohenleutner, F. Langer, B. Urbanek, C. Lange, U. Huttner, D. Golde, T. Meier, M. Kira, S.W. Koch, R. Huber, Sub-cycle control of terahertz high-harmonic generation by dynamical Bloch oscillations. *Nat. Phot.* **8**, 119 (2014).

[24] M. Hohenleutner, F. Langer, O. Schubert, M. Knorr, U. Huttner, S.W. Koch, M. Kira, R. Huber, Real-time observation of interfering crystal electrons in high-harmonic generation. *Nature* **523**, 572 (2015).

[25] M. Först, R. Mankovsky, H. Bromberger, D.M. Fritz, H. Lemke, D. Zhu, M. Chollet, Y. Tomioka, Y. Tokura, R. Merlin, J.P. Hill, S.L. Johnson, A. Cavalleri. Displacive lattice excitation through nonlinear phononics viewed by femtosecond X-ray diffraction. *Solid state communication* **169**, 24 (2013).

[26] B.J. Sternlieb, J.P. Hill, U.C. Wildgruber, G.M. Luke, B. Nachumi, Y. Moritomo, Y. Tokura, Charge and magnetic order in $La_{0.5}Sr_{1.5}MnO_4$, *Phys. Rev. Lett.* **76**, 2169 (1996).

[27] R.I. Tobey, D. Prabhakaran, A.T. Boothroyd, A. Cavalleri, Ultrafast electronic phase transition in $La_{0.5}Sr_{1.5}MnO_4$ by coherent vibrational excitation: evidence for non-thermal melting of orbital order. *Phys. Rev. Lett.* **101**, 197404 (2008).

[28] A. Cartella, T. F. Nova, M. Fechner, R. Merlin and A. Cavalleri, Parametric amplification of optical phonons. *PNAS* **115**, (48), 12148 (2018) .

[29] R. Matsunaga, N. Tsuji,H. Fujita,A. Sugioka, K. Makise,Y. Uzawa, H. Terai,Z. Wang,H. Aoki, R. Shimano, Light-induced collective pseudospin precession resonating with Higgs mode in a superconductor. *Science* **345**, 1145 (2014)

[30] S. Rajasekaran, J. Okamoto, L. Mathey, M. Fechner, V. Thampy, G. D. Gu and A. Cavalleri, Probing optically silent superfluid stripes in cuprates, *Science,* **369**, 575 (2018).

[31] K. Katsumi, N. Tsuji, Y.I. Hamada, R. Matsunaga, J. Schneeloch, R. D. Zhong, G. D. Gu, H. Aoki, Y. Gallais, and R. Shimano, Higgs mode in the d-wave superconductor $Bi_2Sr_2CaCu_2O_{8+x}$ driven by an intense terahertz pulse. *Phys. Rev. Lett.* **120**, 117001 (2018).

[32] H. Chu, M. Kim, K. Katsumi, S. Kovalev, R.D. Dawson, L. Schwarz, N. Yoshikawa, G. Kim, D. Putzky, Z. Zhong Li, H. Raffy, S. Germanskiy, J.-C. Deinert, N. Awari, I. Ilyakov, B. Green, M. Chen, M. Bawatna, G. Christiani, G. Logvenov, Y. Gallais, A.V. Boris, B. Keimer, A. Schnyder, D. Manske, M. Gensch, Z. Wang, R. Shimano and S. Kaiser, New collective mode in superconducting cuprates uncovered by Higgs spectroscopy. *arXiv:1901.06675.*

[33] C.C. Homes, T. Timusk, and D.A. Bonn, R. Liang and W.N. Hardy, Optical phonons polarized along the c axis of $YBa_2Cu_3O_{6+x}$, for x = 0.5 → 0.95. *Can. J. Phys.* **73**, 663 (1995).

[34] G. Burns, F. H. Dacol, P. P. Freitas, W. König, and T. S. Plaskett, Phonons in $YBa_2Cu_3O_{7-\delta}$-type materials. *Phys. Rev. B* **37**, 5171 (1988).

[35] B. Liu, M. Först, M. Fechner, D. Nicoletti, J. Porras, B. Keimer, A. Cavalleri, Two pump frequency resonances for light-induced superconductivity in $YBa_2Cu_3O_{6.5}$. *arXiv:1905.08356*.

[36] B Ferguson, XC Zhang, Materials for terahertz science and technology. *Nat. Mater.* **1**, 26 (2002).

[37] H. A. Hafez, X. Chai, A. Ibrahim, S. Mondal, D. Férachou, X. Ropagnol and T. Ozaki, Intense terahertz radiation and their applications. *J. Opt.* **18**, 093004 (2016).

[38] D. Nicoletti and A. Cavalleri, Nonlinear light–matter interaction at terahertz frequencies**.** *Advances in Optics and Photonics*, **3**, 401 (2016).

[39] R. Mankowsky, M. Först and A. Cavalleri, Nonequilibrium control of complex solids by nonlinear phononics. *Reports on Progress in Physics* **79**, 6 (2016).

[40] S. A. Zvyagin, M. Ozerov, E. Čižmár, D. Kamenskyi, S. Zherlitsyn, T. Herrmannsdörfer, J. Wosnitza, R. Wuensch and W. Seidel, Terahertz-range free-electron laser electron spin resonance spectroscopy: Techniques and aplications in high magnetic fields. *Rev. of Sci. Inst.* **80**, 073102 (2009).

[41] B. Green, S. Kovalev, V. Asgekar, G. Geloni, U. Lehnert, T. Golz, M. Kuntzsch, C. Bauer, J. Hauser, J. Voigtlaender, B. Wustmann, I. Koesterke, M. Schwarz, M. Freitag, A. Arnold, J. Teichert, M. Justus, W. Seidel, C. Ilgner, N. Awari, D. Nicoletti, S. Kaiser, Y. Laplace, S. Rajasekaran, L. Zhang, S. Winnerl, H. Schneider, G. Schay, I. Lorincz, A. A. Rauscher, I. Radu, S. Mährlein, T. H. Kim, J. S. Lee, T. Kampfrath, S. Wall, J. Heberle, A. Malnasi-Csizmadia, A.

Steiger, A. S. Müller, M. Helm, U. Schramm, T. Cowan, P. Michel, A. Cavalleri, A. S. Fisher, N. Stojanovic & M. Gensch. High-Field High-Repetition-Rate Sources for the Coherent THz Control of Matter. *Scientific Reports* **6**, 22256 (2016).

[42] G. L. Carr, M. C. Martin, W. R. McKinney, K. Jordan, G. R. Neil, and G. P. Williams, *Nature* **420**, 153 (2002).

[43] A. Sell, A. Leitenstorfer and R. Huber, Phase-locked generation and field-resolved detection of widely tunable terahertz pulses with amplitudes exceeding 100 MV/cm. *Opt. Lett.* **33**, 2767 (2008).

[44] Robert Boyd, Nonlinear Optics, 3rd Edition. *ISBN*: 9780080485966 (2008).

[45] A. Schneider, M. Neis, M. Stillhart, B. Ruiz, R.U.A. Khan, P. Gunter, Generation of terahertz pulses through optical rectification in organic DAST crystals: theory and experiment. *J. Opt. Soc. Am. B* **23**, 1822 (2006).

[46] A. Schneider, Theory of terahertz pulse generation through optical rectification in a nonlinear optical material with a finite size. *Phys. Rev. A* **82**, 033825 (2010).

[47] Peter R. Griffiths, James A. De Haseth, Fourier Transform Infrared Spectroscopy (2nd ed.). Wiley-Blackwell. *ISBN 978-0-471-19404-0*.

[48] K. E. Peiponen, A. Zeitler, M. Kuwata-Gonokami, Terahertz Spectroscopy and Imaging. *ISBN: 3642295649.*

[49] M. Jazbinsek, U. Puc, A. Abina, and A. Zidansek, Organic Crystals for THz Photonics. *Appl. Sci.* **9**, 882 (2019).

[50] R.L. Sutherland, Handbook of Nonlinear Optics. *ISBN* 9780824742430 (2003).

[51] L. Dalton, P. Gunter, M. Jazbinsek, O.P. Kwon, P. Sullivan, Nonlinear Optical Properties of Organic Molecules and Crystals. *Cambridge University Press: Cambridge, UK,* (2015).

[52] S. W. Jolly, N. H. Matlis, F. Ahr, V. Leroux, T. Eichner, A. L. Calendron, H. Ishizuki, T. Taira, F.X. Kärtner and A. R. Maier, Spectral phase control of interfering chirped pulses for high-energy narrowband terahertz generation. *Nat. Comm.* **10**, 2591 (2019).

[53] J. Hebling, G. Almási, I. Z. Kozma, and J. Kuhl, Velocity matching by pulse front tilting for large-area THz-pulse generation. *Opt. Express* **10**, 1161 (2002).

[54] Z. Bor, B. Racz, G. Szabo, M. Hilbert, H. A. Hazim Femtosecond pulse front tilt caused by angular dispersion. *Optical Engineering*, **32**, 10 (1993).

[55] J. Shikata, M. Sato, T. Taniuchi, and H. Ito, Enhancement of terahertz-wave output from $LiNbO_3$ optical parametric oscillators by cryogenic cooling. *Opt. Lett.* **4**, 202 (1999).

[56] S.-W. Huang, E. Granados, W. R. Huang, K.-H. Hong, L. E. Zapata, and F. X. Kärtner, High conversion efficiency, high energy terahertz pulses by optical rectification in cryogenically cooled lithium niobate," *Opt. Lett.* **38**, 796 (2013).

[57] D. H. Auston, Subpicosecond electro-optic shock waves. *Appl. Phys. Lett.* **43**, 713(1983).

[58] D. H. Auston, K. P. Cheung, J. A. Valdmanis, and D. A. Kleinman, Cherenkov radiation from femtosecond optical pulses in electro-optic media. *Phys. Rev. Lett*. **53**, 1555 (1984).

[59] J. Hebling, K. Yeh, M. C. Hoffmann, B. Bartal and Keith A. Nelson, Generation of high-power terahertz pulses by tilted-pulse-front excitation and their application possibilities. *J. Opt. Soc. Am B*, **25**, 6, (2008).

[60] Z. Chen, X. Zhou, C.A. Werly and K.A. Nelson, Generation of high power tunable multicycle terahertz pulses. *Appl. Phys. Lett.* **99**, 071102 (2011).

[61] E. A. Nanni, W. R. Huang, K.- H. Hong, K. Ravi, A. Fallahi, G. Moriena, R. J. D. Miller, F.X. Kärtner, Terahertz-driven linear electron acceleration. *Nat*. *Comm*. **6**, 8486 (2015).

[62] D. Zhang, A. Fallahi, M. Hemmer, X. Wu, M. Fakhari, Y. Hua, H. Cankaya, A.-L. Calendron, L. E. Zapata, N. H. Matlis and F.X. Kärtner, Segmented terahertz electron accelerator and manipulator (STEAM). *Nat. Phot.* **12**, 336 (2018).

[63] X. C. Zhang, X. F. Ma, Y. Jin, T. M. Lu, E. P. Boden, P.D. Phelps, K.R. Stewart, C. P. Yakymyshyn, Terahertz optical rectification from a nonlinear organic-Crystal. *Appl. Phys. Lett.* **61**, 3080 (1992).

[64] P.Y. Han, M. Tani, F. Pan, X.C Zhang, Use of the organic crystal DAST for terahertz beam applications. *Opt. Lett.* **25**, 675 (2000).

[65] A. Schneider, M. Neis, M. Stillhart, B. Ruiz, R.U.A Khan, P. Gunter, Generation of terahertz pulses through optical rectification in organic DAST crystals: theory and experiment. *J. Opt. Soc. Am. B.* **23**, 1822 (2006).

[66] I. Katayama, R. Akai, M. Bito, H. Shimosato, K. Miyamoto, H. Ito, M. Ashida, Ultrabroadband terahertz generation using 4-N,N-dimethylamino-4'-N'-methyl-stilbazolium2,4,6-trimethylbenzenesulfonate single crystals. *Appl. Phys. Lett.* **97**, 021105 (2010).

[67] C.P. Hauri, C. Ruchert, C. Vicario, F. Ardana, Strong-field single-cycle THz pulses generated in an organic crystal. *Appl. Phys. Lett.* **99**, 161116 (2011).

[68] M. Stillhart, A. Schneider, P. Guenter, Optical properties of 4-N,N-dimethylamino-4'-N'-methyl-stilbazolium2,4,6-trimethylbenzenesulfonate crystals at terahertz frequencies. *J. Opt. Soc. Am. B* **25**, 1914 (2008).

[69] C. Vicario, B. Monoszlai, C.P. Hauri, GV/m Single-Cycle Terahertz Fields from a Laser-Driven Large-Size Partitioned Organic Crystal. *Phys. Rev. Lett.* **112**, 213901 (2014).

[70] C. Vicario, C. Ruchert, C.P. Hauri, High field broadband THz generation in organic materials. *J. Mod. Opt.* **62**, 1480 (2015).

[71] M. Shalaby, C.P. Hauri, Demonstration of a low-frequency three-dimensional terahertz bullet with extreme brightness. *Nat. Commun.* **6**, 5976 (2015).

[72] F.D.J. Brunner, O.P. Kwon, S.J. Kwon, M. Jazbinsek, A. Schneider, P. A Gunter, hydrogen-bonded organic nonlinear optical crystal for high-efficiency terahertz generation and detection. *Opt. Express* **16**, 16496 (2008).

[73] C. Ruchert, C. Vicario, and C. P. Hauri, Scaling submillimeter single-cycle transients toward megavolts per centimeter field strength via optical rectification in the organic crystal OH1. *Opt. Lett.* **37**, 899 (2012).

[74] A. Majkić, M. Zgonik, A. Petelin, M. Jazbinšek, B. Ruiz, C. Medrano, and P. Günter, Terahertz source at 9.4 THz based on a dual-wavelength infrared laser and quasi-phase matching in organic crystals OH1. *Appl. Phys. Lett.* **105**, 141115 (2014).

[75] C. Vicario, A. V. Ovchinnikov, O. V. Chefonov and C. P. Hauri, Multi-octave spectrally tunable strong-field Terahertz laser. *arXiv: 1608.05319.*

[76] C. Vicario, B. Monoszlai, M.Jazbinsek, S.H. Lee, O.P. Kwon, C.P. Hauri, Intense, carrier frequency and bandwidth tunable quasi single-cycle pulses from an organic emitter covering the Terahertz frequency gap. *Sci. Rep.* **5**, 14394 (2015).

[77] A. Rovere, Y.G. Jeong, R. Piccoli, S.H. Lee, S.C. Lee, O.P. Kwon, M. Jazbinsek, R. Morandotti, L. Razzari, Generation of high-field terahertz pulses in an HMQ-TMS organic crystal pumped by an ytterbium laser at 1030 nm. *Opt. Express* **26**, 2509 (2018).

[78] K. Miyamoto, S. Ohno, M. Fujiwara, H. Minamide, H. Hashimoto, H. Ito, Optimized terahertz-wave generation using BNA-DFG. *Opt. Express* **17**, 14832 (2009).

[79] M. Shalaby, C. Vicario, K. Thirupugalmani, S. Brahadeeswaran, C.P. Hauri, Intense THz source based on BNA organic crystal pumped at Ti:sapphire wavelength. *Opt. Lett.* **41**, 1777 (2016).

[80] C. Vicario, M. Jazbinsek, A. V. Ovchinnikov, O. V. Chefonov, S. I. Ashitkov, M. B. Agranat, and C. P. Hauri, High efficiency THz generation in DSTMS, DAST and OH1 pumped by Cr:forsterite laser. *Opt. Express* **23**, 4 (2015).

[81] A.V. Ovchinnikov, O.V. Chefonov, V.Y. Molchanov, K.B. Yushkov, C. Vicario, C. Hauri, Generation of frequency-tunable pulsed terahertz radiation by a Cr: Forsterite laser system with an acousto-optical control of the pulse temporal profile. *Quantum Electron.* **46**, 1149 (2016).

[82] A. Schneider, M. Stillhart, P. Gunter, High efficiency generation and detection of terahertz pulses using laser pulses at telecommunication wavelengths. *Opt. Express* **14**, 5376 (2006).

[83] A. G. Stepanov, C. Ruchert, J. Levallois, C. Erny, and P. H. Christoph, Generation of broadband THz pulses in organic crystal OH1 at room temperature and 10 K. *Opt. Matet. Exp.* **4,** 870 (2014).

[84] B.J. Kang, S.H. Lee, W.T. Kim, S.C. Lee, K. Lee, G. Benacchio, G. Montemezzani, G. Jazbinsek, O.P. Kwon, F. Rotermund, New Class of Efficient Terahertz Generators: Effective Terahertz Spectral Filling by Complementary Tandem Configuration of Nonlinear Organic Crystals. *Adv. Funct. Mater.* **28**, 1707195 (2018).

[85] T. Taniuchi, S. Okada, and H. Nakanishi, Widely tunable terahertz-wave generation in an organic crystal and its spectroscopic application. *Journal of Appl. Phys.* **95**, 5984 (2004).

[86] T. Satoh, Y. Toya, S. Yamamoto, T. Shimura, K. Kuroda, Y. Takahashi, M. Yoshimura, Y. Mori, T. Sasaki, and S. Ashihara, Generation of mid- to far-infrared ultrashort pulses in 4-dimethylamino-N-methyl-4-stilbazolium tosylate crystal, *J. Opt. Soc. Am. B* **27**, 2507 (2010).

[87] F. Junginger, A. Sell, O. Schubert, B. Mayer, D. Brida, M. Marangoni, G. Cerullo, A. Leitenstorfer, and R. Huber, Single-cycle multiterahertz transients with peak fields above 10 MV/cm. *Opt. lett.* **35**, 2645 (2010).

[88] M. Knorr, J. Raab, M. Tauer, P. Merkl, D. Peller, E. Wittmann, E. Riedle, C. Lange, and R. Huber, Phase-locked multi-terahertz electric fields exceeding 13 MV/cm at a 190 kHz repetition rate. *Opt. lett.* **21**, 4267 (2017).

[89] S. R. Marder, J. W. Perry, Nonlinear optical polymers: discovery to market in 10 years? *Science* **263**, 1706 (1994).

[90] Z. Yang, L. Mutter, M. Stillhart, B. Ruiz, S. Aravazhi, M. Jazbinsek, A. Schneider, V. Gramlich, and P. Günter, Large-Size Bulk and Thin-Film Stilbazolium-Salt Single Crystals for Nonlinear Optics and THz Generation. *Adv. Funct. Mater.* **17,** 2018 (2007).

[91] Y. Li, J. Zhang, G. Zhang, L. Wu, P. Fu, Y. Wu, Growth and characterization of DSTMS crystals. *Journal of Crystal Growth* **327,** 127 (2011).

[92] G. Montemezzani, M. Alonzo, V. Coda, M. Jazbinsek, and P. Günter, Running electric field gratings for detection of coherent radiation. *J. Opt. Soc. Am. B* **32**, 1078 (2015).

[93] F. Raoult, A. C. L. Boscheron, D. Husson, C. Sauteret, A. Modena, V. Malka, F. Dorchies, and A. Migus, Efficient generation of narrowband-bandwidth picosecond pulses by frequency doubling of femtosecond chirped pulses. *Opt. Lett.* **23**, 1117 (1998).

[94] G. Veitas and R. Danielius, Generation of narrow-bandwidth tunable picosecond pulses by difference-frequency mixing of stretched pulses. *J. Opt. Soc. Am. B* **16**, 1561 (1999).

[95] S. Wandel, M.-W. Lin, Y. Yin, G. Xu, and I. Jovanovic, Bandwidth control in 5 μm pulse generation by dual-chirped optical parametric amplification. *J. Opt. Soc. Am. B* **33**, 1580 (2016).

[96] F. O. Koller, K. Haiser, M. Huber, T. E. Schrader, N. Regner, W. J. Schreier, and W. Zinth, Generation of narrowband subpicosecond mid-infrared pulses via difference frequency mixing of chirped near-infrared pulses. *Opt. Lett.* **32**, 3339 (2007).

[97] A. Cartella, T. F. Nova, A. Oriana, G. Cerullo, M. Först, C. Manzoni and A. Cavelleri, Narrowband carrier-envelope phase stable mid-infrared pulses at wavelengths beyond 10 μm by chirped-pulse difference frequency generation. *Opt. Lett.* **42**, 663 (2017).

[98] G. Cerullo and S. D. Silvestri, Ultrafast optical parametric amplifiers. *Review of Scientific Instruments* **74**, 1 (2003).

[99] C. Manzoni and G. Cerullo, Design criteria for ultrafast optical parametric amplifiers. *J. Opt.* **18**, 103501 (2016).

[100] M. Bass, *Handbook of Optics, 3rd ed., Vol. IV of Optical Properties of Materials, Nonlinear Optics, Quantum Optics*, McGraw-Hill (2009).

[101] B. Liu, H. Bromberger, A. Cartella, T. Gebert, M. Först, A. Cavalleri, Generation of narrowband, high-intensity, carrier-envelope phase stable pulses tunable between 4 and 18 THz. *Opt. Lett,* **42**, 129 (2017).

[102] H. R. Telle, G. Steinmeyer, A. E. Dunlop, J. Stenger, D. H. Sutter, U. Keller, Carrier-envelope offset phase control: A novel concept for absolute optical frequency measurement and ultrashort pulse generation. *Appl. Phys.* **69**, 327 (1999).

[103] A. Baltuška, T. Fuji, and T. Kobayashi, Controlling the Carrier-Envelope Phase of Ultrashort Light Pulses with Optical Parametric Amplifiers. *Phys. Rev. Lett,* **88**, 133901 (2002).

[104] R. Singla, G. Cotugno, S. Kaiser, M. Först, M. Mitrano, H. Y. Liu, A. Cartella, C. Manzoni, H. Okamoto, T. Hasegawa, S. R. Clark, D. Jaksch, and A. Cavalleri, THz-Frequency Modulation of the Hubbard U in an Organic Mott Insulator. *Phys. Rev. Lett.* **115**, 187401 (2015).

[105] C. Manzoni, M. Först, H. Ehrke, and A. Cavalleri, Single-shot detection and direct control of carrier phase drift of midinfrared pulses. *Opt. Lett.* **35**, 757 (2010).

[106] K. Iwaszczuk, D. G. Cooke, M. Fujiwara, H. Hashimoto and P. Uhd Jepsen, Simultaneous reference and differential waveform acquisition in time-resolved terahertz spectroscopy. *Opt. Express* **17**, 21969 (2009).

[107] J. G. Bednorz, K. A. Mueller, Possible high T_c superconductivity in the Ba-La-Cu-O system. *Z. Phys. B* **64**, 189 (1986).

[108] J.G. Bednorz, K.A. Müller, Perovskite-type oxides - The new approach to high-Tc superconductivity. *Rev. Mod. Phys.* **60**, 585 (1988).

[109] M.K. Wu, J.R. Ashburn, C.J. Torng, P.H. Hor, R.L. Meng, L. Gao, Z.J. Huang, Y.Q. Wang, and C.W. Chu, Superconductivity at 93 K in a new mixed-phase Y-Ba-Cu-O compound system at ambient pressure. *Phys. Rev. Lett.* **58**, 908 (1987).

[110] H. Maeda, Y. Tanaka, M. Fukutomi and T. Asano, A New High-Tc Oxide Superconductors without a Rare Earth Element. *Jpn. J. App. Phys.* **27**, 209 (1988).

[111] Z.Z. Sheng, A.M. Hermann, Bulk superconductivity at 120 K in the Tl-Ca/Ba-Cu-O system. *Nature* **332**, 55 (1988).

[112] A. Schilling, M. Cantoni, J.D. Guo, H.R. Ott, Superconductivity above 130 K in the Hg-Ba-Ca-Cu-O system. *Nature* **363**, 56 (1993).

[113] A. Dienst, Nonlinear Control of the Josephson Plasma in Superconducting Cuprates, Doctoral thesis, Brasenose College, University of Oxford (2011)..

[114] Taupin, Study of the magnetic heavy fermions UCoGe and YbRh2Si2 by transport measurements. Doctoral thesis, Université Joseph-Fourier - Grenoble I, (2013).

[115] L. Gao, Y. Y. Xue, F. Chen, Q. Xiong, R. L. Meng, D. Ramirez, C. W. Chu, J. H. Eggert and H. K. Mao, Superconductivity up to 164 K in $HgBa_2Ca_{m-1}Cu_mO_{2m+2+\delta}$ (m=1, 2, and 3) under quasi-hydrostatic pressures. *Phys. Rev. B* **50**, 4260 (1994).

[116] K. Chang, When superconductivity became clear (to some). *New York Times* (2008).

[117] B. Keimer, S. A. Kivelson, M. R. Norman, S. Uchida, and J. Zaanen, From quantum matter to high-temperature superconductivity in copper oxides. *Nature* **518**, 179 (2015).

[118] S. Peli, S. Dal Conte, R. Comin, N. Nembrini, A. Ronchi, P. Abrami, F. Banfi, G. Ferrini, D. Brida, S. Lupi, M. Fabrizio, A. Damascelli, M. Capone, G. Cerullo and C. Giannetti, Mottness at finite doping and charge instabilities in cuprates. *Nat. Phys.* **13**, 806 (2017).

[119] J. Fink, N. Nücker, H. A. Romberg and J. C. Fuggle, Electronic structure studies of high- Tc superconductors by high-energy spectroscopies. *IBM J. Res. Dev.* **33**, 372 (1989).

[120] M.A. Hossain, J.D.F. Mottershead, D. Fournier, A. Bostwick, J.L. McChesney, E. Rotenberg, R. Liang, W.N. Hardy, G.A. Sawatzky, I.S. Elfimov, D.A. Bonn,

and A. Damascelli, In situ doping control of the surface of high-temperature superconductors. *Nat. Phys.* **4**, 527 (2008).

[121] T. Freltoft, J.E. Fisher, G. Shirane, D.E. Moncton, S.K. Sinha, D. Vaknin, J.P. Remeika, A.S. Cooper, D. Harshman, Antiferromagnetism and oxygen deficiency in single-crystal $La_2CuO_{4-\delta}$. *Phys. Rev. B* **36**, 826 (1987).

[122] D. Vaknin, S.K. Sinha, D.E. Moncton, D.C. Johnston, J.M. Newsam, C.R. Safinya, H.E. Jr. King, Antiferromagnetism in La_2CuO_{4-y}. *Phys. Rev. Lett.* **58**, 2802 (1987).

[123] M.R. Norman, The Challenge of Unconventional Superconductivity. *Science* **332**, 196 (2011).

[124] J. Bardeen, L.N. Cooper, and J.R. Schrieffer, Theory of superconductivity. *Phys. Rev.* **108**, 1175 (1957).

[125] N. Plakida, High temperature cuprate superconductors: experiment, theory and applications. Springer series in solid-state science, *ISBN-10: 9783642126321* (2010).

[126] W. L. McMillan, Transition Temperature of Strong-Coupled Superconductors. *Phys. Rev.* **167**, 331 (1968).

[127] N.N. Bogoliubov, V.V. Tolmachev, D.V. Shirkov, New method in the theory of superconductivity, *Fortsch. Phys.* **605**, 6 (1958).

[128] P. J. Hirschfeld, Using gap symmetry and structure to reveal the pairing mechanism in Fe-based superconductors. *C R. Physique* **17**, 197 (2016).

[129] P. Marra, Theoretical approach to direct resonant inelastic x-ray scattering on magnets and superconductors. Doctoral thesis, Fakultät für Mathematik und Naturwissenschaftern, Technishe Universität Dresden (2015).

[130] A.J. Leggett, A theoretical description of the new phases of liquid 3He. *Rev. Mod. Phys.* **47**, 331 (1975).

[131] J.R. Kirtley, C.C. Tsuei, A. Ariando, C.J.M. Verwijs, S. Harkema, and H. Hilgenkamp, Angle-resolved phase-sensitive determination of the in-plane gap symmetry in $YBa_2Cu_3O_{7-\delta}$. *Nat. Phys.* **2**, 190 (2006).

[132] A. Damascelli, Z. Husain, Z.X. Shen, Angle-resolved photoemission studies of the cuprate superconductors. *Rev. Mod. Phys.* **75**, 473 (2003).

[133] P. W. Anderson, The Resonating Valence Bond State in La_2CuO_4 and Superconductivity. *Science* **235**, 1196 (1987).

[134] T. A. Maier, D. Poilblanc, and D. J. Scalapino, Dynamics of the Pairing Interaction in the Hubbard and t−J Models of High-Temperature Superconductors. *Phys. Rev. Lett.* **100**, 237001 (2008).

[135] M. R. Norman, H. Ding, M. Randeria, J. C. Campuzano, T. Yokoya, T. Takeuchik, T. Takahashi, T. Mochiku, K. Kadowaki, P. Guptasarma and D. G. Hinks, Destruction of the Fermi surface in underdoped high-Tc superconductors. *Nature* **392**, 157 (1998).

[136] N. Doiron-Leyraud, C. Proust, D. LeBoeuf, J. Levallois, J.-B. Bonnemaison, R. Liang, D.A. Bonn, W.N. Hardy, and L. Taillefer, Quantum oscillations and the Fermi surface in an underdoped high-T_c superconductor. *Nature* **447**, 565 (2007).

[137] M. Hashimoto, I. M. Vishik, R.-H. He, T. P. Devereaux, and Z.- X Shen, Energy gaps in high-transition-temperature cuprate superconductors. *Nat. Phys.* **10**, 483 (2014).

[138] M.R. Presland, J.L. Tallon, R.G. Buckley, R.S. Liu, N.E. Flower, General trends in oxygen stoichiometry effects on Tc in Bi sand Tl superconductors. *Physica C* **176**, 95 (1991).

[139] W.W. Warren, R.E. Walstedt, G.F. Brennert, R.J. Cava, R. Tycko, R.F. Bell, and G. Dabbagh, Cu spin dynamics and superconducting precursor effects in planes above Tc in $YBa_2Cu_3O_{6.7}$. *Phys. Rev. Lett.* **62**, 1193 (1989).

[140] R. Daou, J. Chang, David LeBoeuf, Olivier Cyr-Choinière, Francis Laliberté, Nicolas Doiron-Leyraud, B. J. Ramshaw, Ruixing Liang, D. A. Bonn, W. N. Hardy, and Louis Taillefer, Broken rotational symmetry in the pseudogap phase of a high-T_c superconductor. *Nature* **463**,519 (2010).

[141] Y. Sato, S. Kasahara, H. Murayama, Y. Kasahara, E.-G. Moon, T. Nishizaki, T. Loew, J. Porras, B. Keimer, T. Shibauchi, and Y. Matsuda, Thermodynamic evidence for a nematic phase transition at the onset of the pseudogap in $YBa_2Cu_3O_y$. *Nat. Phys.* **13**, 1074(2017).

[142] Y. J. Uemura, Dynamic superconductivity responses in photoexcited optical conductivity and Nernst effect. *Phys. Rev. Mat.* **3**, 104801 (2019).

[143] B. Wuyts, V.V. Moshchalkov, and Y. Bruynseraede, Resistivity and Hall effect of metallic oxygen-vacant $YBa_2Cu_3O_x$ films in the normal state. *Phys. Rev. B* **53**, 9418 (1996).

[144] N. Plakida, High-temperature cuprate superconductors, experiment, theory and application. Springer, ISBN-10: 3642264832 (2010).

[145] Nancy Li, D. K. Bediako, R.G. Hadt, D. Hayes, T.J. Kempa, F. von Cube, D.C. Bell, L.X. Chen, and D. G. Nocera, Influence of iron doping on tetravalent nickel content in catalytic oxygen evolving films. *PNAS.* http://doi.org/10.1073/pnas.1620787114.

[146] T.R. Chien, Z.Z. Wang, N.P. Ong, Effect of Zn impurities on the normal-state Hall angle in single-crystal $YBa_2Cu_{3-x}Zn_xO_{7-d}$. *Phys. Rev. Lett.* **67**, 2088 (1991).

[147] S. Wakimoto, H. Zhang, K. Yamada, I. Swainson, H. Kim, and R.J. Birgeneau, Direct relation between the low-energy spin excitations and superconductivity of overdoped high-Tc superconductors. *Phys. Rev. Lett.* **92**, 217004 (2004).

[148] M. H. Bakr, Electronic and Phononic Raman Scattering in Twin-Free $YBa_2Cu_3O_{6+x}$. Doctoral thesis, Von der Fakultät Mathematik und Physik der Universität Stuttgart, (2010).

[149] N.H. Andersen, M. von Zimmermann, T. Frello, M. Käll, D. Mønster, P.-A. Lindg ard, J. Madsen, T. Niemöller, H.F. Poulsen, O. Schmidt, J.R. Schneider, Th. Wolf, P. Dosanjh, R. Liang, W.N. Hardy, Superstructure formation and the structural phase diagram of $YBa_2Cu_3O_{6+x}$. *Physica C* **317**, 259 (1999).

[150] S. I. Schlachter, U. Tutsch, W. H. Fietz, K.-P. Weiss, H. Leibrock, K. Grube, Th. Wolf, B. Obit, P. Schweiss, H. Wühl, Pressure effect and specific heat of RBa2Cu3Ox at distinct charge carrier concentrations: Possible influence of stripes, *Int. J. Mod. Phys. B* **14**, 3673 (2000).

[151] F. E. Bates and J. E. Eldridge, Zero-wavevector vibrations of $YBa_2Cu_3O_7$. *Solid State Communications* **64**, 1435 (1987).

[152] F. E. Bates, Normal modes of tetragonal YBa2Cu3O6 and orthorhombic $YBa_2Cu_3O_7$. *Phys. Rev. B* **39**, 322 (1989).

[153] D. N. Basov and T. Timusk, Electrodynamics of high-Tc superconductors. *Rev. Mod. Phys.* **77**, 721 (2005).

[154] C. C. Homes, T. Timusk, D. A. Bonn, R. Liang, and W. N. Hardy. Optical properties along the c-axis of $YBa_2Cu_3O_{6+x}$ for x = 0.50 → 0.95 Evolution of the pseudogap. *Physica C* **254**, 265 (1995).

[155] K. Tomari, R. Matsunaga, H. Niwa, D. Song, H., Eisaki and R. Shimano, Light-induced switching to metastable phase in a layered superconductor $La_{2-x}Sr_2CuO_4$. arXiv:1712.05086.

[156] C. C. Homes, T. Timusk, D. A. Bonn, R. Liang, and W.N. Hardy, Optical phonons polarized along the c-axis of $YBa_2Cu_3O_{6+x}$, for x → 0.5 to 0.95. *Can. J. Phys.* **73**, 663 (1995).

[157] S. Kaiser, C. R. Hunt, D. Nicoletti, W. Hu, I. Gierz, H. Y. Liu, M. Le Tacon, T. Loew, D. Haug, B. Keimer, and A. Cavalleri, Optically induced coherent transport far above Tc in underdoped $YBa_2Cu_3O_{6+\delta}$, *Phys. Rev. B* **89**, 184516 (2014).

[158] C. R. Hunt, D. Nicoletti, S. Kaiser, D. Pröpper, T. Loew, J. Porras, B. Keimer, and A. Cavalleri, Dynamical decoherence of the light induced interlayer coupling in $YBa_2Cu3O_{6+\delta}$, *Phys. Rev. B* **94**, 224303 (2016).

[159] M. Först, C. Manzoni, S. Kaiser, Y. Tomioka, Y. Tokura, R. Merlin, and A. Cavalleri, Nonlinear phononics as an ultrafast route to lattice control. *Nat. Phys.* **7**, 854 (2011).

[160] R. Mankowsky, M. Först, T. Loew, J. Porras, B. Keimer, and A. Cavalleri, Coherent modulation of the $YBa_2Cu_3O_{6+x}$ atomic structure by displacive stimulated ionic Raman scattering. *Phys. Rev. B* **91**, 094308 (2015).

[161] D. Nicoletti, E. Casandruc, Y. Laplace, V. Khanna, C. R. Hunt, S. Kaiser, S. S. Dhesi, G. D. Gu, J. P. Hill, A. Cavalleri, Optically-induced superconductivity in striped $La_{2-x}Ba_xCuO_4$ by polarization-selective excitation in the near infrared. *Phys. Rev. B* **90**, 100503(R) (2014).

[162] E. Casandruc, D. Nicoletti, S. Rajasekaran, Y. Laplace, V. Khanna, G. D. Gu, J. P. Hill, and A. Cavalleri, Wavelength-dependent optical enhancement of superconducting interlayer coupling in $La_{1.885}Ba_{0.115}CuO_4$. *Phys. Rev. B* **91**, 174502 (2015).

[163] D. Nicoletti, D. Fu, O. Mehio, S. Moore, A. S. Disa, G. D. Gu, and A. Cavalleri, Magnetic-Field Tuning of Light-Induced Superconductivity in Striped $La_{2-x}Ba_xCuO_4$. *Phys. Rev. Lett.* **121**, 267003 (2018).

[164] K. A. Cremin, J. Zhang, C. C. Homes, G. D. Gu, Z. Sun, M. M. Fogler, A. J. Millis, D. N. Basov, R. D. Averitt, Photo-enhanced metastable c-axis electrodynamics in stripe ordered cuprate $La_{1.885}Ba_{0.115}CuO_4$. *PNAS* **116**(40), 19875 (2019).

[165] S. J. Zhang, Z. X. Wang, L. Y. Shi, T. Lin, M. Y. Zhang, G. D. Gu, T. Dong, and N. L. Wang, Light-induced new collective modes in $La_{1.905}Ba_{0.095}CuO_4$ superconductor. *Phys. Rev. B* **98**, 020506(R) (2018).

[166] M. Först, R.I. Tobey, H. Bromberger, , S.B. Wilkins, V. Khanna, A.D. Caviglia, Y.D. Chuang, W.S. Lee, W.F. Schlotter, J.J. Turner, M.P. Minnitti, O. Krupin, X.J, Xu, J.S. Wen, G.D. Gu, S. S. Dhesi, A. Cavalleri and J. P. Hill, Melting charge stripes in vibrationally driven $La_{1.875}Ba_{0.125}CuO_4$: assessing the respective roles of Electronic and Lattice order in frustrated Superconductors. *Phys. Rev. Lett.* **112**, 157002 (2014).

[167] V. Khanna, R. Mankowsky, M. Petrich, H. Bromberger, S. A. Cavill, E. Möhr-Vorobeva, D. Nicoletti, Y. Laplace, G. D. Gu, J. P. Hill, M. Först, A. Cavalleri and S. S. Dhesi, Restoring interlayer Josephson coupling in $La_{1.885}Ba_{0.115}CuO_4$ by charge transfer melting of stripe order. *Phys. Rev. B* **93**, 224522 (2016).

[168] D. Fausti, R.I. Toby, N. Dean. S. Kaiser, A. Dienst, M. Hoffmann, S. Pyon, T. Takayam, H. Takagi, A. Cavalleri, Light induced superconductivity in a striped ordered cuprate. *Science* **331**, 189 (2011).

[169] S. J. Zhang, Z. X. Wang, H. Xiang, X. Yao, Q. M. Liu, L. Y. Shi, T. Lin, T. Dong, D. Wu, N. L. Wang, Photo-induced nonequilibrium response in heavily underdoped $YBa_2Cu_3O_{6.45}$ probed by time-resolved terahertz spectroscopy. arXiv:1904.10381 (2019).

[170] M. Dressel and G. Grüner, Electrodynamics of Solids, Cambridge University Press, Cambridge (2002)

[171] M. Mori, G. Khalliullin, T. Tohyama, S. Maekawa, Origin of the spatial variation of the pairing gap in Bi-based high temperature superconductors. *Phys. Rev. Lett.* **101**, 24720023 (2008).

[172] Y. Y. Peng, G. Dellea, M. Conni, A. Amorese, D. Di Castro, G.M. DeLuca, K. Kummer, M. Salluzzo, X. Sun, X.J. Zhou, G. Balestino, M. LeTacon, B. Keimer, L. Braicovic, N.B. Brookes, G. Ghiringhelli, Influence of apical oxygen on the extent of the in-plane exchange interaction in cuprate superconductors. *Nat. Phys.* **13**, 1201 (2017).

[173] S. J. Denny, S. R. Clark, Y. Laplace, A. Cavalleri, and D. Jaksch, Proposed Parametric Cooling of Bilayer Cuprate Superconductors by Terahertz Excitation. *Phys. Rev. Lett.* **114**, 137001 (2015).

[174] J. Okamoto, A. Cavalleri, and L. Mathey, Theory of enhanced interlayer tunneling in optically driven high Tc superconductors. *Phys. Rev. Lett.* **117**, 227001 (2016).

[175] M. Knap, M. Babadi, G. Refael, I. Martin, and E. Demler, Dynamical Cooper pairing in nonequilibrium electron-phonon systems. *Phys. Rev. B* **94**, 214504 (2016).

[176] M. Babadi, M. Knap, I. Martin, G. Refael, and E. Demler, Theory of parametrically amplified electron-phonon superconductivity. *Phys. Rev. B* **96**, 014512 (2017).

[177] M. Först, A. Frano, S. Kaiser, R. Mankowsky, C. R. Hunt, J. J. Turner, G. L. Dakovski, M. P. Minitti, J. Robinson, T. Loew, M. Le Tacon, B. Keimer, J. P. Hill, A. Cavalleri, and S. S. Dhesi, Femtosecond x rays link melting of charge-density wave correlations and light-enhanced coherent transport in $YBa_2Cu_3O_{6.6}$, *Phys. Rev. B*, **90**, 184514 (2014).

[178] M. Först, R.I. Tobey, H. Bromberger, , S.B. Wilkins, V. Khanna, A.D. Caviglia, Y.D. Chuang, W.S. Lee, W.F. Schlotter, J.J. Turner, M.P. Minnitti, O. Krupin, X.J, Xu, J.S. Wen, G.D. Gu, S. S. Dhesi, A. Cavalleri and J. P. Hill Melting Charge Stripes in Vibrationally Driven $La_{1.875}Ba_{0.125}CuO_4$: assessing the respective roles of Electronic and Lattice order in frustrated Superconductors. *Phys. Rev. Lett.* **112**, 157002 (2014).

[179] M. Buzzi, M. Först, R. Mankowsky, and A. Cavalleri, Probing dynamics in quantum materials with femtosecond X-rays. *Nat. Rev. Mater.* **3**, 299-311 (2018).

[180] L. J. P. Ament, M. van Veenendaal, T. P. Devereaux, J. P. Hill, and J. van den Brink, Resonant inelastic x-ray scattering studies of elementary excitations. *Rev. Mod. Phys.* **83**, 705 (2011).

[181] H.-H. Kim, S.M. Souliou, M. E. Barber, E. Lefrançois, M.Minola, M. Tortora, R. Heid, N. Nandi, R. A. Borzi, G. Garbarino, A. Bosak, J. Porras, T. Loew, M. König, P. J.W. Moll, A. P. Mackenzie, B. Keimer, C. W. Hicks, and M. Le Tacon, Uniaxial pressure control of competing orders in a high-temperature superconductor. *Science*, **362**, 1040 (2018).

[182] D. van der Marel and A. Tsvetkov, Transverse optical plasmons in layered superconductors. *Czech. J. Phys.* **46**, 3165 (1996).

[183] K. Oguchi, M. Okano and S. Watanabe, Polarization-Sensitive Electro-Optic Sampling of Elliptically-Polarized Terahertz Pulses: Theoretical Description and Experimental Demonstration. *Particles* **2**, 70 (2019)

[184] M. Fechner and N. A. Spaldin, Effects of intense optical phonon pumping on the structure and electronic properties of yttrium barium copper oxide. *Phys. Rev. B*, **94**, 134307 (2016).

[185] D. M. Juraschek, M. Fechner, and N. A. Spaldin, Ultrafast Structure Switching through Nonlinear Phononics. *Phys. Rev. Lett.* **118**, 054101 (2017).

[186] X. Gonze and C. Lee, Dynamical matrices, Born effective charges, dielectric permittivity tensors, and interatomic force constants from density-functional perturbation theory. *Phys. Rev. B* **55**, 10355 (1997).

[187] G. Khalsa and N. A. Benedek, Ultrafast optically induced ferromagnetic/anti-ferromagnetic phase transition in $GdTiO_3$ from first principles. *Npj Quantum Mater.* **3**, 15 (2018).

[188] E. Uykur, K. Tanaka, T. Masui, S. Miyasaka, and S. Tajima, Pseudogap Study Using *c*-axis Optical Spectra of Underdoped $YBa_2Cu_3O_{7-\delta}$. *Journal of Physical Society of Japan* **81**, SB035 (2012).

[189] http://elk.sourceforge.net, (n.d.).

[190] A. Togo and I. Tanaka, First principles phonon calculations in materials science. *Scr. Mater.* **108**, 1 (2015).

[191] R.J. Cava, A.W. Hewat, E.A. Hewat ,B. Batlogg, M. Marezio, K. M. Rabe, J.J. Krajewski, W.F. Peck Jr., and L.W. Rupp Jr., Structural anomalies, oxygn oderring nad superconductivity in oxuygen deficient $Ba_2YCu_3O_x$. *Physica C* **165**, 419 (1990).

[192] S.D. Conradson and I.D. Raistrick, The axial oxygen atom and superconductivity in $YBa_2Cu_3O_7$. *Science* **243**,1340 (1989).

[193] Z. Tesanovic, A.R. Bishop, and R.L. Martin, Planes and chains: A novel excitonic mechanism for high temperature superconductivity. *Solid State Commun.* **68**, 337 (1988).

[194] C. Taliani, R. Zamboni, G. Ruani, F.C. Matacotta, and K.I. pokhodnya, Infrared photoinduced absorption in the $YBa_2Cu_3O_{7-y}$ high T_c superconducting system. *Physica C* **66**, 487 (1988).

[195] A. von Hoegen, M. Fechner, M. Först, J. Porras, B. Keimer, M. Michael, E. Demler, and A. Cavalleri, Probing coherent charge fluctuationsin $YBa_2Cu_3O_{6+x}$ at wavevectors outside the light cone. *arXiv:1911.08284.*

[196] R. Mankowsky, M. Fechner, M. Först, A. von Hoegen, J. Porras, T. Loew, G. L. Dakovski, M. Seaberg, S. Möller, G. Coslovich, B. Keimer, S. S. Dhesi, and A. Cavalleri, Optically induced lattice deformations, electronic structure changes, and enhanced superconductivity in $YBa_2Cu_3O_{6.48}$. *Struct. Dyn.* **4**, 044007 (2017).

[197] A. Cantaluppi, M. Buzzi1, G. Jotzu, D. Nicoletti, M. Mitrano, D. Pontiroli, M. Riccò, A. Perucchi, P. Di Pietro and A. Cavalleri, Pressure tuning of light-induced superconductivity in K_3C_{60}. *Nat. Phys.* **14**, 837 (2018).

[198] A. Nava, C. Giannetti, A. Georges, E. Tosatti and M. Fabrizio, Cooling quasiparticles in A_3C_{60} fullerides by excitonic mid-infrared absorption. *Nat. Phys.* **14**, 154 (2018).

[199] K.W. Kim, A. Pashkin, H. Schäfer, M. Bezer-, M. Porer, T. Wolf, C. Bernhard, J. Demsar, R. Huber, A. Leitenstorfer, Ultrafast transient generation of spin-density-wave order in the normal state of $BaFe_2As_2$ driven by coherent lattice vibrations. *Nat. Mat.* **11**, 497 (2012).

[200] M. Yi, Y. Zhang, Z.X. Shen, D. Lu, Role of the orbital degree of freedom in iron-based superconductors. *npj, Quan. Mat.* **2**, 57 (2017).

[201] J. B. Kemper, Measurement of the heat capacity of cuprate superconductors in high magnetic fields. Thesis, College of arts and science, Florida State University (2014).

[202] C. Hunt, Manipulating Superconductivity in Cuprates with Selective Ultrafast Excitation. Department of Physics, University of Illinois at Urbana-Champaign (2015).